Interaction of particles with complex electrostatic structures and 3D clusters

Tetyana Antonova

München 2007

Interaction of particles with complex electrostatic structures and 3D clusters

Tetyana Antonova

Dissertation
an der Fakultät für Physik
der Ludwig–Maximilians–Universität
München

vorgelegt von
Tetyana Antonova
aus Kupyansk, Ukraine

München, den 16 Oktober 2007

Erstgutachter: Prof. Dr. Gregor E. Morfill

Zweitgutachter: Prof. Dr. Martin Faessler

Tag der mündlichen Prüfung: 30. November 2007

Contents

Introduction to complex plasmas **1**

1 Some theoretical aspects of complex plasmas **7**

1.1 Basic plasma parameters 8

1.2 RF discharge and plasma generation 9

1.3 A single charged particle in complex plasmas 10

1.3.1 Charging and electrostatic potential around a particle 11

1.3.2 Electric probe theories and the particle charging process 12

1.3.3 The forces acting on a single particle in plasma 24

1.4 Interaction between particles in complex plasmas 29

1.4.1 Electrostatic energy between grains 30

1.4.2 Shadow force 30

1.4.3 Wake potential 31

1.4.4 Dipole-dipole interaction 32

1.4.5 Strongly coupled dusty plasmas and crystal formation 33

2 Experimental set-up and methods of measurements **37**

2.1 The metallic chamber with glass windows 38

2.1.1 Vacuum system 38

2.1.2 Particle injection 39

2.1.3 Illumination of particles 40

2.2 The PKE-Nefedov chamber 41

2.2.1 Arrangement of the PKE-Nefedov chamber 41

2.2.2 Three-dimensional diagnostics 42

2.3 "Adaptive electrode" 45

2.4 Langmuir probe diagnostics 47

3 Complex plasma manipulation by radio-frequency biasing **51**

3.1 The levitation in the case $V_{RF} \leq V_{DC}$ 52

3.2 Particle charging in RF sheath . . . 53
3.3 Experiments with particles . . . 54
3.4 The levitation in the case $V_{RF} \gg V_{DC}$ . . . 57
3.5 Visualization of the plasma structure by fine particulate (∼nm) size . . . 59
3.6 Three dimensional clusters . . . 60
3.7 Conclusions . . . 65

4 Study of 3D plasma clusters' environment by emission spectroscopy 67
4.1 Experimental evidence . . . 68
4.2 Corona model . . . 70
4.3 The first method of ion density calculation . . . 71
4.4 The second method of ion density calculation . . . 71
4.5 Density profile of the "secondary plasma" . . . 72
4.6 Theoretical calculation of "plasma ball" density . . . 73
4.7 Conclusion . . . 75

5 Pair-interaction force in small 3D plasma clusters 77
5.1 Introduction . . . 77
5.2 Methods of measurements . . . 78
5.3 Particle charge . . . 78
5.4 Description of particle kinematics . . . 79
5.5 Analysis of forces in small clusters . . . 80
5.6 Attractive forces in medium size clusters . . . 81
5.7 Discussion . . . 82
5.8 Summary . . . 84

6 Limit of the co-operative regime in 3D plasma clusters 85
6.1 Experimental procedure . . . 85
6.2 Changing of the system energy after the arrival of new particles . . . 86
6.3 Changing of the system energy after escape of one of the particles . . . 87
6.4 Analysis of vibrations and dust acoustic waves . . . 90
6.5 Analysis of vibrations and surface tension . . . 92
6.6 Conclusion . . . 93

7 Microparticles as a diagnostic tool of the electronegative plasma sheath at low pressures 95
7.1 Features of electronegative plasmas . . . 96
7.2 Experimental evidence . . . 98

7.3 Modification of Bohm criterion in electronegative plasma 100
7.4 Calculation of electric field 104
7.5 Charge calculation 104
7.6 Levitation force 107
7.7 The measurements of α with electric probes 107
7.8 The temperature of negative ions 112
7.9 Simulations 115
7.10 Summary 117

Conclusions **119**

Bibliography **123**

Acknowledgements **131**

Publications **133**

Curriculum vitae **135**

Zusammenfassung

Mikropartikel, die in ein Plasma eingebracht werden, schweben gewöhnlich in der Plasmarandschicht, wo die Schwerkraft durch das starke elektrische Feld kompensiert wird. Hier organisieren sich die Teilchen selbst auf Grund ihrer elektrostatischen Wechselwirkungen und bilden Strukturen (z.B. sog. Plasmakristalle), die interessant für die Erforschung stark gekoppelter Systeme und kritischer Phänomene sind. Wegen der geringen Dämpfung (im Vergleich z.B. zu kolloidalen Suspensionen) ist es möglich, die Dynamik bis zu den relevanten höchsten Frequenzen (z.B. Einsteinfrequenz) auf dem elementarsten Niveau der Bewegung jedes einzelnen Partikels zu messen. Die Aufgabe dieser Arbeit war, dreidimensionale Strukturen und dynamische Prozesse in Plasmakristallen zu analysieren und die Grenzen kollektiven Verhaltens kleiner Systeme zu erforschen. Außerdem können die Mikropartikel selbst zur Diagnostik verwendet werden: zur Bestimmung der Plasmaparameter oder zur Beobachtung von Plasmaprozessen.

Die Laborexperimente wurden in Radiofrequenz (RF)-Plasmareaktoren mit parallelen Elektroden durchgeführt. Die untere, sogenannte 'adaptive Elektrode' ist in 57 kleine 'Pixel' aufgeteilt, die unabhängig voneinander mit Gleich- und/oder RF-Spannung gespeist werden können. Wenn eines dieser Pixel mit RF betrieben wird, bildet sich dort ein helles lokalisiertes Glühen, der 'sekundäre Plasmaball', in welchem Mikropartikel eingefangen werden können. Dadurch können kleine, dreidimensionale Plasmakristalle oder Plasmatropfen mit weniger als 100 Partikel gebildet werden — ideale Voraussetzungen für die Erforschung des Übergangs von Cluster-Systemen zu kollektiven Systemen. Die Partikel-Wechselwirkungen wurden mit einem optischen Diagnosesystem untersucht, das es erlaubt, die drei Ortskoordinaten jedes Teilchens gleichzeitig mit einer Zeitauflösung von 0.04 Sekunden zu bestimmen.

Die experimentellen Ergebnisse sind:
1. Die binäre Wechselwirkung zwischen den Partikeln enthält neben der abstoßenden Coulombkraft noch einen attraktiven Teil, der zum ersten Mal experimentell nachgewiesen wurde.
2. Die zeitliche Entwicklung der Dynamik zeigt die Tendenz der Systeme, sich dem Zustand der niedrigsten Energie durch Umordnung der Partikel zu nähern.
3. Die Vibrationen in einem Plasmakristall von 63 Partikeln stimmen gut mit den Schwingungen einer Kugel mit Oberflächenspannung überein. Das zeigt, dass bereits ein System von nur 63 Partikeln kooperative Eigenschaften besitzt.

Die Möglichkeit, frei schwebende Partikel zur Untersuchung der Plasmarandschicht zu verwenden, wurde betrachtet. Die Existenz verschiedener stabiler Regionen für die Mikropartikel in einer Sauerstoff-Plasmarandschicht hat den ersten experimentellen Beweis einer strukturierten elektronegativen Plasmarandschicht geliefert — eine Eigenschaft, die bis jetzt nur mathematisch und numerisch untersucht wurde.

Abstract

Particles of micrometer size externally introduced in plasmas usually find their positions of levitation in the plasma sheath, where the gravity force is compensated by the strong electric field. Here due to electrostatic interaction they form different structures, which are interesting objects for the investigation of strongly coupled systems and critical phenomena. Because of the low damping (e.g. in comparison to colloidal suspension) it is possible to measure the dynamics up to the relevant highest frequency (e.g. Einstein frequency) at the most elementary level of single particle motion. The task of this work was to analyze the three dimensional structure, dynamical processes and the limit of the cooperative behavior in small plasma crystals. In addition to the study of the systems formed, the immersed particles themselves may be used for diagnostics of the plasma environment: estimation of parameters or monitoring of the processes inside plasma.

The laboratory experiments are performed in two radio-frequency (RF) plasma reactors with parallel plate electrodes, where the lower electrode is a so-called "adaptive electrode". This electrode is segmented into 57 small "pixels" independently driven in DC (direct current) and/or RF voltage. When RF voltage is applied to one of these pixels, a bright localized glow, "secondary plasma ball", appears above. Three dimensional dust crystals with less than 100 particles are formed inside this "plasma ball" — the ideal conditions for the investigation of the transition from cluster systems to collective systems. The investigation of the particle interactions in crystals is performed with an optical diagnostic, which allows determination of all three particle coordinates simultaneously with time resolution of 0.04 sec.

The experimental results are:

1. The binary interaction among particles in addition to the repelling Coulomb force exhibits also an attractive part, which is experimentally determined for the first time.
2. Analysis of the dynamical evolution shows the tendency of the systems to approach the state with minimum energy by rearranging particles inside.
3. The measured 63 particles' crystal vibrations are in close agreement with vibrations of a drop with surface tension. This indicates that even a 63 particle crystal already exhibits properties normally associated with the cooperative regime.

The possibility to use levitated particles as a new powerful diagnostic of the plasma sheath region is proposed. The existence of different equilibrium positions of microparticles suspended in an Oxygen discharge provides evidence of a structured electronegative plasma sheath, a feature so far only mathematically and numerically investigated.

Introduction to complex plasmas

Ionized gases containing charged particles of solid matter are known as "complex" or "dusty plasmas". Complex plasmas are defined by the external introduction of micrometer size particles of solid matter into a laboratory plasma discharge. Dust particles form different structures in these plasmas, which obey both the discharge conditions and the force of gravity. Depending on the conditions these structures may stay in crystal-like or fluid-like states and then they are called strongly coupled. Dust particles may also experience a lot of thermal motion and then they are weakly-coupled in a gas-like phase. In this thesis the attention mostly will be paid to the study of crystalline systems. But at the same time the dusty plasma systems of different states are the subject of considerable interest in fundamental physics, plasma science, astrophysics as well as technological applications ([1], [2], [3]).

Initially, the interest to dusty plasmas came from astrophysics. Natural dust fills the universe. Interplanetary and interstellar clouds, comet tails consist of dust [4], [5]. The complex structure of planetary rings [6] and particle transport processes observed in those rings [7] are objects for dusty plasma investigation. Dust appears in the physics of magnetospheres and ionospheres as well.

Another field, where dusty plasma researches are of great interest is plasma processing. Here dust is often present as a consequence of sputtering from plasma reactor walls and electrodes. The formation of particles in low-pressure glow discharges during plasma-enhanced chemical vapor deposition (PECVD) of thin films for electronic applications has been considered as a trouble-making product for the films for a long time. The particle growth induced by gas-phase nucleation has been observed and studied in sputtering and reactive ion etching discharge conditions. In this case the atoms sputtered from the electrode materials are the primary source of nucleation. Therefore, controlling the particle behavior is regarded as essential for improving manufacturing techniques in many optoelectronic applications, such as solar cells or thin-film transistors in active-matrix liquid crystal displays [8]. To prevent or decrease the dust contamination, it is necessary to understand the physical processes of formation and growth of dust particles in gas discharge plasmas, the mechanism of their transport and the influence of dust on the plasma parameters.

Dust can also affect the plasma stability and operation of fusion devices ([9], [10]). The plasmas in tokamaks and stellarators contain impurities (dust), which are the result of several processes, such as desorption, sputtering, evaporation and sublimation of wall materials, etc. A high amount of dust can raise serious problems related to the safety of operation. For example, the tritium implantation into carbonaceous dust can result in the appearance of dust particles consisting of carbon and tritium. Due to the high mobility and chemical reactivity dust may operate as a potential carrier of tritium in the case of a severe reactor failure, contaminating substantial areas. Thus, the removal of dust from the thermonuclear devices represents both technical and the scientific problems.

But in the last years it has become obvious that the presence of dust in plasmas does not necessarily have undesirable consequences. Injected particles have some properties, which can be successfully used in industrial processes: very small size, monodispersity and high chemical activity. One of the possible applications is the creation of new nanostructure materials, like film deposition with specific inclusion of particles. At the beginning of the solar cell production, as it was mentioned above, dust was considered an undesirable side effect. But later it was shown that the incorporation of grown nanometer-sized crystalline dust particles in the amorphous silicon film can substantially increase the stability and efficiency of the solar cells [11]. The deposition of dust during the manufacture of nanostructured silicon can also accelerate the crystallization processes [12].

A number of unique properties (relative simplicity of observing, self-organization and formation of ordered structures [13], [14], [15], [16], fast relaxation and response to external disturbances) make complex plasmas very attractive and interesting objects for observations and also very effective instrument for studying the properties of strongly coupled systems, such as fundamental properties of crystals, etc at the kinetic level. The dust particles can usually be seen with the naked eye or easily visualized by optical techniques. This allows, for the first time, investigations at the kinetic level of such phenomena as phase transition, particle transport, limits of cooperative behavior, visco-elastic properties, etc. If in addition we take the ubiquity of dust in space and its importance in technology into account, we can conclude that the experimental and theoretical investigation of complex (dusty) plasmas is a very important in fundamental and applied physics. The present thesis is devoted to the study of individual dust particle behavior in small strongly coupled systems in a low temperature plasma environment.

Dust particles in plasmas create crystal structures due to strong electrostatic coupling. After being injected into the plasma the particle gets charged. The charge and potential of a body immersed in a low temperature plasma are determined by the balance between electron and ion currents to the body. Since electrons are more mobile than ions, a dust particle will acquire negative charge and negative potential in a plasma with respect to

the unperturbed plasma potential. The floating potential adjusts so that, by repelling the mobile electrons and attracting positive ions, the dust particle collects zero net current in the steady state. The charging time has been estimated numerically to be of the order of 10-20 μs for a micron size particle and typical discharge conditions (electron and ion temperatures and densities are: $T_e \sim 3$ eV, $T_i \sim 0.025$ eV, $n_i \sim n_e \sim 10^{15}\ m^{-3}$) [1]. On longer timescales the charge remains practically constant and experiences only small fluctuations around its equilibrium value [2].

The charging is generally governed by the collection of charged plasma particles (electrons and ions), but it also can be a result of thermionic, photoelectric or secondary electron emission. These processes are important for dust charging in the upper atmosphere [17], in space [18], in a plasma induced by UV irradiation or in a plasma with electron beams [2], etc. The emission of electrons increases the dust particle charge and it even can become positive. In the next chapter these processes will be discussed in more detail.

In a sense, the dust particle collecting currents from the plasma are similar to those of a microscopic probe. Therefore, the general aspects of probe theories are relevant to dusty plasmas. They are used for the quantitative description of the particle charging in gas discharge plasmas. Usually the particle charge Q is related to the particle surface (floating) potential V_s and it is calculated through vacuum capacitance:

$$Q = 4\pi\varepsilon_0 a V_s, \tag{1}$$

where ε_0 is the vacuum permittivity and a is the dust particle radius. The charging process determines the particle behavior in time and is very important for dusty plasma studies. Therefore, in chapter 1 we review the probe theories, which are used for the particle charge estimation.

The negatively charged particles in plasmas are influenced by an electric field. The equilibrium position of the particle is determined mainly by the balance between gravity and the electrostatic force:

$$m_p g = QE, \tag{2}$$

where m_p is the particle mass and g is the acceleration of gravity. Usually in laboratory experiments the electric field, E, is strong enough to compensate the gravitation force only in the region near electrodes (plasma sheath region), unless the particles are very small (tenth of microns), when they can levitate even in the bulk plasma.

Besides the electric force and weight of the dust there are many other forces known, which influence the single particle position, such as the ion drag force, neutral drag force, thermophoretical force and others. These forces become especially important in microgravity conditions, when one of the major forces, gravity, is absent. In order to study this effect,

the experiments on complex plasmas were started on board of the International Space Station in the beginning of 2001 (the PKE (in German, Plasma-Kristal-Experiment)-Nefedov experiment). The main feature of these experiments is that the particles do not levitate in the plasma sheath, but in the bulk plasma, since gravity is absent. New features then appear due to the "lesser" forces such as the presence of empty space (void) in the center of the particle cloud [19], which has been explained as a result of the ion drag force action [20].

A positive ion cloud is formed around each particle. Its size is related to the electron and ion Debye length, which is also called screening length, since it isolates the charge from the plasma environment. Outside the shielding sphere plasma can be considered as non-modified by the local point-like charge. But in the presence of many dust particles in a plasma (dust cloud), the usual situation in dusty plasma experiments that the particles may experience additional interaction (shadow force, wake potential, dipole-dipole interaction and others). Due to these forces dust particles self-organize into a variety of assemblies, in particular, chains or crystals with different kinds of like-lattice structures. The forces acting on single particles and between dust particles in plasmas will be considered in chapter 1 of this thesis.

As has been mentioned above, at usual laboratory conditions particles find their equilibrium positions inside the plasma sheath (where the electric field is strong enough to compensate gravity) and only under microgravity particles may populate in the plasma volume. In this work a specifically designed electrode has been used, which allows us to levitate dust particles of micrometer size in the plasma even in ground based conditions. This is the RF (radio-frequency with 13.56 MHz) "adaptive electrode", which is divided into many segments (pixels) with the possibility to apply DC (direct current) or RF voltage to each of these segments. This electrode can be operated to create a small "plasma ball" in the sheath region of the main plasma. The particles are collected to this small plasma region from their usual positions in the sheath. The "adaptive electrode" has been mounted in two different experimental set-ups, which will be described in detail in chapter 2.

After the visualization of a dust particle cloud it is important to analyze the properties of the whole structure (as a macro-system) and the characteristics of individual interactions between the particles. For this purpose we need to determine the particle positions. One of our experimental set-ups has a unique three-dimensional diagnostics, which allows us to determine all three particle coordinates simultaneously. This system is described in chapter 2. Such a possibility is very useful for the study of dust dynamics, because one can extract some information about the system only by observing "fast" events. Up to now vertically unstressed 3D crystals without strong additional confinement could only be obtained in microgravity conditions. With our "adaptive electrode" set-up it is possible to

get almost spherical 3D crystals in the small plasma above the driven pixel. Contrary to the sheath plasmas, where particles usually form vertical chain-like structures, the grains are found to organize themselves in well ordered spherical 3D structures. Crystals with small numbers of particles (from 4 up to 70), later they are called clusters, have been obtained and they are described in chapter 3. By varying the voltage applied to the pixel the positions of individual particles can be changed, thus, manipulation of dust particles using the "adaptive electrode" is achieved. The control of the particle positions is highly desirable in plasma processing of materials, e.g, for removal, as it has already been discussed above.

In chapter 3 the perturbation of the main plasma introduced by the RF biasing on the driven pixel of the "adaptive electrode" will be considered. The presence of the additional RF biased area in the plasma reactor changes the potential configuration in the chamber and, consequently, influences the dust particle positions. The calculation of the electric field, dust charge and levitation force of the particles are given in chapter 3.

In order to obtain a complete picture of all the interactions and confinement forces, knowledge of the plasma parameters is essential and the diagnostics of the plasma is a significant part of the investigations. In order to characterize the behavior of clusters it is necessary to know the parameters of the plasma at the position, where the clusters are situated. In our case the dust clusters are formed in a "plasma ball" of very small size (approximately 32 mm^3) and it is not easy to make diagnostics of such a plasma. One possible method is optical analysis. Spectroscopic measurement have been provided in order to obtain the density of the plasma above the pixel. The experimental methods and theoretical approaches of the spectroscopic analysis are presented in chapter 4. For the diagnostics of the main plasma volume Langmuir probes have also been used (see chapter 1 for the theory of electric probes and chapter 2 for the experimental methods of measurements).

The cluster formation is a very interesting phenomena in dusty plasmas. The forces, which keep the particles together in clusters, are still not understood completely. The screened Coulomb potential (or Debye-Hückel, Yukawa potential) is often applied to describe the electrostatic interaction between particles in dusty plasmas:

$$\varphi(r) = \frac{Ze}{r} \exp^{-r/\lambda_D}, \tag{3}$$

where $Z = Q/e$ is the particle charge number, λ_D is the Debye screening length, e is the electron charge, r is the distance between particles. A great deal of work is in progress on to identify also the possibility of attraction between particles. During our experiments with 3D clusters we have observed the spontaneous attraction between particles in the smallest

cluster obtained, the cluster of 4 particles, without any external perturbations. The force of repulsion and attraction during the particle motion has been estimated and is discussed in chapter 5. This force could be reconstructed using the three-dimensional diagnostics. The collective effects in the cluster of 73 particles are also analyzed (chapter 5).

Collective effects are important in large particle systems formed by hundreds or thousands of particles. In the experiments discussed in this thesis small cluster structures below 100 particles have been investigated in order to prove the collective (co-operative) limit. Therefore, a study of the particle dynamics and structure of two clusters of 17 and 63 particles have been performed. In both of these systems particle rearrangement was observed: in the cluster of 17 particles as a result of the addition of a new particle, in the cluster of 63 particles because of the removal of particles from the top of the cluster. In chapter 6 the energies of these two structures during the rearrangement is estimated. It has been found that the cluster relaxation obeys the principle of minimum energy: restructuring is going in a way to achieve the state with the smallest energy. Besides energy estimations, in chapter 6 the vibration of particles in these two clusters will be discussed. Fourier transform analysis shows that the cluster of 63 particles has characteristic frequencies of oscillations which agree well with those for a liquid drop, suggesting that the cluster of 63 particles can already experience the cooperative-like behavior. The cluster of 17 particles does not develop such oscillations.

Chapter 7 describes the behavior of dust particles in an electronegative discharge, in particular, in Oxygen gas. In this work the dust particles have been used as a diagnostic tool for the electronegative plasma sheath. The importance of studying electronegative plasmas is governed by the wide application of discharges with electronegative gases in plasma processing of materials (due to their high chemical reactivity). The other effect is the presence of negative ions, which influence all processes in the discharge. The degree of this influence depends on the amount of negative ions in the plasma volume. This amount is calculated as the density ratio of electrons to negative ions $\alpha = n_e/n_n$ – the plasma electronegativity. In our work dust particles together with Langmuir probes have been used to calculate α. For electronegative plasmas it has been theoretically predicted that due to the presence of negative ions the potential distribution in the plasma sheath is different from the electropositive plasma and at a certain value of the negative ion density the double layer can develop in the plasma sheath. This implies that particles should have several equilibrium positions in the electronegative discharge. In our experiments we have observed dust forming several equilibrium layers providing direct proof of these theories for the first time.

Chapter 1

Some theoretical aspects of complex plasmas

Complex (dusty) plasma physics is a very young field in plasma science, however, a large amount of work has already been done in this area. Before discussing the results obtained in the thesis a review of some theoretical and experimental aspects of dusty plasmas will be presented.

Since small pieces of solid matter (dust particles) levitate in the plasma environment, we give the determination of several main plasma parameters, which affect the particle positions. The radio-frequency (RF) capacitively coupled discharge and its plasma sheath will also be described, since this discharge is generally used in complex plasma experiments including ours. Particles injected in a plasma immediately get an electric charge, which is usually calculated by using the electric probe theory. For measuring plasma parameters in our experiments the probe diagnostics have been used. Therefore, in this chapter first of all the main models developed for the interpretation of the electric probe measurements will be considered. After that the behavior of a single particle in plasmas and the main forces acting on it will be described. Both the plasma processing and dusty plasma experiments usually involve hundreds or thousands of particles. In this case the collective effects become very important. At the end of this chapter a review of the main interaction mechanisms between the particles will be made. A large part of the field is devoted to the investigation of wave-related properties of dusty plasmas (i.e. dust acoustic waves, shock waves, instabilities, etc.) This subject, however, will not be considered in the thesis, since our experiments do not involve wave formation. An exception is an analysis of dust vibrations in 3D plasma clusters in chapter 6.

1.1 Basic plasma parameters

Plasma frequency

The plasma frequency is an important parameter in time dependent effects. There ion and electron plasma frequencies which describe electrostatic oscillation frequency appearing as a result of a small charge separation in a plasma:

$$\omega_{e,i} = \sqrt{\frac{n_{e,i}e^2}{\varepsilon_0 m_{e,i}}}, \tag{1.1}$$

where $\varepsilon_0 = 8.85 \cdot 10^{-12}\ Fm^{-1}$ is the vacuum permittivity, $n_{e,i}$ and $m_{e,i}$ are the densities and masses of electrons and ions, respectively, and e is the electron charge. The typical frequency used in the laboratory experiments in radio-frequency discharges (13,56 MHz) is between the ion and electron frequency. As a result, electrons follow the oscillations of the field applied and ions follow the time averaged field.

The dust particle ensembles oscillate around their equilibrium positions with a frequency [3]:

$$\omega_{pl} = \sqrt{\frac{n_p Z^2 e^2}{\varepsilon_0 m_p}}, \tag{1.2}$$

where n_p, m_p and Z are the density, mass and charge number of the dust particle.

Debye length

The small charged object (micrometer size dust particle) is effectively screened by the surrounding plasma. The screening length scale is determined by the Debye length. This is the characteristic distance, at which deviations from quasi-neutrality occur. The electron and ion Debye lengths $\lambda_{D_{e,i}}$ are:

$$\lambda_{D_{e,i}} = \sqrt{\frac{\varepsilon_0 k_B T_{e,i}}{e^2 n_0}}, \tag{1.3}$$

where k_B - the Boltzmann constant, $T_{e,i}$ - the electron and ion temperature, respectively, and n_0 - the plasma density. In our experiments the electron temperature is $T_e \approx 3$ eV, the ions have room temperature $T_i \approx 0.03$ eV and the plasma density is of the order of $n_0 \sim 10^{16}\ m^{-3}$. Substituting these values in eq. 1.3 the electron Debye length can be estimated as $\lambda_{D_e} \approx 120\ \mu m$ and the ion Debye length is $\lambda_{D_i} = 13\ \mu m$. In dusty plasmas a linearized Debye length is often used [3]:

$$\frac{1}{\lambda_D^2} = \frac{1}{\lambda_{D_e}^2} + \frac{1}{\lambda_{D_i}^2}. \tag{1.4}$$

Mean free path

Another important plasma parameter is the mean free path. This is the distance, which a plasma particle labelled 1, can travel without collision with another particle, labelled 2:

$$l_{mfp1} = \frac{1}{n_2 \sigma_{12}}, \tag{1.5}$$

where n_2 is the number density of the particles 2 and σ_{12} is the cross section for the collision of particle 1 with particles 2. For instance, in our experiments, the mean free path of the ions was of the order of 32 μm (at P = 60 Pa), which is much shorter than the electron Debye length (approximately 120 μm). Hence, we are dealing with collision dominated plasmas.

1.2 RF discharge and plasma generation

The radio-frequency (RF) plasma is commonly used in laboratory research as well as for industrial applications. Such plasmas are created by applying high frequency (MHz) sinusoidal voltage to one of the chamber electrode with following acceleration of the charge carriers (electrons) and gas ionization. The properties of the RF discharges considerably depend on the frequency of the applied voltage. Usually, industrial and laboratory systems are designed for 13.56 MHz, the international standard commercial frequency. We used the capacitively coupled RF discharge in the parallel plate configuration. The plasma is created by applying an electric field between two electrodes (lower electrode is grounded, the upper one is driven). In spite of the relative simplicity of a parallel plate discharge, it is difficult enough to understand all its internal processes [17]. A full analysis is beyond the scope of this work, here some typical features of an RF discharge will be recalled. The important thing is that ions do not follow the RF cycles, because of their large mass, but electrons do.

In the usual RF plasma reactors the space charge sheath separates electrodes from the plasma glow. The space charge RF sheath is a very important part of an RF discharge, especially in our investigations, since the dust particles usually levitate in the sheath near the lower electrode. A sheath, in general, is the positive-space-charge region, which develops in plasmas near a solid surface. The formation of the positively charged region is caused by the fact, that when a solid-state body comes in contact with the plasma, the charge carriers (electrons and ions) are absorbed on its surface. Initially, the electron flux is much larger than the ion flux, because of the difference in mobilities of these two species. If a surface is floating the fluxes have to be equal to each other. Thus, an immersed body

(e.g. chamber wall, floating electric probe or injected dust particle) gets negatively charged and repels electrons and attracts positive ions. When the dimensions of a body is larger than the Debye length, a positive space charge region is formed in front of the body surface ($n_i \gg n_e$). The sheath lengthscale is typically a few Debye lengths. Since there are few electrons in the sheath to excite the gas, this region appears dark to the eye.

If we compare the sheath width (or roughly the Debye length) with the mean free path of the charge carriers (electrons and ions), it is possible to classify the types of sheaths as collisional $l_{mfp} \ll \lambda_D$ or collisionless $l_{mfp} \gg \lambda_D$. An increase of the pressure in a plasma chamber may lead to a transition from a collisionless to a collisional sheath. Another classification of the sheaths is based on the comparison between the curvature radius r of the solid body, which is in contact with the plasma, and the Debye length λ_D. If $\lambda_D \ll r$ we have a thin sheath, in the opposite case $\lambda_D \gg r$ we have thick sheath.

In original work Langmuir [21] assumed that the potential drop from the floating potential of a body immersed into a plasma occurs across the sheath and plasma was entirely field-free. But later Bohm [22] provided a criterion for the location of transition from the quasi-neutral plasma to the sheath region. With the assumption of negligible ionization inside the sheath, a negligible electric field on the sheath edge, monoenergetic ions and Boltzmann electrons, Bohm found that in order to form a sheath positive ions must have a certain minimum energy. In terms of velocity the Bohm criterion is:

$$v_{Bohm} \geq \sqrt{\frac{k_B T_e}{m_i}}. \tag{1.6}$$

This equation implies that the electric field must exist inside the plasma in order to accelerate ions.

1.3 A single charged particle in complex plasmas

As it has already been mentioned in the Introduction, a dust particle immersed in a discharge is getting charged. The balance of gravity and electric field usually confines the particle clouds near the lower plasma boundary, where they form different crystallized or fluid systems [13]. However, besides these two main forces some others influence the particle positions as well. A fundamental issue is the nature and strength of the (binary and collective) forces, which act on the dust particles in plasmas. In this section we will consider elementary processes and main forces on a single charged particle in plasmas.

1.3.1 Charging and electrostatic potential around a particle

The ion and electron fluxes are directed to the surface of an uncharged particle placed in a plasma. Since a small dust particle may be considered as a spherical floating probe in plasma, the probe theory can be used to describe the charging process. It is usually assumed that the ion and electron recombination and absorbtion take place on the particle surface; neutrals, which are created as a result of the recombination, can either remain on the surface or leave back to the plasma. As it has been already mentioned, the dust particle acquires negative charge because the electron flux is larger than the ion flux. After that the charge remains almost constant and only experiences small fluctuations due to the stochastic nature of the charging process. For the quantitative description of the particle charging the most frequently used approach is the *Orbital Motion Limited theory* (OML). The applicability conditions for this theory are often formulated as:

$$a \ll \lambda_D \ll l_{mfp}, \tag{1.7}$$

where a is the radius of a probe or a particle. Since the dust particle radius is much smaller than the Debye length in a plasma its capacitance is close to that in a vacuum, as it has already been pointed out in the Introduction:

$$Q = 4\pi a \varepsilon_0 V_s. \tag{1.8}$$

The inequality $\lambda_D \ll l_{mfp}$ implies that the plasma is collisionless and is very important to apply OML theory for the surface potential determination. The question of the validity of OML theory in dusty plasmas is still open. In several works the plasma regimes, at which OML may be used, are specified ([23], [24], [25]). The probe theories will be considered in detail in the next section, since they are an important subject in the present research.

The charge of a particle can be influenced by other secondary processes like secondary electron emission, photoemission, and thermionic emission. In gas discharge these processes are usually neglected. However, in other situations they can substantially affect the charge and it can even acquire positive values ([26], [2]). Also if the dust concentration is sufficiently high in a plasma, the particle surface potential and, hence, the charge can decrease ([26],[2]).

The potential distribution around an isolated spherical particle in plasmas is governed by the Poisson equation:

$$\frac{d^2V}{dr^2} + \frac{2}{r}\frac{dV}{dr} = -4\pi e(n_i - n_e), \tag{1.9}$$

with the boundary conditions $V(\infty) = 0$ and $V(a) = V_s$. The particle charge $Q = Ze$ is

related to the surface potential V_s as :

$$\frac{dV}{dr}|_{r=a} = -\frac{Ze}{a^2}. \tag{1.10}$$

Note, that eq. 1.10 coincides with eq. 1.8 for the Coulomb potential in the vicinity of the particle. If the Boltzmann distributions of electrons and ions holds, the condition $|eV_s/T_{ei}| < 1$ is satisfied, and the right hand side of the Poisson equation can be linearized yielding:

$$V(r) = V_s(a/r)\exp\left\{-\frac{r-a}{\lambda_D}\right\}, \tag{1.11}$$

where λ_D is the linearized Debye length, $\lambda_D^{-2} = \lambda_{De}^{-2} + \lambda_{Di}^{-2}$. For small particles, when $a \ll \lambda_D$, we get:

$$V(r) = (Ze/a)\exp\left(\frac{-r}{\lambda_D}\right), \tag{1.12}$$

since $V(s) = (Ze/a)(1 + a/\lambda_D)^{-1} \approx Ze/a$. This is the screened Coulomb or Debye-Hückel (Yukawa) potential, which is often used to describe the electrostatic interaction between dust particles in plasmas. If the surface potential is not small in comparison with the temperatures of electrons or ions, then it is only possible to use this expression at large enough distances from a particle. The surface potential in this case should be replaced by some "effective potential" V_{eff}, with $|V_{eff}| < |V_s|$. Effective potential can be calculated numerically with known plasma parameters [27].

The equilibrium isotropic case considered above is rarely realized in dusty plasmas. First of all in laboratory plasma experiments the ions often have some directed velocity relative to dust particles. For instance, this happens in the plasma sheath, where the particles are usually situated. Downstream from the particle there is a perturbed plasma region – ion wake, where the potential has a periodically oscillating character with decay [2], while upstream from the particle the potential has a form of a screened Coulomb potential. Besides, the distribution of the potential is influenced by ion-neutral collisions. For example, Zobnin *et al.* [28] have shown, that with an increase in collisionality there can be a transition from the Yukawa potential to the unscreened Coulomb potential. Although there is plenty of research devoted to the calculation of the distribution of the electrostatic potential around a dust particle and its dependence on plasma parameters ([23], [29], [30]), this problem is not completely solved yet.

1.3.2 Electric probe theories and the particle charging process

The electric probe method of plasma diagnostics is widely used for studying the parameters of gas discharges. A considerable advance has been made since Langmuir's pioneering

Figure 1.1: The probe circuit.

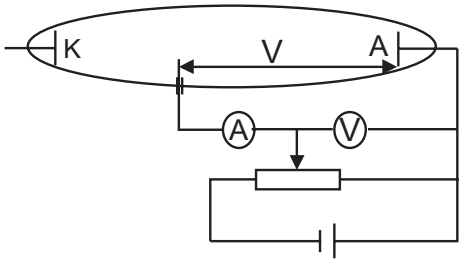

works during the years 1923 to 1935 [21]. Essentially, the electric probe is a small metallic electrode (usually, a wire), which is immersed into a plasma. The probe is connected to a power supply, which allows to maintain the different voltages on the probe (positive or negative with respect to the plasma potential). From the current gathered by the probe the different plasma parameters can be extracted. The simplest circuit of the probe measurements is shown in Fig. 1.1.

The advantage of the electrical probe method over other methods of plasma diagnostics is that the diagnosis can be performed using relatively simple apparatus. In addition, this method is frequently capable of measuring local values of the plasma parameters. Most of the other diagnostics give values of the plasma parameters averaged over a relatively large volume. Although experimentally this method seems to be relatively simple, it is much more complicated from the point of view of theoretical analysis. The reason for the difficulties is the diversity of the plasma regimes, ranging from partially ionized gases at very low pressures to highly ionized gases at high pressures, so they require different theoretical models.

The current collected by the probe, which in general consists of an ion current and an electron current and can be determined for various values of external voltage applied to the probe. This dependence is known as a probe characteristic or current-voltage characteristic (IV-characteristic) and shown schematically in Fig. 1.2.

The qualitative interpretation of current-voltage characteristic will be given below. At the point V_p the probe has the same potential as the plasma, there is no electric field and charged particles can reach the probe only due to their thermal velocity. This value V_p is called space or plasma potential. As electrons are much faster than ions, the probe mainly collects electron current. If the probe is positive with respect to the discharge (section EF), then electrons are accelerated to the probe and ions are retarded. Thus, there is a negative space charge at the probe surface, which rises until it is equal to the

Figure 1.2: The probe characteristic.

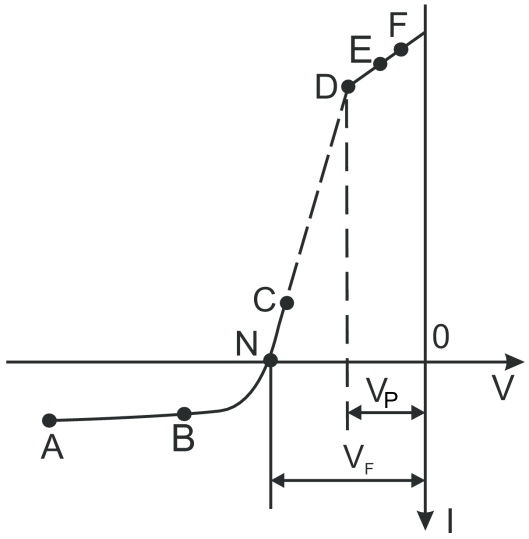

positive charge of the probe. This charged shell ("sheath") is usually very thin and does not disturb the surrounding plasma. Further, increasing of the probe voltage does not change the area of the sheath and saturation of the electron current occurs. When the probe is strongly negative with respect to the surrounding plasma the electrons are repelled from the probe while the ions are attracted. A positive space charge sheath is formed around the probe. In this regime the electron current decreases. Finally, at the point V_F the probe retards almost all electrons, except for a small quantity, whose flux is equal to the ion flux and the resulting current is equal to zero. The potential at which this occurs is usually called "floating potential" and it is the potential that an isolated probe would reach if it is immersed in a discharge. At a more negative voltage almost all electrons are retarded and saturation of the ion current takes place (section AB).

The saturation regimes on sections AB and EF are, in principle, similar, however, there are two different features (except the difference in ion and electron masses). Firstly, the electrons are much hotter than the ions. Secondly, electrons are much more affected by a magnetic field. In most of the calculations the electron part of the IV-characteristic is used. But sometimes, for example, at the presence of a magnetic field, only the ion part can be used. Let us consider the elementary treatment of the positive and negative current collection on the probe.

The first attempt to develop a theory for the positive collection was made by Langmuir and Mott-Smith [31]. In this work it was assumed that the negative probe is surrounded by two regions: the positive ion space charge sheath and the undisturbed quasi-neutral

plasma. But, as pointed out by Swift [32], there is a region between the plasma and the sheath, in which electrons and ions have almost the same densities, but it is already modified due to directed motion of the ions to the probe. This region is the transition quasi-neutral region or the so-called "presheath".

Most of the potential drop occurs across the inner sheath and only a relative small drop occurs across the transition quasi-neutral region. Therefore at the sheath boundary the ions have a directed motion towards the probe. Thus, the ions are gathered not by the surface of the sheath, but by a larger surface of the transition quasi-neutral region. The positive ions require a certain minimum energy before the sheath can form and this causes the potential drop in the pre-sheath. According to the Bohm criterion [33]:

$$e\triangle V \geq \frac{1}{2}k_B T_e, \tag{1.13}$$

where $\triangle V$ is a potential drop between the sheath edge and the undisturbed plasma, and the electrons assumed to have the Maxwell-Boltzmann distribution with a temperature T_e. For the radial velocity of the ions at the sheath boundary we have:

$$v_s = \sqrt{\frac{-2e\triangle V}{m_i}}, \tag{1.14}$$

where m_i is the ion mass. The electron concentration at the sheath boundary is given by:

$$n_e = n_{e0} \exp\left\{\frac{e\triangle V}{k_B T_e}\right\}; \triangle V < 0. \tag{1.15}$$

n_{e0} is the electron concentration in the undisturbed discharge. Since the ion and electron concentrations at the sheath edge are still approximately equal, we have for the ion current I_i [32]:

$$I_i = n_{e0} \exp\left\{\frac{e\triangle V}{k_B T_e}\right\} \sqrt{\frac{-2e\triangle V}{m_i}} A_s; \triangle V < 0, \tag{1.16}$$

where A_s is the area of the sheath surface. In many cases (thin sheath) the area of the probe can be used instead of A_s. If the probe is made very negative there is some increase in A_s.

Now let us consider the case of the electron collection by the positive probe (section CD in Fig. 1.2). Here some of the electrons can overcome the retarding potential between the probe and the discharge. In the case of the Maxwellian electron distribution and negligible number of collisions between electrons and molecules of a gas inside the sheath, the electron current I_e is given by

$$I_e = I_0 \exp\left\{\frac{eV_p}{k_B T_e}\right\}, \tag{1.17}$$

Figure 1.3: The semi logarithmic dependence of the probe current on the applied voltage. Picture is taken from [32].

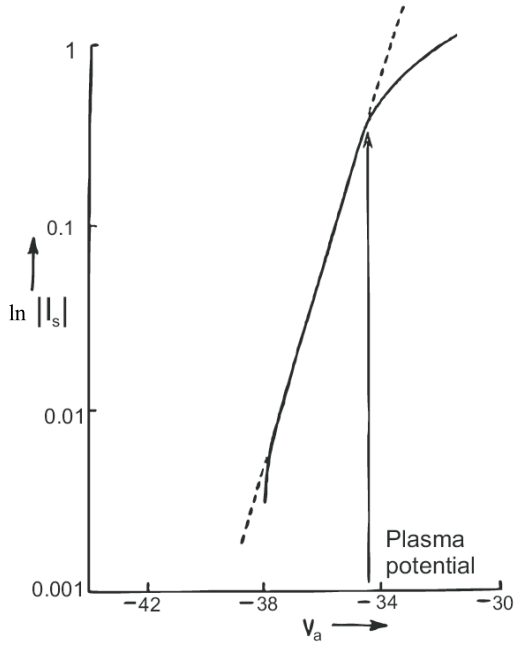

where I_0 is the electron current reaching the probe, when it is at the plasma potential [32]:

$$I_0 = -\frac{1}{4} n_{e0} \bar{c}_e e A_p = -n_{e0} e A_p \sqrt{\frac{k_B T_e}{2\pi m_e}}. \tag{1.18}$$

A_p is the surface area of the probe and $\bar{c}_e = \sqrt{8kT_e/\pi m_e}$ the electron thermal speed.

From the dependence of the current collected by the probe on the voltage the plasma parameters can be obtained. The slope of the graph of $\ln |I_s|$ (I_s is a probe current) versus the applied voltage V_a can be used to obtain the electron temperature T_e (Fig. 1.3) in the regime, where the current is dominated by the electrons:

$$T_e = \frac{e}{k_B} \frac{1}{\tan \psi}, \tag{1.19}$$

where ψ is the angle of the slope of the linear part in Fig. 1.3.

This plot also can help to obtain the plasma potential, which corresponds approximately to the start of the deviation of the semi logarithmic characteristic from linearity (Fig. 1.3).

The electron current at the plasma potential yields the electron density:

$$n_{e0} = \frac{4 I_0}{e \bar{c}_e A_p}. \tag{1.20}$$

The dust particle inserted in a plasma is, in essence, an isolated probe at the floating potential. Therefore, the electrostatic probe theories can be applied to describe the dust particle charging.

The probe theories

There are, essentially, two major theories that consider the electron and ion current to the probe immersed in a plasma. They differ by the assumptions concerning the ion collection. These theories are:

1. *The Radial Motion Theory* developed by Allen, Boyd and Reynolds [34](ABR theory), in which ions approach the probe surface radially (i.e.with zero angular momentum).

2. *The Orbital Motion Theory* (OM theory), in which ions approach the probe with a non-zero angular momentum. This theory was firstly developed by Mott-Smith and Langmuir [35]. But in their work several incorrect assumptions were made. Their primary fallacy was the assumption that the entire probe potential is developed across the sheath, and they did not assume the existence of small fields in the plasma. Bohm in 1949 [22] showed that such field must exist. In the general OM theory the probes have an associated absorption radius, r_A ($r_A > r_{probe}$, r_{probe} - probe radius), for each distinct ion energy, such that, if an ion crosses r_A in its orbit, it will necessary hit the probe. However, for small probe radii, $r_{probe} \ll \lambda_D$ (such as most dust grains) or for hot ions this absorption radius can be neglected and simpler *Orbital Motion limited* (OML theory) may be used. Another simplification is that of Bohm, Burhop and Massey [36], who considered an absorption radius, but assumed a monoenergetic distribution of ions. Also the OM theory was extended by Bernstein and Rabinovitz [37] and by the voluminous report of Laframboise [38].

In this chapter the overview of the existing theories for the determination of the plasma parameters from IV-characteristic of the electrical probe will be presented.

Orbital Motion Limited Theory

The orbital motion limited theory is a simplified case of the full orbital motion theory. It is based on the conservation of the angular momentum and the energy in a central field of the force. The angular momentum J of a particle with respect to the probe center is:

$$\vec{J} = m\vec{v} \times \vec{r}, \tag{1.21}$$

where $\vec{r}$ is the position vector of the particle and $\vec{v}$ is its velocity.

In Fig. 1.4 the particle trajectories with respect to the probe surface are shown. An arbitrary angular momentum may always be characterized by a parameter h called *the impact parameter*. This parameter defines the distance, by which the particle on its zero-potential

Figure 1.4: Sketch of the particle trajectories near the probe (dust particle) surface in the case of attractive interaction.

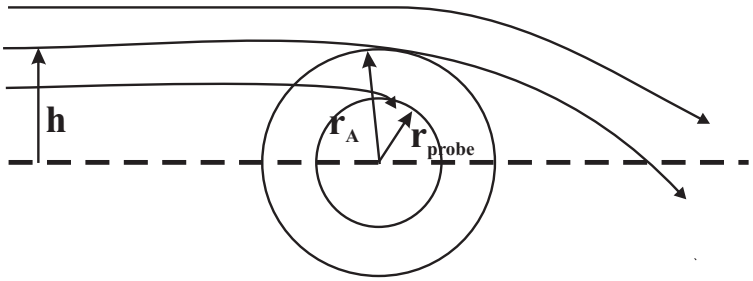

trajectory would miss the probe center. If the length of the probe is large compared with its radius then the charged particles (electrons and ions) move in a central field of the force and the angular momentum and the energy are conserved. The conservation of the angular momentum gives [39]:

$$mv_p a = mv_0 h, \tag{1.22}$$

where a and v_p are the particle radius and the velocity at the surface of the probe, and v_0 is the particle velocity far from the probe. The conservation of energy gives:

$$\frac{1}{2}mv_0^2 = \frac{1}{2}mv_p^2 \mp e\phi_p, \tag{1.23}$$

where a negative sign corresponds to electrons and a positive sign corresponds to singly charged ions, and ϕ_p is the probe potential.

Combining these two conservation laws we can get the expression for the impact parameter of a particle that just grazes the probe surface:

$$h_p = a(1 \pm \frac{\phi_p}{\phi_0})^{\frac{1}{2}}, \tag{1.24}$$

where the positive sign corresponds to electrons and ϕ_0 is the potential far from the probe. h_p can be taken as an effective radius of the probe. The only particles with an impact parameter less than h_p will strike the probe. The other particles may be deflected, but they will not contribute to the particle flux at the probe surface.

In [39] Allen gives the equations of the current to a spherical probe for attracting potential:

$$I_{e,i} = 4\pi a^2 n_0 e(k_B T_{e,i}/2\pi m_{e,i})^{\frac{1}{2}}(1 \pm e\phi_p/k_B T_{e,i}). \tag{1.25}$$

and also for retarding potential:

$$I_{e,i} = 4\pi a^2 n_0 e(k_B T_{e,i}/2\pi m_{e,i})^{\frac{1}{2}} \exp(\pm e\phi_p/k_B T_{e,i}). \tag{1.26}$$

The positive sign always goes with the expression for electrons.

An important assumption in the OML theory, that some of the charged particles in any particular energy range hit the probe at the grazing incidence, was made. However, this assumption does not hold in some cases and an absorption radius appears there, which should replace the probe radius. An absorption radius might exist outside the probe, such that particles, which cross it are destined to hit the probe [39].

Orbital Motion Theory and Absorption Radius

When a mass moves relative to a fixed point, it possesses an angular momentum given by the equation (1.21) above. In Swift and Schwar [32] it is shown that the angular momentum can be treated as an effective radial potential energy. This energy can be added to the electrical potential considered in the OML theory. In this theory the potential was purely attractive or retarding depending on the type of the particle and the probe voltage. When the effective potential is added to the electrical potential, the radial potential eventually takes on a retarding character for all values of the angular momentum except zero. The radial motion of a particle in the central field of the force is fully determined by the effective potential and energy, which consists of the interaction energy and a term arising from the conservation of the angular momentum.

The Fig. 1.5 from Bernstein and Rabinowitz [37] shows a family of curves for the effective potential $U_{eff}(r)$ for an attractive center. The lowest curve is for the zero angular momentum (pure radial motion). As soon as the angular momentum becomes non-zero, the shapes of the curves change dramatically. The contribution due to the angular momentum conservation dominates at small radii, causing an extreme repulsion there. For small values of the angular momentum the curves exhibit a single minimum at a sufficiently small radius. Following Bernstein and Rabinowitz, the maximum value of angular momentum for which there is only one local extremum, is denoted by J_a. The curves for values of angular momenta greater than J_a, but below a critical value J_c, $J_a < J < J_c$, have two local extrema: a minimum at a smaller distance and a maximum at a larger distance. Then they approach the $E = 0$ asymptotic limit from the positive side. E is the total energy of the orbiting particle. Curves for $J > J_c$ have no local extrema: the effective potential monotonically decreases with the distance towards to zero.

There are the different cases depending on the value of the angular momentum J. If $0 < J^2 < J_a^2$, for a probe radii larger than the critical value, all particles with this angular momentum and non-negative energy will hit the probe. If the probe radius is less than

Figure 1.5: The family of curves for the effective radial potential due to an attractive electric interaction and the conservation of angular momentum (picture is taken from [37]).

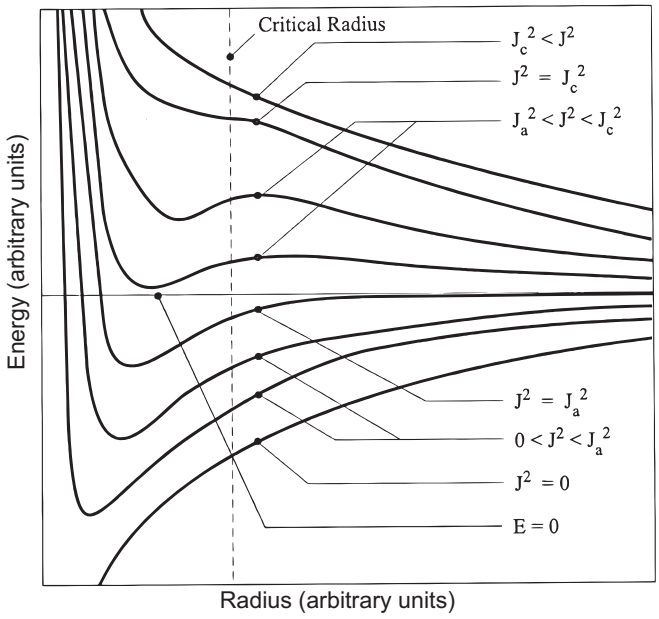

this value, only particles with this specific angular momentum and an energy greater than the intersection of the potential curve and the critical radius can reach the probe.

When $J^2 > J_c^2$, there is no extrema and only particles with the energy greater than or equal to the intersection of the appropriate potential curve and probe radius can hit the probe.

The most complicated situation is when $J_a^2 < J^2 < J_c^2$. Here the curve of potential has its local maximum and the behavior of the charged particles (electrons and ions) depends on their energy and the probe radius. The radial position of this local maximum is called *the absorption radius*. In order to reach the probe a particle should have enough energy to overcome the local maximum. In the case of a very small probe radius there is an effect of the potential well on particles. And only the particles with an energy which is greater than the local maximum can reach the probe.

The expressions for the floating potential and the probe current for the OM theory are not presented here. They are much more complicated than the OML theory yields and require an exact knowledge of the spatial variation of the potential to obtain numerical values. For example, Kennedy and Allen in [24] describe the solutions for the OM theory in a range of parameters applicable to dusty plasmas.

Also collisions can affect the charged particle energies. As it is mentioned in [40], even rare ion-neutral collisions in the sheath around the probe (dust particle) may affect the

particle charging. As it has been noted in [41] and in [42] the collisions in the sheath cause the destruction of the ion orbital motion. When an ion collides with a neutral in the sheath it loses energy, becomes trapped by the negative potential and will eventually reach the probe. Especially effective are charge-exchange collisions, which result in appearance of low energy ions from neutrals. The probability of these low energy ions to be absorbed by the probe is very high. Thus, when an ion experiences not too many collisions in the sheath region, the collisions lead to an increase of the ion flux to the probe. At high gas pressure ions make many collisions, since they are very mobile. With decreasing pressure the ion mobility decreases and, hence, the ion flux to the probe decreases as well.

These assumptions have been used by Khrapak *et al.* in [43] to estimate the ion current to the negatively biased probe in the presence of ion-neutral collisions. The comparison of experimental data with the theoretical model demonstrates that under typical experimental conditions in laboratory complex plasmas the particle charge is considerably reduced compared to the prediction of the OML theory.

Annaratone *et al.* [44] have estimated the criterion of the validity of the OML theory. They showed that the OML theory will fail in a collisional non-infinite plasma at the angular momentum limit based upon the ratio of the mean free path l_{mfp} to the probe radius r_p. They estimated the maximum angular momentum of the particle in a collisional non-infinite plasma as $J_m \simeq m_i(2E_0/m_i)^{1/2} l_{mfp}$, where E_0 is the energy of ions with a mass m_i at infinity. The angular momentum calculated through the collisionless OML theory was represented as $J = m_i(2E_0/m_i)^{1/2}(1 - e\phi_p/E_0)^{1/2} r_p$. Here ϕ_p is the potential of the probe, which is negative.

If $J_m < J$ OML will fail. The authors also have presented the expression, when OML is valid, as following :

$$l_{mfp} > r_p(-e\phi_p/k_B T_i)^{1/2}. \tag{1.27}$$

Khrapak *et al.* [43] proposed another approximate criterion of the validity of the collisionless OML theory:

$$l_{mfp} > 0.1 \left(-\frac{e\phi_p}{k_B T_i}\right) \lambda_D. \tag{1.28}$$

It shows that OML can fail even when the ion mean free path is considerably larger than the plasma screening length. The validity of the OML theory has also been discussed in the paper of Allen *et al.* [23]. All these criteria of validation are highly relevant to the field of dusty plasmas, where this theory is often used.

Radial Motion Theory

The radial motion theory is the limiting case of orbital motion theories. It is the case of the OML theory, when the impact parameter goes to zero $h \to 0$ and zero angular momentum for the OM theory $J \to 0$. In the paper of Allen, Boyd and Reynolds [34] it has

been shown that for spherical probes after the attracted particles have been accelerated to an energy much larger than their thermal energy, their velocity is purely radial. A small angular momentum means low temperature of charged particles or it is destroyed because of collisions.

For both the OML and OM theories the existence of plasma sheaths is either neglected or it is assumed to have a discontinuous boundary. In contrast, the Allen-Boyd-Reynolds (ABR) model includes a so-called "presheath". This is a transition region, where quasi-neutrality still hold, but the potential is of the order of the Bohm potential [22]:

$$\phi_{Bohm} \geq \frac{k_B T_e}{2e}. \tag{1.29}$$

So there exist three regions in a plasma: the quasineutral plasma, the presheath and the space-charge region (sheath). It is difficult to identify boundaries between these regions. The results of the papers [45], [46] demonstrate that it is almost impossible to identify the inner boundary between the transition region and the plasma sheath in highly collisional plasmas.

The radial motion theory as well as the theories of orbital motion have limits of validity. In the work of Nairn *et al.* [25] a brief analysis of these limits is presented. The ABR theory can be used, when:

- the ion temperature is much smaller than the electron temperature, $T_i \ll T_e$;
- the plasma is collisional, which prevents using orbital motion theories.

The first condition is usually fulfilled in the low pressure laboratory plasmas and it has been discussed already (see e.g. [34], [47] and [38]).

The OML theory will fail and the ABR theory is used, if:

$$l_{mfp} < r_p(-e\phi_p/k_B T_i)^{1/2}, \tag{1.30}$$

as discussed above.

This criterion refers to the necessity of some collisions in the plasma region. But the authors of ref. [25] have noted the important point: the ABR theory is a collisionless theory and requires the collisions to be rare in the sheath. They have estimated the thickness of the sheath and have deduced a second necessary condition for the validity of the radial motion theory:

$$l_{mfp} > 1.5\sqrt{J_i}\lambda_D, \tag{1.31}$$

where J_i is a normalized ion current to a sphere:

$$J_i = I_i \left[\frac{e}{4\pi\varepsilon_0} \sqrt{\frac{m_i}{2Zk_B^3 T_e^3}} \right]. \tag{1.32}$$

Here I_i is the total ion current to a spherical probe, m_i is the mass of ions, Z is the ion charge.

Some estimations of the validity of the ABR theory from experiments in radio-frequency plasmas have been produced by Annaratone *et al.* [44].

Summary of motion theories

Some analytical results for the positive ion current to a negative probe will be summarized. Some theories do not have an analytical solution (the case of a large sheath) and the results have to be presented graphically.

The earliest theory of Mott-Smith and Langmuir [35] assumes no absorption radius. This is the OML theory with Maxwellian ions, which yields:

$$I = 4\pi a^2 n_0 e \left(\frac{kT_i}{2\pi m_i} \right)^{1/2} \left(1 - \frac{e\phi_p}{k_B T_i} \right)^{1/2}. \tag{1.33}$$

The theory of Bohm, Burhop and Massey [36] takes the existence of the absorption radius (Orbital motion theory) into account and assumes monoenergetic ions ($T_i/T_e \neq 0$). Here two expressions for the ion current are presented:

$$I = 0.57(4\pi a^2) n_0 e \left(\frac{k_B T_e}{m_i} \right)^{1/2} \tag{1.34}$$

for $T_i/T_e = 0.01$ and

$$I = 0.54(4\pi a^2) n_0 e \left(\frac{k_B T_e}{m_i} \right)^{1/2} \tag{1.35}$$

for $T_i/T_e = 0.5$.

The radial motion theory (ABR theory) of Allen, Boyd, Reynolds [34] assumes cold ions ($T_i/T_e \to 0$), which do not have an angular momentum and gives the following expression for the ion current in the case when the sheath length is comparable with the probe radius:

$$I = 0.61(4\pi a^2) n_0 e \left(\frac{k_B T_e}{m_i} \right)^{1/2}. \tag{1.36}$$

Bernstein and Rabinowitz in their theory assumed cold ions, but allowed the existence of the absorption radius. The results are presented graphically for the case of a thick sheath [37].

After summarizing the probe theories it can be concluded that the experimental work

from the literature in most of the cases use the more simple ABR theory rather than the more complicated orbital theories [44].

1.3.3 The forces acting on a single particle in plasma

Gravitational force

The position of a small particle in a discharge is strongly dependent on the gravitational force, which is acting downwards. For a spherical particle it is determined as following:

$$\overrightarrow{F}_g = m_p \overrightarrow{g} = \frac{4}{3}\pi a^3 \rho \overrightarrow{g}, \tag{1.37}$$

where ρ is the particle density, $\overrightarrow{g}$ is the gravitational acceleration, m_p and a are the particle mass and radius, respectively.

Electric force

If an electric field E is present in a plasma, it exerts a force on a charged particle. The electrostatic force for a conducting particle [48] is:

$$F_e = ZeE\left[1 + \frac{(a/\lambda_D)^2}{3(1 + a/\lambda_D)}\right], \tag{1.38}$$

where Z is the particle charge number. The effective electric field can be introduced as:

$$E_{eff} = E\left[1 + \frac{(a/\lambda_D)^2}{3(1 + a/\lambda_D)}\right], \tag{1.39}$$

and then the force can be written as:

$$F_e = ZeE_{eff}. \tag{1.40}$$

Usually in dusty plasmas the radius of a particle is much smaller than the Debye length, $a \ll \lambda_D$. Thus, the electric force can be re-written simply as:

$$F_e \simeq ZeE. \tag{1.41}$$

Electric and gravity forces are often the main forces defining the particle position in a discharge. Even in the case of small particles (around several microns), they levitate in the sheath area close to the lower electrode in the plasma discharge, where the electric field is strong enough to compensate the particle weight. Only sub-micron particles can levitate in the plasma bulk region characterized by a weak electric field.

There is another effect caused by the electric field. In a vicinity of a dust particle the

polarization of a plasma induced by an external electric field occurs. This polarization leads to the appearance of the dipole momentum $p \approx a^3 E_{eff}$, which is directed along the field. Since $a \ll \lambda_D$ usually holds in complex plasmas, polarization momentum is similar to that of a conducting sphere in vacuum $p \approx a^3 E$. In the presence of an external nonuniform field the force acting on such a dipole is:

$$F_{dp} = (p\nabla)E. \tag{1.42}$$

The particle dipole-dipole interactions will be discussed later in this chapter.

Thermophoretic force

If there is a temperature gradient in the neutral gas, the thermophoretic force will act on a particle. This force will push the particle in the direction of low temperatures because of the larger momentum transfer from neutrals in the region with higher temperatures. In the case of a full accommodation the thermophoretic force can be expressed as follows [49]:

$$F_{th} = -\frac{4\sqrt{2\pi}}{15}\frac{a^2}{v_{Tn}}\chi_n \nabla T_n, \tag{1.43}$$

where χ_n is the thermal conductivity coefficient of gas. From the estimation of this coefficient [17] $\chi_n \approx C\bar{v}\sigma_{tr}$, where C is a coefficient of the order of unity, $C = 5/6$ for atoms, $C = 7/6(9/6)$ for diatomic molecules with unexcited (excited) vibrational states, respectively, σ_{tr} is the transport scattering cross section for gas atoms or molecules, $\bar{v} = \sqrt{8T_n/\pi m_n}$. If we put $C = 5/6$ in eq. 1.43 we get:

$$F_{th} \approx -\frac{16}{9}\frac{a^2}{\sigma_{tr}}\nabla T_n. \tag{1.44}$$

Thus, the thermophoretic force depends on the particle radius, gas type (through σ_{tr}) and temperature gradient, but does not depend on the gas pressure and temperature. Much work is devoted to experimental investigation of the influence of thermophoretic forces on the behavior of dust particles in discharges. In particular, in ref. [50] it is shown that the thermophoretic force can be used for levitation of particles and controlled influence on the ordered dust structures. In our experiment we also have measured the thermophoretic force, which can possibly influence the particle positions. The results are given in chapter 3.

Ion drag force

The ion drag force is the force connected to the momentum transfer from plasma particles to a dust particle. This momentum transfer appears if the average speed of ions is different from zero with respect to a dust particle. The relative motion of ions and dust particles can be connected to the influence of an external electric field as well as to the

thermal motion of dust particles with respect to a stationary gas of ions. The momentum transfer takes place in inelastic collisions (absorption of ions by a dust particle) as well as in elastic collisions (scattering of ions in the electric field of a particle). The influence of this force on various processes in plasma was studied even before the beginning of active researches in the field of dusty plasmas [51]. Now it is believed that the ion drag force influences and in some cases defines the position and configuration of dust structures in laboratory experiments [52], [53]. It is also responsible for the rotation of dust clusters in the presence of a magnetic field [54], [55], [56], influences properties of low-frequency waves in dusty plasma [57], [58], causes the formation of a void in the center of the discharge in microgravity experiments [59], [40] and defines the diffusion and mobility of dust particles in strongly ionized plasma [60].

The traditional way to calculate the ion drag force on a test particle is based on the pair collision approximation, that is a case of collisionless ions $l_{mfp} \gg r_{int}$, and an isolated dust particle $d \gg r_{int}$, where r_{int} - the characteristic radius of the interaction between an ion and a dust particle, d - the average distance between dust particles. In general, the ion drag force can be expressed as [2]:

$$F_i = m_i n_i \int v f_i(v) \sigma_i^{tr}(v) v dv, \tag{1.45}$$

where $f_i(v)$ is the ion velocity distribution function, $\sigma_i^{tr}(v)$ is the momentum transfer cross section of ion collisions with a dust particle. The momentum transfer cross section depends on the ion velocity through the scattering parameter:

$$\beta = \frac{U_0}{m v_i \lambda_D}, \tag{1.46}$$

where $U_0 = e|\varphi_s| a \exp(a/\lambda_D)$ and λ_D is the effective screening length, which has been defined above in this chapter (1.4). For subthermal flows (ion flow velocity below the thermal ion velocity, $u_i \leq v_{Ti}$) the thermal scattering parameter is used:

$$\beta_T = e^2 |Z| / \lambda_D T_i. \tag{1.47}$$

The ion drag force is also determined by the ion velocity. Two limiting cases exist. In the case of subthermal flows (when the thermal Mach number is small $M_T = u_i / v_{Ti} \ll 1$) and $\beta_T \leq 5$ the next expression for the ion drag force derived in [20]:

$$F_i = \frac{1}{3} \sqrt{\frac{2}{\pi}} \left(\frac{T_i}{e} \right)^2 \Lambda \beta_T^2 M_T, \tag{1.48}$$

where

$$\Lambda(\beta_T) \simeq \int_0^\infty e^{-x} ln(1 + 2x/\beta_T) dx \equiv e^{\frac{\beta_T}{2}} E_i\left(-\frac{\beta_T}{2}\right) \tag{1.49}$$

is the modified Coulomb logarithm integrated over the Maxwellian distribution function. Here the screening length is equal to the ion Debye length. The case of very large β_T is investigated in [61]. The obtained expression is:

$$F_i \simeq \frac{2}{3}\sqrt{\frac{2}{\pi}}\left(\frac{T_i}{e}\right)^2 \ln^2 \beta_T M_T. \tag{1.50}$$

In the case of a large Mach number $M_T \gg 1$ the drift velocity should be used instead of the thermal velocity to estimate the parameter β_T. The screening length is determined by the electron Debye length. In this case the scattering parameter decreases rapidly with the Mach number. The ion drag force can be written as:

$$F_i \simeq \left(\frac{T_i}{e}\right)^2 \ln\left(\frac{\lambda_{De}}{\lambda_{Di}}\frac{M_T^2}{\beta_T}\right)\frac{\beta_T^2}{M_T^2}. \tag{1.51}$$

Finally, in the limiting case of very high relative velocity only the geometrical particle size matters, then [40]:

$$F_i \simeq \left(\frac{T_i}{e}\right)^2 \left(\frac{a}{2\lambda_{Di}}\right)^2 M_T^2. \tag{1.52}$$

Another way to calculate the ion drag force is the kinetic approach based on the so-called "linear dielectric response formalism" [62]. Instead of calculating single ion trajectories and then integrate the resulting momentum transfer, it is possible to solve the Poisson equation with the kinetic equation for ions and obtain the electrostatic potential around a particle. The polarization electric field at the origin of a particle gives the force on a particle. Recently, Ivlev *et al.* [63] have applied this formalism for the calculation of the ion drag force for arbitrary velocity of ion flow and arbitrary frequency of ion-neutral collisions.

The binary collision approach is applicable, when ions are collisionless, i.e. ion mean free path exceeds the screening Debye length and the potential is close to isotropic. The latter is satisfied for subthermal ions. In the case of large Mach numbers the particle potential is anisotropic and the kinetic approach is more suitable.

Electron drag force

Similar to the ion drag force the electron drag force arises due to the momentum transfer from the electrons drifting relative to the charged particles. In the binary collision approximation the electron drag force can be expressed as [40]:

$$F_e = m_p \nu_{pe} u_e, \tag{1.53}$$

where $\nu_{pe} \simeq (2\sqrt{2\pi}/3)(m_e/m_p)n_e v_{Te} a^2 z^2 \Lambda_{de}$ is the momentum exchange rate between dust particles and electrons, v_{Te} is the electron thermal velocity, $z = |Z|e^2/aT_e$ is the absolute magnitude of the dust particle charge, eZ, in units of aT_e/e^2 and Λ_{de} is the Coulomb logarithm for grain-electron collisions [40], [64]. The effect of the electron drag force compared to the ion drag force is usually ignored because of the small electron mass. In [40] it is emphasized that the electron drag force can be ignored, if $u_e \sim u_i$ in RF discharges, where electrons and ions drift together due to ambipolar diffusion. But, for example, in the positive column of a DC discharge, in the case of an independent drift, the ratio of the ion-to-electron drag forces is independent of masses and can be approximately estimated as:

$$\frac{F_i}{F_e} \sim \left(\frac{T_e}{T_i}\right)^2 \frac{\sigma_{en}}{\sigma_{in}}, \tag{1.54}$$

where $\sigma_{e(i)n}$ is the transport cross section for electron (ion) collisions with neutrals. The investigation in [64] shows that the electron drag force can indeed dominate over the ion drag force in most of the noble gases with relative small electron temperature ($T_e \leq 1$ eV).

Neutral drag force

In a weakly ionized plasma neutral gas friction is the main mechanism, also called neutral drag force. In general, this force is proportional to the particle velocity, which is usually much smaller than the thermal velocity of neutrals. The expression for the neutral drag force depends on the value of the Knudsen number:

$$K_n = \frac{\lambda_n}{a}, \tag{1.55}$$

which is the ratio of the molecular or atomic mean free path to the particle radius. If the Knudsen number is large $K_n \gg 1$, the molecular regime is realized. For a small relative velocity of the particle with respect to the gas, $u \ll v_{Tn}$, the neutral drag force can be written as [65]:

$$F_n = -\frac{8\sqrt{2\pi}}{3}\gamma a^2 n_n T_n \frac{u}{v_{Tn}}, \tag{1.56}$$

where n_n and T_n are the concentration and temperature of neutrals, respectively, and γ is a coefficient of the order unity, which depends on the way the neutrals are scattered from the particle surface [65]. The minus sign means that the force acts in the direction opposite to the particle velocity. For high relative velocity $u \gg v_{Tn}$ the neutral drag force is proportional to the velocity squared [40]:

$$F_n = -\pi a^2 n_n m_n u^2. \tag{1.57}$$

In the limit of small Knudsen number $K_n \ll 1$ there is the hydrodynamic regime, in

which the resistance force is given by the Stokes expression [66]:

$$F_n = -6\pi\eta a u, \tag{1.58}$$

where η is the neutral gas viscosity.

1.4 Interaction between particles in complex plasmas

Until now we have considered a single isolated dust particle in plasmas, its behavior and forces acting on it. We have not taken collective effect from many neighboring dust particles into account, which usually form dust cloud in dusty plasmas.

The determination of the interaction between dust particles is a challenge in complex plasma physics. The difficulty is that the potential of the interaction depends on the particle charge, which varies in time. Also collective effects can play a role in the particle interaction, when there is a large dust concentration. For a lower dust concentration the interparticle interaction can be considered within the approximation of an isolated particle. The electrostatic force acting on the particle with the fixed charge Ze from another particle situated at a distance r is presented in the form:

$$F_e = -\frac{dU(r)}{dr}. \tag{1.59}$$

At small distances $r \ll \lambda_D$ the potential of an isolated particle is considered to be purely Coulomb [2]. But if $r \sim \lambda_D$, the screening is important and the Debye-Hückel potential can be used. Finally, if the distances are very large (several Debye lengths) the potential is described by the power-law asymptotic. Thus, for not very large distances the screened Coulomb potential can be applied:

$$U(r) = \frac{Z^2 e^2}{r} exp\left(-\frac{r}{\lambda_D}\right). \tag{1.60}$$

As it has already been shown in several works [40], the interaction potential between two grains surrounded by Debye spheres contains an attractive part at large distances. Some of these attractive forces will be discussed below.

The experiment to determine the particle interaction potential has been done by Konopka *et al.* [67], where the analysis of elastic collisions between two particles has been performed. The collisions were exited by an electric probe inserted into a discharge chamber. From the trajectories and velocities of the particles during collisions the form of the interaction potential can be reconstructed by using the equation of motion. Other experiments also

have been done to determine the interaction between particles. They will be mentioned later in this chapter, when some other interaction forces are considered. In chapter 5 the interaction force between particles in small three dimensional plasma cluster will be estimated.

1.4.1 Electrostatic energy between grains

The changing of the electrostatic energy between two grains displaced from infinity up to the certain distance has been described in the work of Morfill *et al.* [68]. They have considered two grains on the distance $r_{1,2} =\mid r_1 - r_2 \mid$ with the total potential equal to $ZeV(r_1, r_2)/r_{1,2}$. The authors have shown that the charge on each grain decreases at the intergrain distance decreases, the Coulomb interaction energy increases respectively. But at the same time the total change in the electrostatic energy, when grains are displaced from infinity to $r_{1,2}$, will not be $Z^2eV(r_1, r_2)/r_{1,2}$, but it will be -$Z^2eV(r_1, r_2)/r_{1,2}$, as if the dust grains were attracting each other and not repelling like for the equal sign charges.

Usually in laboratory experiments there are more than two dust particles and for such dust clouds the collective effects become important. Many particles create a sink of energy (decrease of electron energy), which should be compensated by external sources. The presence of other particles make the attractive character of the interaction between two test grains possible.

1.4.2 Shadow force

Beside the electrostatic interaction, particles can experience the forces connected with ion and electron flow to their surface. Such a flow leads to a drag force on a neighboring particle resulting in an attractive force between particles. This force is called *the shadow force*. Because of the large ion mass ion drag provides the dominant contribution to this force. For a single dust particle at rest the ion flow to the surface is spherically symmetric and there is no net momentum transfer from ions to a grain. But if there are two grains and the ion motion is collisionless the plasma flux on one of the grains is shadowed by the other grain. Therefore, the pressure outside of the grains is larger than the pressure from inside and some attraction of particles can be observed. This effect was firstly considered by Ignatov [69], Tsytovich *et al.* [70] and Lampe *et al.* [29]. The shadow force can be calculated as a product of the ion momentum flux and the momentum transfer cross section σ for the ion-grain collisions averaged over the ion velocity distribution function [71]:

$$F_{shadow} \approx -2\pi m_i n \int_0^\infty dv\sigma(v)v^4 e^{-v^2/2v_{Ti}^2} \int_0^{\theta_*} d\theta \cos^2\theta \sin\theta, \tag{1.61}$$

where $v_{Ti} = \sqrt{T_i/m_i}$ is the ion thermal velocity, $n = n_i = n_e$ is the unperturbed plasma density and θ_* is the angle defining the cone in ion velocity space, where the ions are moving only towards the grain; at large distances from the grain the angle θ_* can be estimated as $\theta_* \approx (a/r) \times (2Ze^2 a m_i v^2)^{1/2}$ [71].

The attractive shadow force can dominate at large distance, $d \gg \lambda_{Di}$, when the repulsive Coulomb field is screened. Also it is necessary to remember that ion collisions will decrease the shadow effect and the shadow force vanishes at $d \geq l_{mfp}$. The shadow attraction is proportional to the grain size and it rapidly increases with the dust size increasing.

Also attraction or repulsion can be caused by neutrals, if they leave the particle surface with a temperature different from the surrounding gas temperature. This can occur if the particle surface temperature is different from the gas temperature. In this case a momentum and energy flux between gas and particle exists, which creates the shadowing force between neighboring particles [72].

In the free molecular (kinetic) regime an expression for the interaction potential between grains due to the neutral shadow effect has been derived in [72]:

$$U_n = \frac{3\pi}{8} \left(\frac{a^4 p}{r} \right) \frac{\triangle T}{T_n}, \tag{1.62}$$

where p is the neutral gas pressure, r is the distance between grains, $\triangle T = T_s/T_n \ll T_n$ with T_s is the dust surface temperature and T_n the neutral gas temperature. The interaction is repulsive for $\triangle T > 0$ and is attractive for $\triangle T < 0$. In ref. [73] the comparison of the magnitude of the neutral shadowing interaction with the ion shadowing interaction and the pure Coulomb repulsion between charged dust particles has been performed. It results that under typical conditions ($a/\lambda_{Di} \sim 0.1$, $T_e/T_i \sim 100$, $n_i/n_n \sim 10^5 \div 10^6$ and $\triangle T/T_n \sim 0.2$) the neutral shadowing is weaker or comparable to the ion shadowing and considerably weaker than the pure (unscreened) Coulomb interaction.

Thus, the shadow force due to neutrals is repulsive, if the temperature of the dust surface is higher than the temperature of neutral gas. In usual laboratory plasmas the difference between these two temperatures is two small to make neutral shadow force significant for the dust behavior. But under certain conditions dust can be cooled quickly, then the effect of attraction should be observed. This situation can take a place under astrophysical conditions, where radiative cooling is very efficient.

1.4.3 Wake potential

If there is a directed flow of ions in a plasma, the neutralizing Debye sphere around a particle becomes asymmetric. This leads to additional forces on neighboring particles. Such

a situation is usually realized in ground based experiments, when dust particles levitate in the plasma sheath above the lower electrode. Streaming ions are focused downstream from the grain and create a *wake*, "positive space charge", which can affect (attract) a lower particle. This effect is usually used to explain the formation of so-called "particle chains" often observed in experiments. In the work of Lampe *et al.* [29] it is shown that under typical discharge conditions with $T_e/T_i \approx 25$ there is a decay of the wake potential behind the grain. The wake is strongest for flow speeds near $M = 1$.

Upstream from the particle [29] the potential distribution is close to the Debye form. Usually because $T_i < T_e$ the ion screening dominates in the bulk plasma. But for high ion velocities (big Mach numbers $M \gg 1$) the ion screening becomes ineffective and $\lambda_D \sim \lambda_{De}$.

It is necessary to note that creation of a "wake" is very sensitive to the ion-neutral collisions, which destroy directed ion velocities and, therefore, affect the wake structure.

A method based on laser manipulation of the dust particles was proposed by Melzer *et al.* [74] in order to study the effect of wake formation on the particle interaction. The experiment involved two particles, one of them was heavier and levitated below the other. Then a laser beam was used to push either the upper or the lower particle. The lower particle followed the upper one, when it was pushed by the laser. But the upper particle never followed to the lower one. This proves that the effect of particle attraction due to ion wake is asymmetric (the force acts only on the downstream particle).

1.4.4 Dipole-dipole interaction

The formation of an ion wake downstream of the suspended grain modifies the dust-dust interaction potential introducing an anisotropy in particle interactions. In particular, according to recent laboratory studies of "particle pairing" in the plasma sheath, the ion wake can cause an attractive force between grains [75, 76]. The positive charge concentrates below the negative particles and forms a kind of dipole, which can influence the next negative grain and vice versa. The standard approach to the dipole-dipole interaction is to model the ion wake with a positive point-like effective charge q located at some small distance l downstream, within the Debye sphere [77]. The combined system "particle charge and its ion density enhancement" – in a further simplification – is treated as an uncompensated residual particle charge Q, plus an electric dipole $P = ql$, which accounts for the anisotropy of the plasma due to the ion flow.

The electrostatic potential around an electric dipole is [78]:

$$\phi = \frac{1}{4\pi\varepsilon_0 r^2}(P \cdot \overrightarrow{r}), \tag{1.63}$$

where $\overrightarrow{r}$ is a unit vector between two charges, P is a dipole moment. The electric field

Figure 1.6: Scheme of the binary particle interactions. The vertical coordinate y is directed to the lower electrode (along the ion flow) [79].

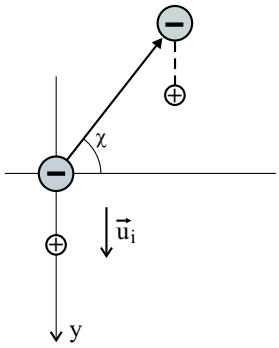

can be found as a gradient of this potential [78]:

$$E = \frac{1}{4\pi\varepsilon_0 r^3}(3(P \cdot \overrightarrow{r})\overrightarrow{r} - P). \tag{1.64}$$

Then, the dipole force is $F = (P \cdot \nabla)E$.

This mechanism has been used in the paper of V. Yaroshenko *et al.* [79] to explain dust-dust interaction in the cluster of small size (4 particles), where the attraction between the particles has been observed. The usual assumption of the pure symmetric Coulomb screened dust-dust interaction is not enough to describe the behavior of the particles situated in the plasma and not in the plasma sheath. The force describing binary dust-dust interactions can be represented as a combination of the electrostatic force due to the repulsion of the residual-like particle charges and a dipole force due to the streaming ions [79]:

$$F = \frac{Q^2}{\lambda_D^2}\left[\frac{(1+\kappa)\exp(-\kappa)}{\kappa^2} + 3\varsigma\frac{\left(1-3\sin^2\chi\right)}{\kappa^4}\right], \tag{1.65}$$

where F denotes the force component along the radius-vector between two particles (see Fig. 1.6), $\kappa = \Delta/\lambda_D$ is the so called lattice parameter, Δ is the interparticle distance, and the dimensionless coefficient $\varsigma = q^2 l^2/\left(Q\lambda_D\right)^2$ specifies the value of the electric dipole moment. The quantity χ denotes the angle between the direction perpendicular to the ion flow and the radius-vector connecting the two particles (Fig. 1.6).

1.4.5 Strongly coupled dusty plasmas and crystal formation

The finite number of particles in plasmas confined externally form *dust crystal* or *plasma crystal*. The main character of interaction between particles is considered as pairwise repulsive Debye-Hückel (Yukawa) potential, therefore, such systems sometimes are called

Coulomb or Yukawa crystals. But the question of particle interaction in plasma crystals is still open. For a system consisting of a medium number of particles ($10^2 \div 10^3$) the term *cluster* is used, the larger systems are called crystals. The first dusty plasma crystals were discovered in a capacitively coupled low pressure RF discharge in inert gas almost simultaneously in several laboratories [14], [13], [15], [16]. Schematically the apparatus to investigate the particle behavior consists of two parallel plate electrodes, placed in a vacuum chamber, one of them is RF driven. The inserted particles get negatively charged and levitate above the lower electrode obeying basically the electric and gravitational forces. To compensate gravity the electric field should be strong enough, which is satisfied in the plasma sheath, where particles are usually situated in ground based experiments. In such conditions two-dimensional plasma crystals are mostly observed. In the reference [2] authors report the 2 and the 1/2 dimensional character of plasma crystals, and three dimensional structures are very difficult to get under gravity conditions.

From this point of view the experiments in the absence of gravity (microgravity experiments), where the relatively stress-free 3D plasma structures can be obtained, are valuable. Within the frames of the Russian-German cooperation the experiment "Plasma Crystal" is successfully performed on-board the International Space Station (ISS). In [19] the authors describe the results obtained from the ISS experiments. In the most ordered area of the crystal formation several types of lattice structures were observed: fcc, bcc and hcp. The formation of the shell structure has been obtained by simulations in several works [80], [81] and in the analysis of dust crystals reported in [82]. It has been shown that the inner particle shell forms almost uniform hexagonal structure, while near the boundaries they form circular shells.

Under microgravity conditions the dust cloud structure besides the shells has usually a void just in the middle of the discharge. A typical picture from microgravity experiments with a void is shown on Fig. 1.7. Explanation of the void formation is an important topic in complex plasma science. It is usual to assume that the electric field is directed radially to the walls of the chamber, hence, it pushes particles to the center of the discharge. Therefore, there is some force, which acts on the particles from the center of the discharge to the boundaries. In works [83], [84] and [20] it has been suggested that the ion drag force can be more significant in the absence of gravity and it is responsible for the void formation. The authors found that in the collisionless regime, when $l_{mfp(i)} \gg \lambda_D$, the condition $F_i/F_e > 1$ can be satisfied. This means that the ion drag force could cause the void inside the dust cloud.

The structural properties of a dust component, of course, depend on the parameters of the surrounding plasma. By changing them the different behavior of particles can be obtained. The so-called *phase transitions* have been observed, when the static crystal-like

Figure 1.7: The dust plasma structure with void under microgravity conditions.

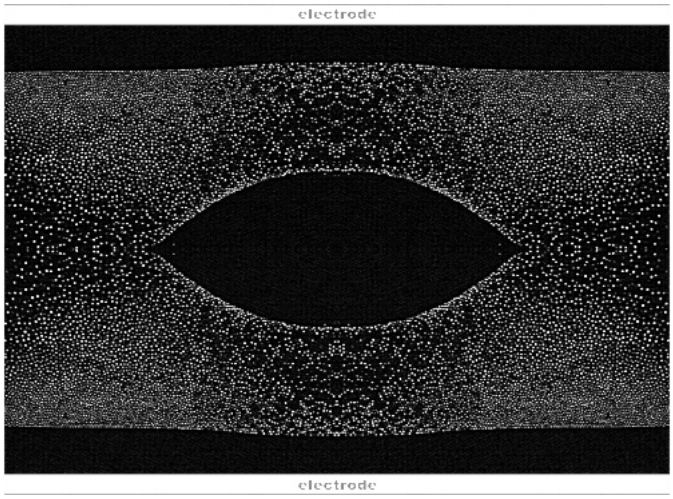

order changes to liquid-like. Such transition is called melting and it has been observed in several works ([85], [86], [87], [88]). The melting of a crystalline structure can be initiated either by a decrease of the neutral gas pressure or by an increase in the discharge power. For example, the initial temperature of grains increased from room temperature ($\sim$ 0.03 eV) in crystal up to 5 eV in liquid state with decrease of the pressure, [86].

The fundamental characteristic of many particle systems is *the coupling parameter*, which is the ratio of the potential energy of interaction between neighboring particles to their kinetic energy. For the Coulomb interaction it is [2]:

$$\Gamma = \frac{Z^2 e^2}{T\Delta}, \tag{1.66}$$

where $\Delta = n^{-1/3}$ characterizes the average interparticle distance and T is the particle kinetic energy. The system is considered as strongly coupled when $\Gamma \geq 1$. In a complex plasma the charge of the particle is very high ($\sim 10^4 e$) and at the densities $\sim 10^{11}\ m^{-3}$ the coupling parameter Γ is of the order of 10^5. Therefore, (sufficiently cold) complex plasmas can be considered as strongly coupled systems. In our experiments with 3D clusters (chapter 6) we got a coupling parameter of the order of 400. This is close to the transition between solid and liquid states.

In order to understand in which state the system exists, crystallization (melting) criteria are used. Best known in dusty plasmas is the Lindemann criterion [89], according to which melting of the crystalline structure occurs, when the ratio of the root-mean-square particle displacement to the mean interparticle distance reaches a value of $\sim$ 0.15. There is another

criterion related to the maximum of the structure factor in the liquid state, which reaches a value of the order of ~ 2.85 at crystallization [90]. Another criterion for crystallization was proposed by Löwen *et al.* [91], where crystallization occurs, when the diffusion constant reduces to a value of ~ 0.1 compared to the diffusion constant for the non-interacting particles.

For the quantitative analysis of the ordered structure of particles the pair correlation function $g(r)$ is used. It represents the probability of finding two particles separated by a distance r and measures the transitional order in the structure of interacting particles [92]. For the case of a crystal at zero temperature, $g(r)$ is a series of δ functions, whose positions and heights can be determined from the particle separation in a perfect hexagonal lattice. Experimentally $g(r)$ can be calculated by measuring the distances between particles in some concentric ring choosing one particle as a central one. This number can be normalized by the ring's area. Making such analysis the shell structure of the plasma crystals can be obtained.

Chapter 2

Experimental set-up and methods of measurements

The experiments presented in the thesis have been performed in two different set-ups. Both of them include a chamber with two parallel plate electrodes, where a capacitively-coupled radio-frequency discharge is initiated. The first chamber has metallic walls and the second chamber, so-called PKE-Nefedov chamber [19] glass walls. The main feature of these two chambers is that both of them contain as a lower electrode the so-called "adaptive electrode". This is a segmented electrode with possibility to apply RF or/and DC voltage to each segment (pixel). The dust particles are injected inside the chamber and levitate usually in the plasma sheath, where the electric field is strong enough to compensate gravity. This happens on floating or grounded lower electrodes. As soon as DC or RF voltage is applied to one of the pixels of the "adaptive electrode", a small glow ("plasma ball" or "secondary plasma") appears in the sheath. Levitated particles start to be collected in this region sometimes forming crystal structures. Typical crystals have been obtained in the PKE-Nefedov chamber, their study will be discussed later (see chapters 3, 5, 6). The "adaptive electrode" and the formation of the "plasma ball" will be described in detail in section 2.3 of the current chapter and in chapter 4.

The "adaptive electrode" is also used in a metallic chamber. Some experiments with particle manipulations will be described using the driven pixel of the "adaptive electrode" (see chapter 3). The experiments with dust particles in an electronegative discharge (Oxygen gas) have also been performed in the chamber with metallic walls (see chapter 7). But in these experiments the "adaptive electrode" stayed grounded. The behavior of dust particles in Oxygen gas has been analyzed in order to study the electronegative plasma sheath.

The current chapter describes main parts of two set-up configurations, principle of particle injection, visualization, plasma diagnostics, etc.

Figure 2.1: The sketch of the set-up with metallic wall chamber.

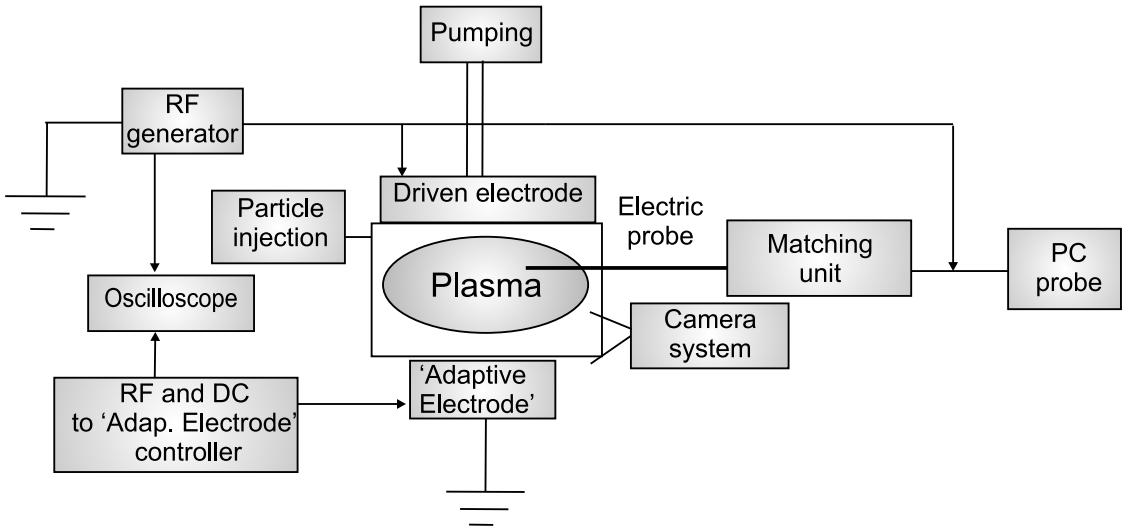

2.1 The metallic chamber with glass windows

The sketch of the first set-up configuration is presented in Fig. 2.1. Here the chamber has 8 round ports, some of them giving the possibility to observe the plasma glow. The chamber consists of two parallel plane electrodes, which have diameters of 30 mm, and are 30 mm apart. The upper one is RF driven. The lower electrode, as already has been mentioned above, is "adaptive". During experiments performed in this chamber and considered in the thesis, it has been grounded. The plasma is generated by radio frequency excitation at 13.56 MHz and 300 V (peak-to-peak) amplitude. The power to the driven upper electrode is measured by an oscilloscope. The Langmuir probe, which is used for measuring of plasma parameters, is inserted into the discharge through one of the chamber ports. The voltage applied to the probe is also monitored by an oscilloscope through a high impedance probe. The analysis of the current gathered by the probe is carried out numerically by a data acquisition system. The picture of the experimental set-up is presented in Fig. 2.2.

2.1.1 Vacuum system

Before the experiments the chamber has been evacuated by a turbo pump. The reactor may be isolated by a valve, which can be manually or automatically actuated controlling the pumping speed. The working gas (Oxygen or Argon) has been supplied through a gas inlet placed in one of the chamber ports. The gas flow is controlled by a mass-flow controller. In all the experiments the flow was 0.8 sccm or a bit lower. The purity of the

Figure 2.2: Picture of the experimental chamber with metallic walls.

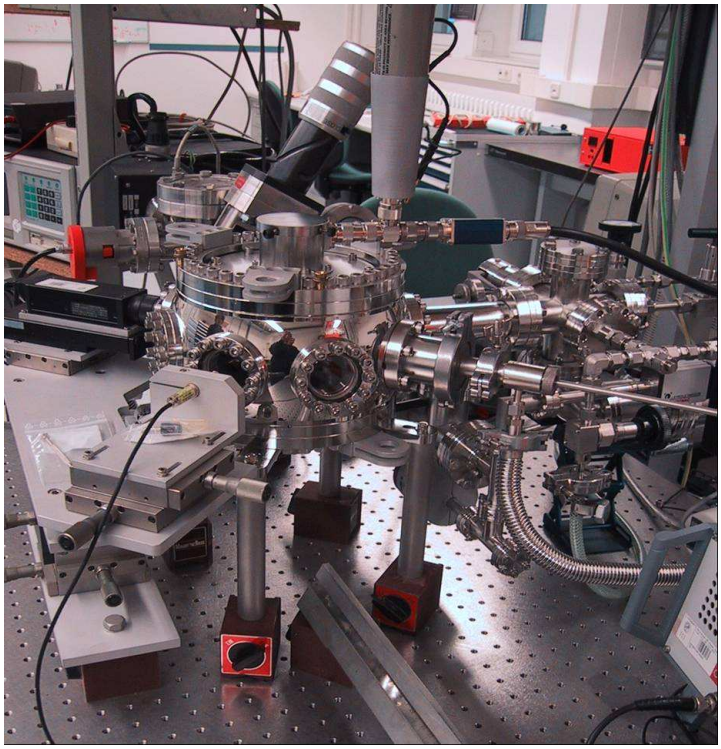

gas is very essential in our experiments. In order to provide high experimental accuracy and investigate the electronegative plasma sheath we have kept a continuous gas flow. The range of pressures, in which the experiments have been performed, is from approximately 4 to 100 Pa (0.03 $Torr$ to 1 $Torr$). Further in this thesis the pressure will be given in Pa.

It must be noted that the electrode configuration described above is rather asymmetrical, because the walls of the metallic chamber serve also as extended grounded electrode. This makes the effective size of the driven electrode much smaller than the grounded surface. As a consequence most of the DC and RF voltage difference will develop in the sheath adjacent to the driven electrode.

2.1.2 Particle injection

Particles of micrometer size have been injected inside the chamber. A typical number of injected particles during experiments is about 30-50. For our purpose to use microparticle as a diagnostic tool for the electronegative plasma sheath we need the plasma to be unperturbed by the presence of particles. In this case we are able to use the single particle approximation for our calculations.

These microparticles or dust particles were spherically shaped melamine formaldehyde

Figure 2.3: Levitation of particles in the electronegative plasma sheath. On the left hand side there is the dispenser, on the right hand side the electric probe is seen. They both are quite far away behind the particles. Picture size is 16 × 12 mm.

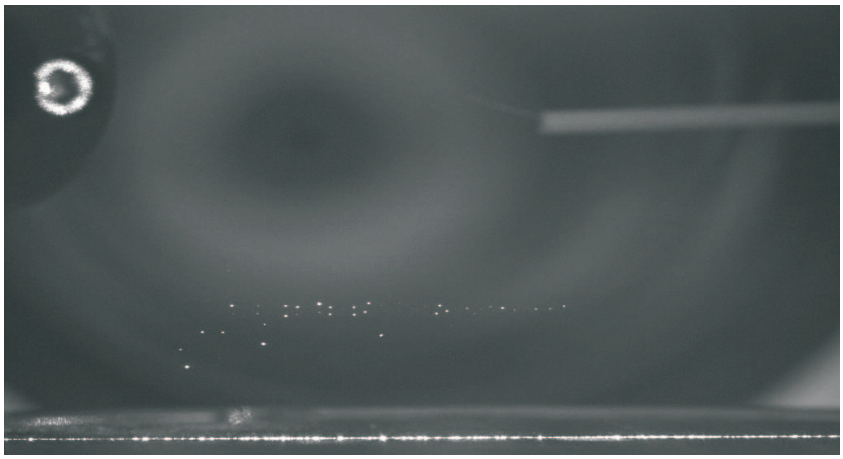

particles (a dielectric polymer) with density of substance $\rho = 1514\ kg/m^3$, manufactured by MicroParticles GmbH of Berlin, Germany. We have used particles of three different sizes: 1.29, 3.42 and 6.81 μm in diameter. The spheres were supposedly monodispersed, having a quoted radial variation of less than 0.1%.

The particles are injected inside the chamber by a dispenser, which is a small container, mounted on a metallic arm and placed in the discharge. The container has a grid, through the fine holes of which the dust particles fall out when the dispenser is shaken. The size of the grid holes has to be several times larger than the diameter of the particles.

The injected particles levitate in the sheath region as seen in Fig. 2.3, gravity being compensated mainly by the upward electrostatic force. With time particles may change their mass and shape because of etching and, consequently, change their position in the sheath. To avoid the inaccuracy, we have taken the data immediately after the injection and then replaced the particles at every experiment.

2.1.3 Illumination of particles

The position/motion of particles in the plasma sheath has been visualized by illuminating them with a laser, fanned out in a vertical plane. This is a diode laser with wavelength 681 nm. The width of the laser sheet is 0.072 mm, the height of illumination is 39.7 mm in the center of the chamber.

The laser is situated in front of one of the glass windows. At 90^0 to the laser, in front of another glass window, there is a CCD (charge coupled device) video camera. The camera

records the particles' position in two directions. The acquisition speed of the CCD is 25 frames/sec. The images from the experiments are monitored on the computer screen and digitized via a frame grabber. The data can be saved either as pictures or as movies with variable speed, amplification and shutter time.

2.2 The PKE-Nefedov chamber

The second chamber, where experiments have been performed, is called PKE-Nefedov chamber. It is the chamber of basic plasma experiment in the International Space Station (ISS), which has been installed in February 2001 by the first permanent crew. It is designed for long-term investigations of complex plasmas under microgravity conditions. In the absence of gravity the microparticles move into the bulk of the plasma [59], experiencing much weaker volume forces than on Earth. This allows investigations of the different properties of strongly coupled plasma states under substantially stress-free conditions.

2.2.1 Arrangement of the PKE-Nefedov chamber

The PKE-Nefedov chamber is shown in Fig. 2.4. The side walls of this reactor are made of glass, almost a third of the total plasma confining area. The upper electrode is radiofrequency (RF) driven at 13.56 MHz, the lower electrode being floating, apart from a small central "pixel", 3.8×3.8 mm^2, which can be independently driven in DC and RF voltage. Typical conditions in our experiments have been the following: RF voltage on the upper electrode in the range $200-300V_{pp}$, about $150V_{pp}$ in "push-pull" on the lower central pixel, Argon pressure from 35 to 70 Pa and melamine-formaldehyde particles of 3.4 μm diameter injected with an automatical dispenser placed in the upper electrode. By suitably adjusting DC and RF on the central pixel, a glow region is formed above the electrode ("secondary plasma"), that can be much brighter than the bulk plasma depending on the voltage amplitude. Here different levitation positions for the particles, including three-dimensional plasma clusters (see chapter 3), can be obtained. The particle number in the cluster can be controlled by varying the RF applied to the pixel. Since all the microparticles carry negative charges, one would presume that the internal electrostatic pressure would disperse a cluster without a strong additional confinement. This confinement can, in principle, be due to electrostatic fields, ion or neutral drag/pressure. In addition, there could be attractive force between the charged particles, as will be discussed later (see chapter 5).

As in the previous case also this chamber is pumped with a turbo-pump automatically controlled and the gas flow is measured by a mass-flow controller. In this chamber we have used only Argon. The voltage on the RF driven electrode and on the driven pixel of the "adaptive electrode" is measured by an oscilloscope.

Figure 2.4: The PKE plasma chamber.

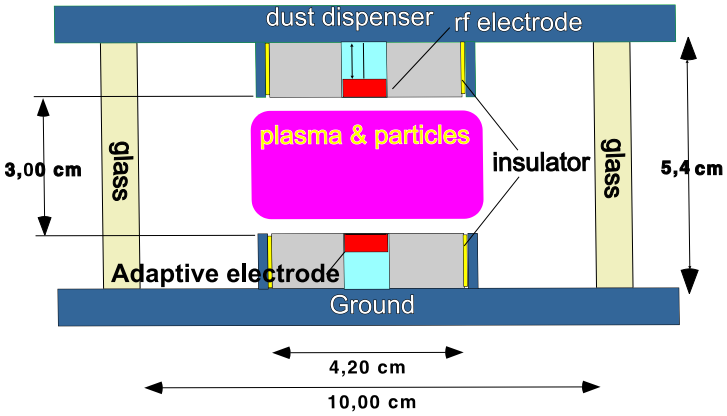

2.2.2 Three-dimensional diagnostics

After plasma clusters are created they need to be visualized. For this purpose we use illumination lasers and recording cameras – a typical system, often used in dusty plasma experiments. But in the PKE set-up, in contrast to the metallic chamber, the configuration of lasers and cameras is special in order to record 3D variables. After particle visualization by lasers and cameras, we need the analysis of the structures obtained. In some cases, where only the xy plane of particle assemblies is investigated, the third coordinate is not so important and 2D pictures are used ([74], [67]). But clearly, with the possibility to conduct kinematic measurements one wishes to determine the full 3D distribution function $f(x,v,t)$. This cannot be done without knowledge about the particle distribution in third direction. For this purpose the scanning by an additional laser beam in the z direction is commonly used ([27], [93], [94]). The scanning is based on shifting laser and camera in depth with some velocity (for example, 0.3 mm/sec [93]). In this case there is an unavoidable delay in the measurement of the third coordinate.

The diagnostic set-up, which we have used, allowed us to get all particle coordinates simultaneously as a function of time. This optical system has been developed by Dr. Dirk David Goldbeck and described in details in his Ph.D. thesis [95]. In this thesis we give the main features of this set-up.

The particle distribution is illuminated by two parallel laser beams (686 and 656 nm) of complementary intensity and the scattered light is recorded at an optimal angle of 112° by two selective CCD-cameras (see Fig. 2.5) . The particle image corresponds to instantaneous

Figure 2.5: The 3D visualization scheme implemented in the PKE chamber. The picture is taken from [95].

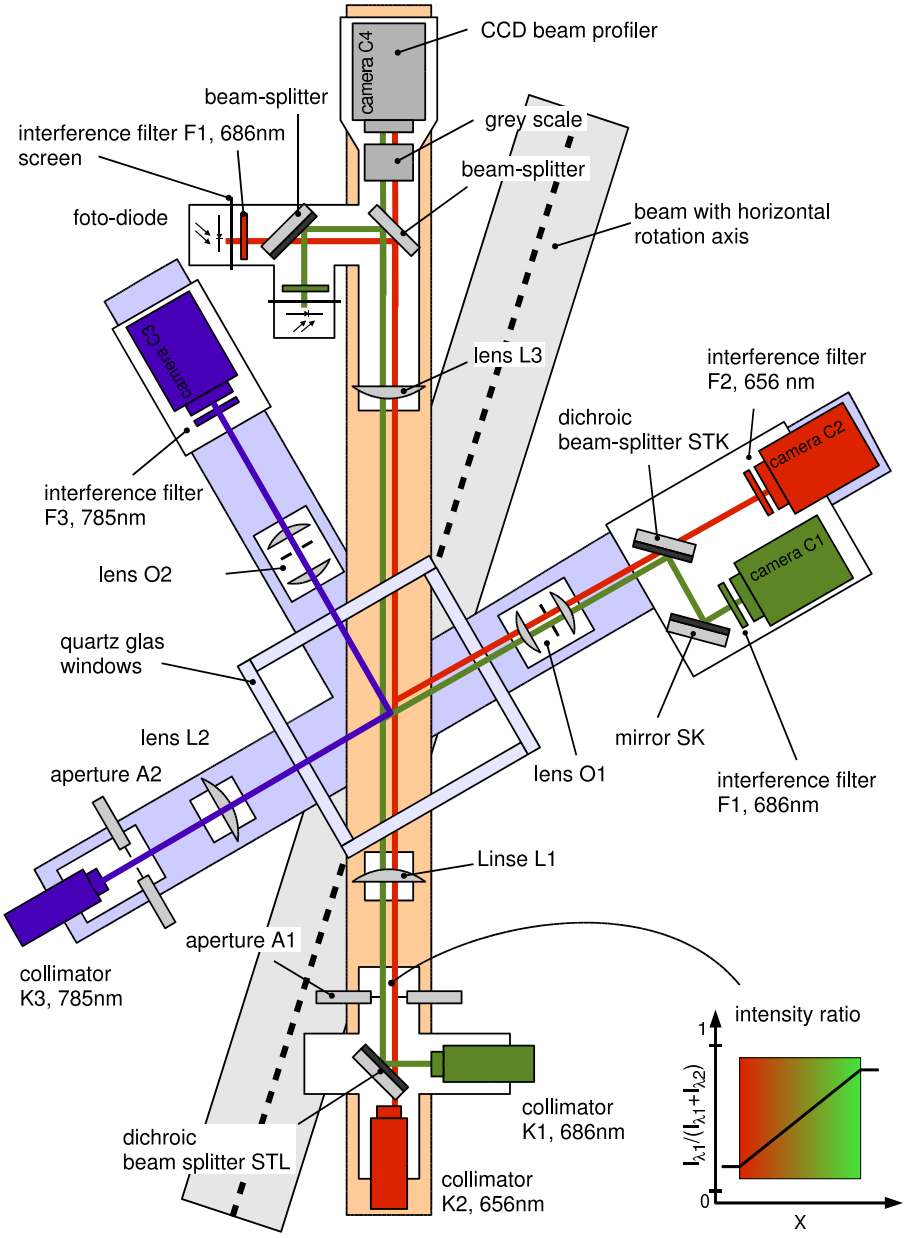

Figure 2.6: The principe of 3D measurements. The distribution of particles in volume is illuminated by the beam with perpendicular gradient of color. The x and y coordinates of particles are obtained from the xy projection, the z coordinate is determined from the ratio of color distribution. The picture is taken from [95].

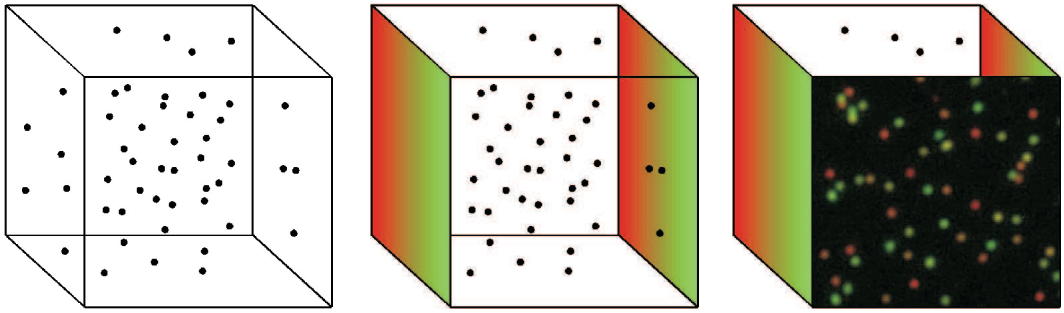

particle position in xy direction, the z coordinate being given by the ratio of the two lasers' scattered light intensity. This is the so-called Red-Green system (RG system) as it is shown in Fig. 2.5. The color of the particle image on the CCD cameras changes from green to red depending whether the particle is situated in the front or in the back (smaller or larger z coordinate) (Fig. 2.6). The velocity vector was determined mainly by the 3D traces left by the particles during the CCD opening time. A typical value is t=36 ms. To improve the resolution in the z direction, positions and velocities are determined also by an additional illumination from an infrared laser (785 nm), with light collected by a third camera at 90^0 with respect to other two cameras. We color code this system as "Blue" (Fig. 2.5). The particle images obtained from this system show z and y position and they are shown in blue. Thus, the 3D particle coordinates can be determined from geometrical coordinates of the images and their colors.

The three cameras provide synchronized time sequences (25 frames/s, total viewing time 8 seconds) for pictures of 2.3 × 1.7 × 2.3 mm size with resolution of 768*576*768 pixels, respectively. This system can be rotated and shifted with respect to the experimental chamber to cover a greater volume. From the digital image sequences all particle coordinates are derived. In the programming analysis each particle image is fitted by a Gauss function, which gives the coordinates and intensities for all sequences. Then xy (Red-Green image) and zy (Blue image) images are correlated in y in order to get x, y and z for each particle (see ref. [95]). Static particles have an error in the position measurement of 3 μm in the x and the z directions and of 21 μm in the y direction. The simultaneity is absolutely indispensable to determine the dynamical behavior of the 3D structures, since it is possible to extract information about the system by observing "fast" events, e.g. interaction between particles (chapter 5) or oscillations of particles (chapter 6).

Figure 2.7: The "adaptive electrode" configuration seen from top.

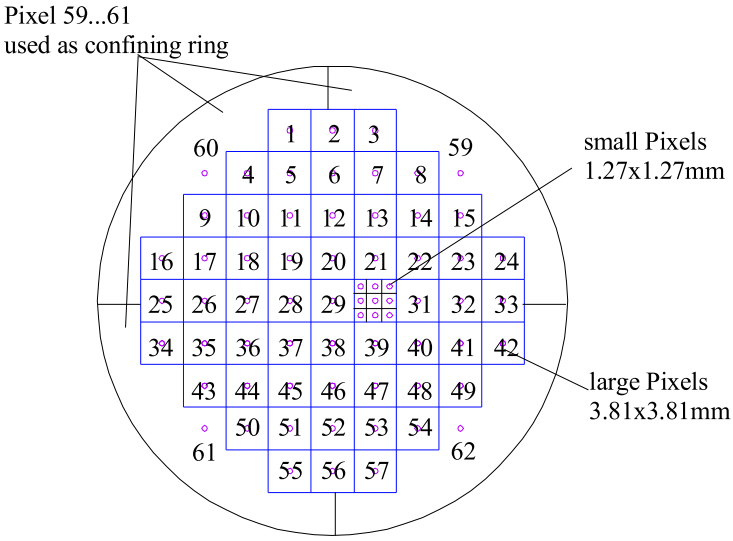

2.3 "Adaptive electrode"

The "adaptive electrode" is an electrode divided in small segments (pixels), independently driveable in DC and RF voltage. The "adaptive electrode" is built by the company "Kayser-Threde GmbH", Munich, Germany following a joint design of Max-Planck-Institut für extraterrestrische Physik and the company "Kayser-Threde GmbH". Several types of adaptive electrode configurations have been developed, in this thesis we will consider only the one, which has been used in the experiments described. The "adaptive electrode" consists of 57 square pixels and 4 external pixels in the shape of a surrounding ring. The square pixels have a size of 3.8 x 3.8 mm^2, one of them has been divided in 9 sub-segments and can be used, when a smaller biased area is needed. This model of "adaptive electrode" has been adapted for both chambers considered here. The full arrangement of the pixels is shown in Fig. 2.7.

The base material of the electrode is Macor Ceramic with a thickness of 7.5 mm. The surface is covered by copper layer of 1 μm thickness. Feed through electrical connections are made using molybdenum wire of 0.25 mm diameter. The gap between pixels is 100 μm. The electrode is mounted in the chamber as it is shown in Fig. 2.1. The controller has 18 DC channels with ± 100 V and 3 RF channels with ± 300 V and 13.56 MHz frequency. That means the possibility to apply independent DC voltage to 18 pixels and RF voltage to 3 pixels simultaneously. In Fig. 2.8 a rough sketch of the "adaptive electrode" section is shown. The wires connect the electrode plate with the breakout board, where DC and RF voltages are applied by DC- and RF-amplifier units. This amplifier is connected to an

Figure 2.8: The sketch of the "adaptive electrode" mounting.

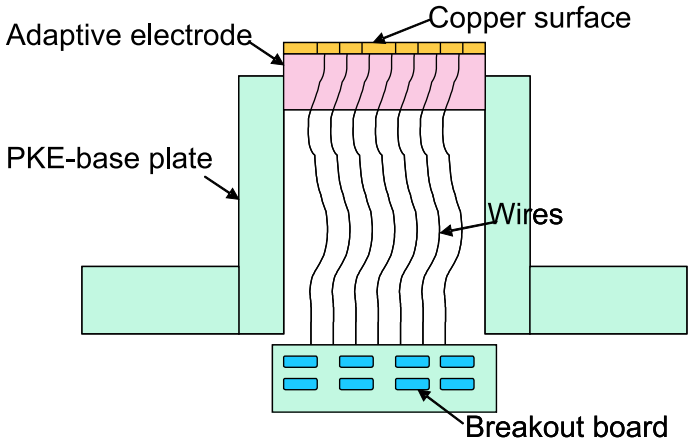

RF probe, which measures DC potential and RF voltage on the pixel. The system is fully computer controlled. LabView programme allows us to select any of 18 DC channels and apply voltage. For the 3 RF channels there is also the adjustment of amplitudes and 360° phase converting.

When RF or DC voltage is applied to one of the pixels and the other pixels are grounded, a bright glow appears. This is a "secondary plasma" in the sheath of the main bulk plasma or, as we call it, the "plasma ball". This "plasma ball" is shown in Fig. 2.9. A possible explanation of the origin of this plasma is the capture of electrons in this region with following high ionization and plasma creation. The brightness of the glow depends on the voltage amplitude and gas pressure. The larger the amplitude applied, the more electrons are trapped. However, the number of electrons inside the plasma sheath is limited. At higher pressures, when sheath shrinks, the pixel can catch more electrons from the main plasma volume and, hence, create a brighter and larger "secondary plasma" glow.

Thus, the "adaptive electrode" introduces modifications inside the plasma sheath. When there are dust particles in the sheath, it influences their behavior as well. Any alteration of the electron and ion fluxes on the electrode's surface modifies also the fluxes to particles. So, the suspended particles are a very sensitive instrument to monitor the sheath structure. As it has been mentioned in the Introduction, in plasma processing very often dust particles etched from surfaces are unwanted, because they can easily influence the processed surface as well as change the discharge characteristics (for example, in etching, thin film deposition, plasma monitor production etc.). Therefore, the possibility of particle manipulation by the "adaptive electrode" is important for technological application. By a careful matching of the amplitude and phase of radiofrequency with respect to the RF on the main driven electrode, it is possible to collect particles (see Fig. 2.10, right

Figure 2.9: The plasma spacing between two electrodes with "secondary plasma" glow on the lower electrode.

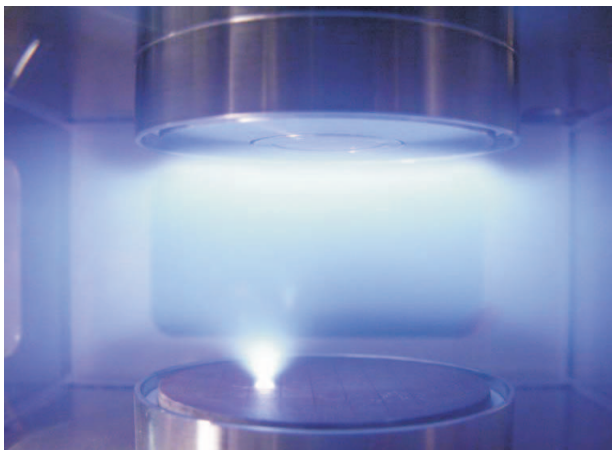

picture), store, repel or re-inject the particles in a versatile way (Fig. 2.10, left picture). Such particle manipulations are possible due to different configurations of the driven pixel circuit. These circuits are shown in Fig. 2.11. The repulsion is achieved leaving the DC bias to develop, i.e., when DC current can not circulate through the pixel (this is represented by the switch open, as it is seen in Fig. 2.11, left circuit). The attraction of particles is obtained connecting the pixel, by means of an inductance, to ground, or to the wall potential, or to a DC source (Fig. 2.11, right circuit).

By increasing the amplitude of the RF voltage volt by volt we can gather dust particles one by one in crystals, thereby controlling the number of grains in these structures.

More details about the particle manipulation with "adaptive electrode" and physical explanation of the plasma sheath modification locally introduced by driven pixel are given in ref. [96].

2.4 Langmuir probe diagnostics

Langmuir probe measurements have been performed to characterize the plasma in the metallic chamber. Since in this chamber we have carried out the experiments in Oxygen, almost all current-voltage characteristics are made in Oxygen.

In our experiments a cylindrical Langmuir probe has been used (Tungsten wire with radius of 87.5 μm and 3 mm length). It is inserted from a lateral port and, being slightly off-axis, could be rotated to scan the space between the electrodes. Before each measurement the probe has been cleaned for about 20 minutes by applying a negative voltage, -60 V, to cause strong ion bombardment. The probe has been actively compensated with RF applied

Figure 2.10: Manipulations of dust particle cloud using "adaptive electrode". Left picture (dimensions $21.5 \times 9.88\ mm^2$) shows repulsion from electrode, right picture (dimensions $16 \times 12\ mm^2$) shows the particle collection and forming of the plasma cluster.

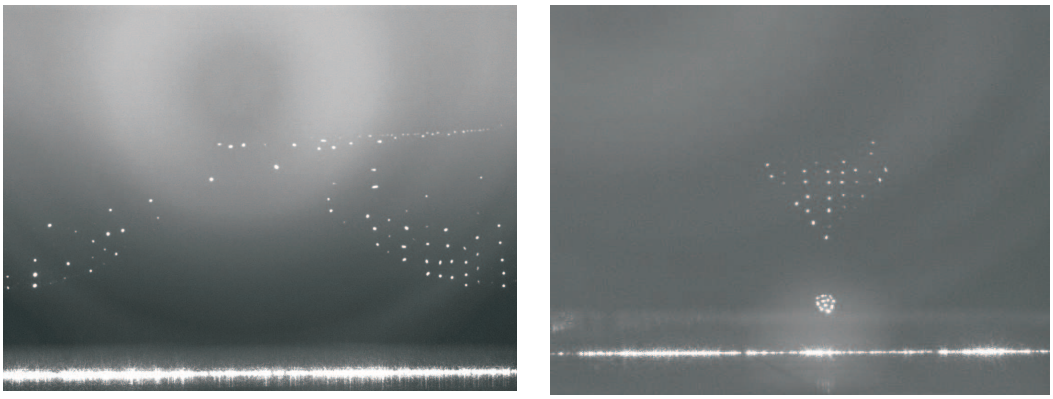

Figure 2.11: The possible configurations of the pixel connections. The switch open gives particles repulsion (left picture), while the switch closed gives particles attraction (right picture). In this case particles can be re-injected in plasma. 1-is the grounded surface of the chamber, 2-connected pixel, 3-RF voltage to pixel, 4-capacity, 5-inductance and 6-switch (left).

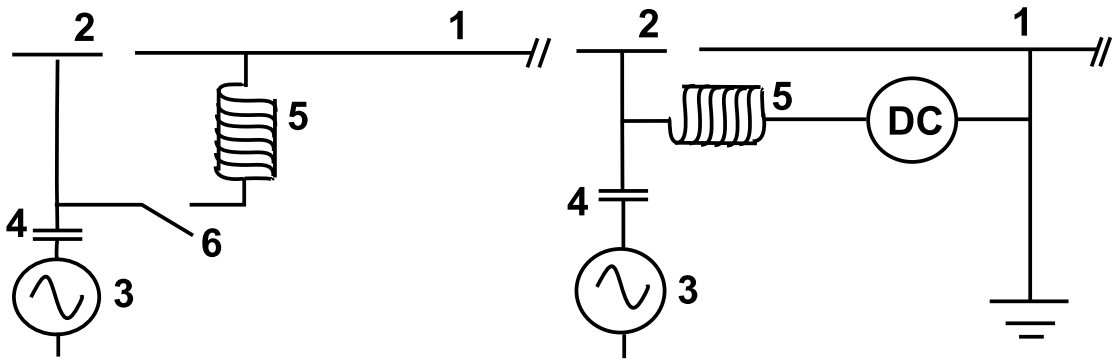

Figure 2.12: The current-voltage characteristics at the static and flowing Oxygen, P=15 Pa.

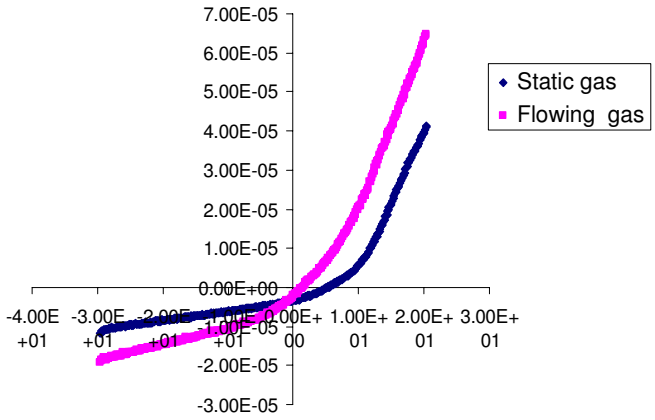

to the probe tip using a three harmonic box [97]. The three harmonic box samples the RF waveform at the driven electrode and generates signals at the fundamental, second and third harmonics. The amplitude and phase of each harmonics are adjusted until the probe current-voltage characteristic is shifted at most to positive voltages. When this occurs the RF applied to the probe tip follows the plasma fluctuations, so that the RF voltage drop across the sheath, which is typical for the asymmetric RF system, is effectively removed. During the measurements it has been found that only the first and second harmonics are needed to fully compensate the probe.

Once compensation is achieved the full IV-characteristic is taken using the digital data acquisition system PSV2 [98]. The system has been used to average the taken current over a number of ramps (we used 1000 ramps to reduce the noises).

We have found out that the IV-characteristics were strongly dependent on the purity of the gas and showed a degradation with time. To reduce contaminants pure Oxygen was constantly introduced in the chamber and the flow rate was increased until the Langmuir probe characteristics were found time independent.

The data acquisition system displays the total probe current (ion and electron), the second derivative of the probe current d^2I/d^2V and $\ln(I_e)$ versus V_a, the applied voltage. The ion current is deduced from a linear interpolation of the total current in the ion saturation region. This ion current is subtracted from the total probe current to give the electron current I_e. The software determines the plasma potential V_p from the zero crossing of second derivative. The plasma temperature is obtained from the gradient of $\ln(I_e)$ versus V_a well below V_p, where any contribution of negative ions is negligible, since $V_a - V_p \ll -k_B T_-/e$. The plasma density n_0 is determined from the current at plasma

potential (knee) assuming that a thermal flux of electrons hits the probe, accounting for the small contributions from the negative ion current.

We have measured many current-voltage characteristics of the discharge during the experiments. Some of them will be given in chapter 7. One example is the dependence of the current to the probe on the gas purity, which is very important in the experiments with Oxygen. Fig. 2.12 shows that we have more negative ions in the discharge, when we use flow of Oxygen, than in the static case (with gas flow the electron current is smaller and total ion current is larger, than without gas flow).

The Langmuir probe measurements in electronegative discharges have their own specifics. When the plasma contains negative ions, a decrease of the saturation current at the positive bias is observed. The region of electron retarding current is distorted and it becomes inaccurate to determine the electron temperature in the usual way. The second derivative of probe current is modified as well. A second peak appears, which is caused by the presence of negative ions. This we will discuss in chapter 7.

Chapter 3

Complex plasma manipulation by radio-frequency biasing

In this chapter an experimental study of the nature, the dimensions and the time scale of the perturbation introduced by RF biasing on the driven pixel of the "adaptive electrode" is presented. The analysis of the RF sheath and particle charging in it has disclosed a levitation force on particles, which is substantially different from the DC case often used in complex plasmas. Experimentally, the RF heavily-loaded sheath presents characteristics completely different from the normal case $V_{RF} \leq V_{DC}$. Regions of extra ionization and complex electrostatic structures arise and the "secondary plasma" glow modifies the main plasma volume.

Besides the modification of neighboring plasma, the application of DC or RF potentials on selected pixels changes the positions of dust particles suspended in the plasma sheath [96]. Particles are very sensitive to the balance of several forces, among them, electrostatic forces, ion drag, gravity, magnetic forces, thermophoresis, radiation pressure, particle's beam pressure, gradients in the plasma species density and other. Any of the forces above mentioned can be used for particle manipulation. By changing the plasma environment we introduce modification to the force balance, which, in turn, produces new possible positions of particle levitation.

A variety of equilibrium positions for a controlled number of micro-particles can be achieved by fine balancing of DC and RF on a pixel of "adaptive electrode" with the neighboring sheath kept under control. The experiments with particle manipulation using "adaptive electrode" in two cases of the voltage applied on the driven pixel ($V_{RF} \leq V_{DC}$ and $V_{RF} \gg V_{DC}$) have been performed in metallic chamber (section 2.1). Melamine-formaldehyde particles, of 3.4 μm diameter were injected in the chamber for manipulation. In certain situations gravity is completely compensated allowing the study of three-dimensional clusters. The clusters of spherical shapes from 4 to about 100 particles have

Figure 3.1: Normalized electric field $E/(k_B T_e/e/\lambda_D)$versus normalized space x/λ_D for the DC and RF sheath.

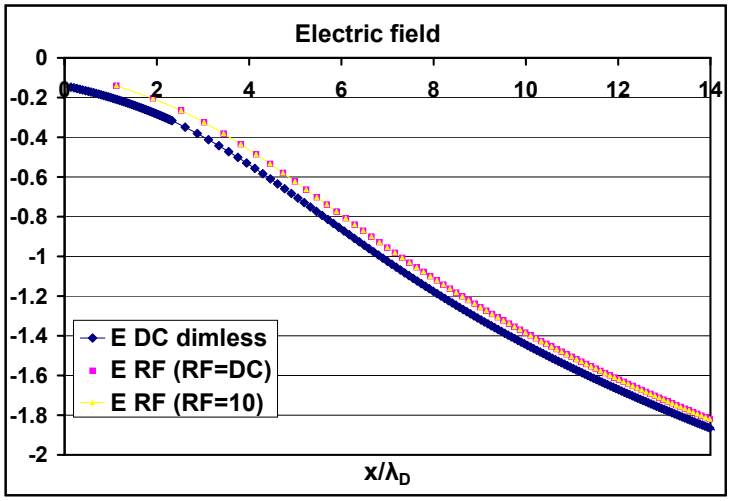

been obtained inside the small "plasma ball". These structures are stable and crystalline. At pressure below 40 Pa in larger clusters a poloidal motion appears. The 3D plasma clusters have been investigated in PKE-Nefedov chamber with 3D optical diagnostics (see section 2.2). The method described enables the study of time varying effects, as transitions and vibrations, as well as the study of static structures and lattice defects.

3.1 The levitation in the case $V_{RF} \leq V_{DC}$

The RF voltage applied to the plasma sheath modifies the DC voltage distribution because of the increased time-averaged electron density. This can be seen in the collisionless Poisson equation:

$$\frac{\partial^2 V_{DC}}{\partial x^2} = -\frac{n_s e}{\varepsilon_0}\left\{\left[1-\left(\frac{V_{DC}}{V_0}\right)\right]^{-1/2} - exp\left(\frac{eV_{DC}}{k_B T_e}\right) I_0\left(\frac{eV_{RF}}{k_B T_e}\right)\right\} \tag{3.1}$$

where V_{DC} and V_{RF} are the potential distributions in the sheath, both measured from the plasma, x is the space with respect to the plasma edge, n_s and V_0 are the plasma density and the energy of the ions at the sheath boundary, T_e is the electron temperature and I_0 is the zeroth order modified Bessel function of the first kind. The first term from the right hand side presents the ion density, and the second one – electron density dependent on RF voltage. The total RF voltage V_{RF} applied to the sheath can be measured by an externally driven Langmuir probe [99]. The condition $V_{RF} \leq V_{DC}$ ensures that the space potential

Figure 3.2: Electron density and ion density for the DC (n_{iDC}, n_{eDC}) sheath and RF (n_{iRF}, n_{iRF}) sheath, where $V_{RF} = V_{DC}$, versus normalized position in the sheath.

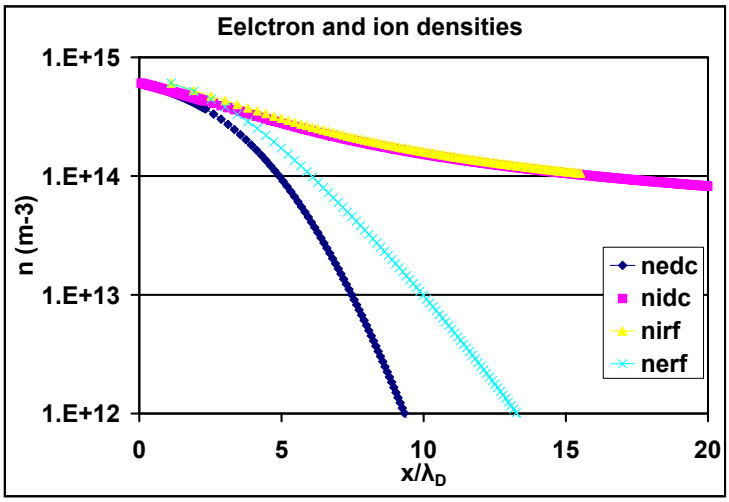

of the sheath is, at any time in the RF cycle, lower or equal to the plasma potential. Eq. (3.1) has been solved for two values of applied RF, $V_{RF} = V_{DC}$, in any point of the sheath and V_{RF} distributed linearly from zero at the plasma potential to V_{RF}=10 $k_B T_e/e$ at the self-bias potential. This latter distribution complies with some of our experiments. Fig. 3.1 shows the distribution of electric fields in these two RF cases and in the DC case for comparison. The effect of the RF is small and this also can be seen from the distribution of the electron and ion density plotted in Fig. 3.2. The ion density is dominant with respect to the electron density even when the RF enhancement of the electron density is taken into account.

The condition of zero total current at the lower electrode gives the floating potential in the DC case and the condition of zero particle current gives the self-bias potential in the RF case.

For electrode potential lower than the floating potential for the DC sheath, or below the self-bias potential for the RF sheath, a net positive current flows out of the plasma. The opposite can be said for potentials above the floating/self bias condition. For zero particle current the condition of $V_{RF} = V_{DC}$ is always complied. However, when an electron current is collected by the pixels the above condition might not hold in every point of the sheath.

3.2 Particle charging in RF sheath

A particle in an RF sheath will be surrounded by more electrons than a particle at the same DC voltage in a DC sheath. Also its floating potential with respect to the local

potential will vary accordingly. While the energy of the ions falling on the wall and on the particle depends only on the DC potential distribution, the charge of dust particles is very much dependent on the acquiring electrons, the quantity of which is different in the DC and in the RF sheath as initially pointed out by [100]. The charge of particles in different positions in the sheath can be deduced using vacuum approximation with the floating potential, U_f, measured with respect to the local space potential, V_{DC}:

$$Q = 4\pi a \varepsilon_0 U_f, \tag{3.2}$$

where a is the particle radius and ε_0 vacuum permittivity.

In collisionless case the floating potential can be derived assuming the conservation of angular momentum from the following equation [100]:

$$\sqrt{\frac{8m_i}{\pi m_e}} exp\left(\frac{eV_{DC}}{k_B T_e}\right) exp\left(\frac{eU_f}{k_B T_e}\right) I_0\left(\frac{V_{RF}}{k_B T_e}\right) = \left(1 - \frac{2e\frac{U_f}{k_B T_e}}{1 - 2e\frac{V_{DC}}{k_B T_e}}\right) \tag{3.3}$$

with m_e and m_i the masses of electron and ion, respectively. The charge of 3.4 μm diameter particles has been calculated in Argon plasma for $V_{RF} = V_{DC}$ and it is shown in Fig. 3.3. The charge multiplied by the electric field gives the levitation force as a function of V_{DC}. The levitation force is plotted in Fig. 3.4 through the dependance of electric field (see Fig. 3.1) and particle charge in it (see Fig. 3.3) as a function of the position in the sheath. The DC case is also shown. Conversely to the levitation in the DC sheath the levitation force in RF does not decrease towards the electrode. The intercepts of the levitation force with the particle weight indicate the equilibrium positions for dust particles. The upper position, close to the plasma, is more stable, because near the electrode any instabilities in the balance of forces will lead to particles falling on the electrode. This upper stable position is closer to the electrode for the RF case than for the DC case.

3.3 Experiments with particles

In order to test the above theory some experiments have been performed in the metallic chamber using the "adaptive electrode". RF voltages adjustable in amplitude and phase are applied to the chosen pixel, while the other pixels are grounded. The particles above the pixel are kept negative with respect to ground by the application of V_{DC}=-10 V as it is shown in Fig. 3.5. Fig. 3.6 shows the particles above the pixel with -9.2 V self bias. This voltage is achieved due to the application of V_{RFpp}=90 V peak-to-peak to the pixel. We can see the same behavior as foreseen by the levitation force shown in Fig. 3.4. Above the self biased surface the particles are more close to the electrode than in the case of DC

Figure 3.3: The particle charge for the DC and RF, ($V_{RF} = V_{DC}$), cases versus the DC voltage.

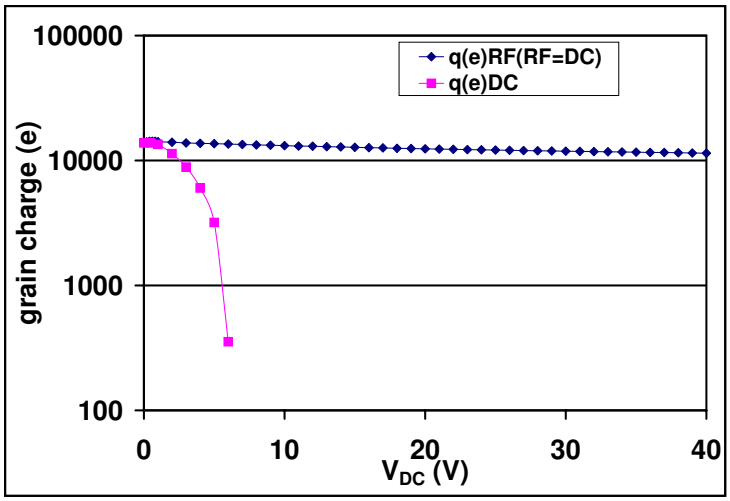

Figure 3.4: The levitation force for particles of 3.4 μm diameter in the DC and RF sheath ($V_{RF} = V_{DC}$). The weight of the particles is also shown.

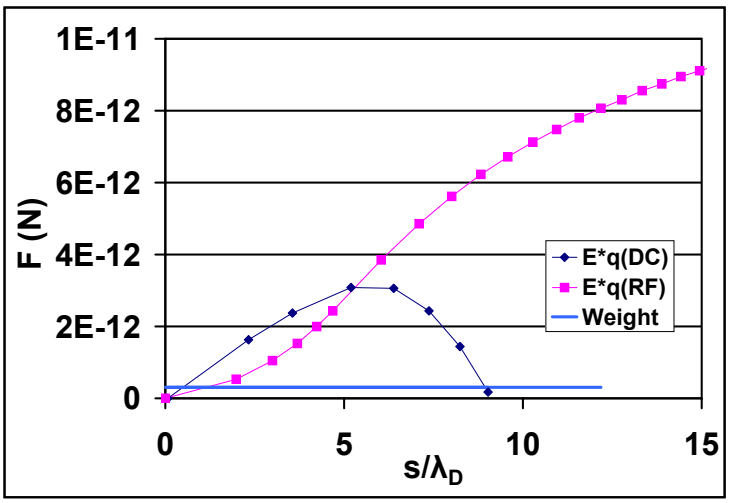

Figure 3.5: The particles above the pixel DC biased at -10 V_{DC}. The pixel is about 1/4 of the picture from the left. The particles are slightly repelled. P=65 Pa, $V_{RFelectrode}$=140 V_{pp}, metallic chamber. Picture size is 16×12 mm^2.

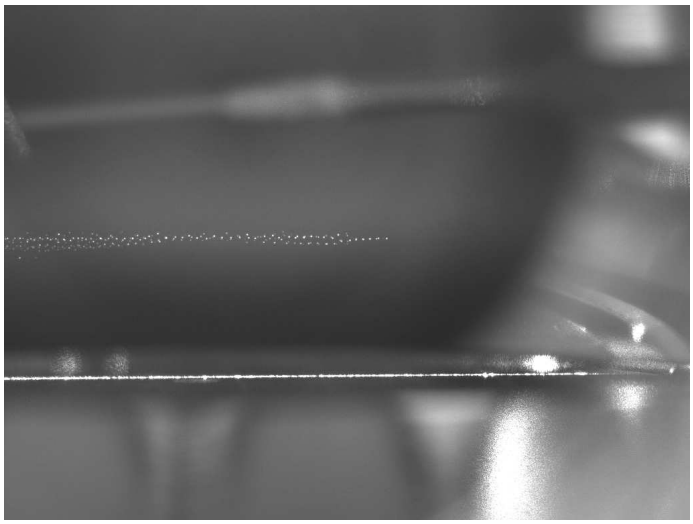

voltage on the pixel. Conversely, when pressure is reduced (in this case from 65 Pa to 13 Pa) the self biased pixel, as well as the DC biased pixel, push the particles away.

Depending on the voltage amplitude on the pixel we can identify two different situations. The first one when the voltage applied to the pixel does not modify the ratio of RF voltages between the driven electrode and the grounded electrode. This is achieved for low RF voltages, low DC voltages applied to the pixel and low pressures. In this case the volume of main plasma is not influenced by the "small plasma" glow, it changes only the sheath region. The other case is when the plasma is substantially modified because of the relative variation of the sheath thickness that modifies the distribution of the RF current. The pixel becomes effectively the main counter electrode.

In both these cases the particles have been successfully transported above the "adaptive electrode" by the consecutive application of RF on adjoining pixels. These experiments have been performed to see if the adaptive electrode could be useful behind a thick dielectric. The motivation for such investigation was the possible application of "adaptive electrode" in window coating technology. Experiments with one glass layer, 1 mm thick, on the adaptive electrode have shown almost the same effects as on the bare electrode. In this case the condition for the maximum localization of the perturbation of the plasma-sheath boundary is that the pixels size must be comparable to the sheath thickness plus the glass thickness.

Figure 3.6: The particles above the pixel self-biased at -9.2 V_{DC}. The pixel is at about 1/4 of the picture from left. The particles are attracted. P=65 Pa, $V_{RFelectrode}$=140 V_{pp}, metallic chamber. Picture size is 16×12 mm^2.

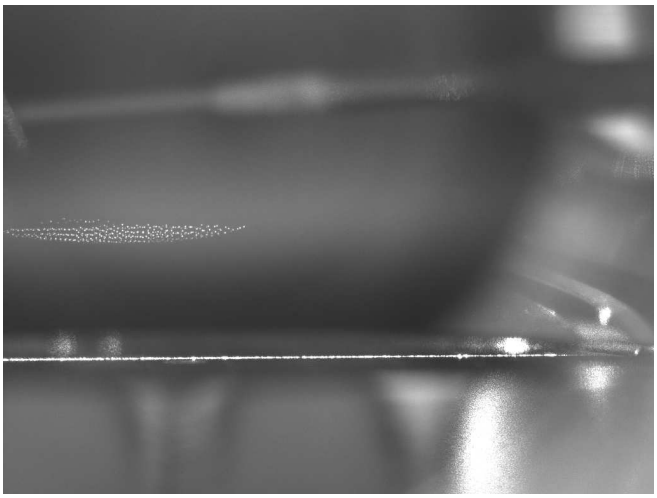

3.4 The levitation in the case $V_{RF} \gg V_{DC}$

When V_{RF} exceeds V_{DC}, the gradient in the averaged electron density is established out of the plasma bulk. However, when $V_{RF} \leq V_{DC}$ in the vicinity of the plasma boundary and $V_{RF} \gg V_{DC}$ only on the deep part of the sheath, the potential can still maintain its negative curvature. The positive charge (negative curvature) is reduced with respect to the DC case, so that the sheath is extending more in the plasma.

The edge of the plasma, being electron rich, has always a negative curvature so that the slow electrons are still confined and the Bohm criterion still holds. Deep in the sheath the electron density increases and the curvature of the electrostatic potential might invert. The electron density depends also on V_{DC} so that a combination of V_{RF} and V_{DC} makes possible a variety of configurations. Bright regions appear near the electrode, as the plasma 'sack' near the anode [101], when the pixel current exceeds the thermal current of the electrons:

$$I_e > \frac{An_0 n_e \bar{c} e}{4}, \tag{3.4}$$

where n_0 is the plasma density, and n_e is the electron density and $\bar{c}$ is the thermal electron velocity. This can be seen in Fig. 3.7 taken at P=88 Pa, the driven electrode excitation V_{RFpp}=250 V and the DC potential of the central pixel kept constant at $V_{DC} = 0$. V_{RF} is increased in opposite phase with respect to the plasma potential fluctuations. For small amount of V_{RF} the RF distribution of potential does not modify the plasma edge (the first picture from the left, upper layer of Fig. 3.7).

Figure 3.7: The glow emitted above a pixel kept at V_{DC}=0 V and RF driven (V_{RFpp}=0, 20, 47, 60, 100, 140 V respectively). Upper electrode voltage V_{RFpp}=250 V, P=88 Pa. PKE-Nefedov chamber.

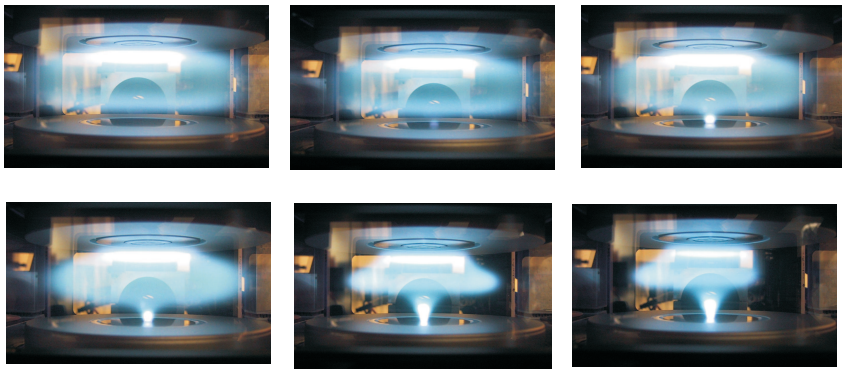

When increasing the RF a weak light appears gradually near the electrode (the second picture from the left, upper layer of Fig. 3.7). Here some electrons are accelerated towards the pixel in the positive part of the RF cycle. These energetic electrons can excite atoms and can ionize. However, their number is limited because the collection is only from the lower part of the sheath. The electron-enhanced sheath, being less positive than that of the neighboring grounded pixels, extends further in the plasma. Particles suspended above the sheath behave as in Fig. 3.5. However, apart from an overall shift, the plasma edge is not much modified. From Fig. 3.2 we can see that increasing V_{RF} above V_{DC} would make the space charge negative (positive curvature) initially at the plasma edge.

At V_{RFpp}=47 V a light ball suddenly appears. The plasma edge is now modified and electrons (and suspended particles) are collected from far away in the plasma because of a negative pre-sheath. The pixel collects a large electron current that induces plasma depletion and a consequent decrease in the plasma potential. Several anode-like effects appear as in the pictures of Fig. 3.7.

The bright regions on two different driven pixel can coexist only for a time of the order of one second keeping the same RF applied as for a single pixel. After this time the bright regions appear only for much higher voltages. If the RF is applied on two adjoining pixels the bright regions merge making one large bright region before disappearing. More experimental work is needed on the co-existence of bright regions and on time variation.

Figure 3.8: Visualization of the sheath structure using "fog". This picture has been taken during a scan of the phase of the RF applied to the pixel. P=24 Pa, $V_{RFdrivenelectrode-pp}$=400 V, $V_{RFpixel-pp}$=174 V, metallic chamber. The picture shows 16×12 mm^2.

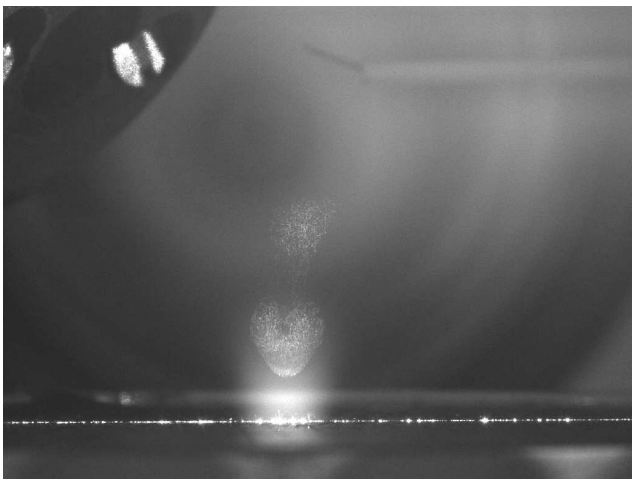

3.5 Visualization of the plasma structure by fine particulate (∼nm) size

A convenient way to visualize the plasma structure above the RF biased pixel is to grow fine particulate in the plasma. We introduced in the chamber surfaces coated with polypyrole (metal). The coating is rapidly etched away and after few minutes nano-particles are clearly identifiable in the plasma, as has also been observed in [102]. The nano-particle concentration increases steadily for about 1/2 hour. The "fog" gives evidence to structures in the plasma sheath, see for example Fig. 3.8 and Fig. 3.9, in which the pressure is 14 Pa and the upper electrode had $V_{electrodepp}$=400 V. The particles can be suspended above the bright glow of the pixel, in the center of the bright glow or very near to the electrode, as in Fig. 3.8 at $V_{RFdrivenelectrodepp}$=400 V. They also can be confined in a very thin layer, as in Fig. 3.9 at $V_{pixelpp}$ = 263 V. In this case aggregation of the particulate forming larger grains has been observed. Although particles found sometimes some equilibrium positions in the positive DC sheath [96], in the great majority of the cases they fall on the electrode. In the RF sheath we find equivalent equilibrium positions but the particles never fall, so that the research can explore a great number of shapes, varying the external parameters, such as pressure, RF on the pixel, RF on the electrode, small correction with added positive or negative DC on the pixel or RF/DC on the neighboring pixels.

Figure 3.9: Visualization of the sheath structure using "fog". This picture has been taken during a scan of the amplitude of the RF applied to the pixel: $V_{RFpixel-pp}$=0-175 V. The phase has been chosen to match the plasma oscillations. P=15 Pa, $V_{RFdrivenelectrode-pp}$=400 V, metallic chamber. The picture shows 16×12 mm^2.

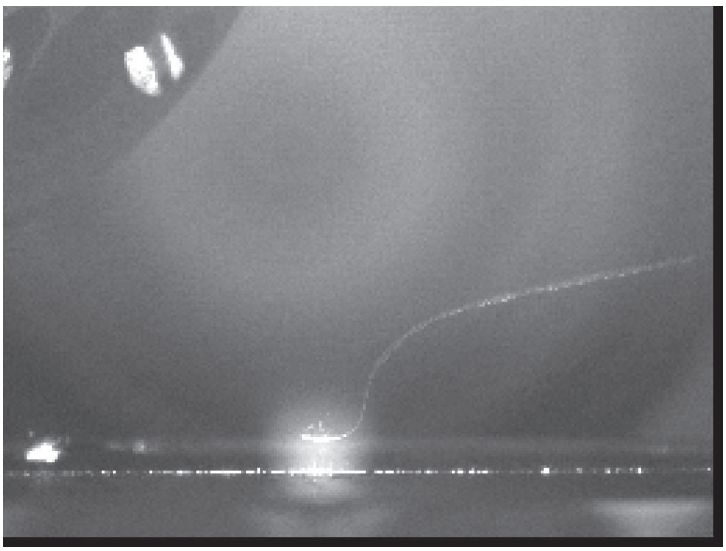

3.6 Three dimensional clusters

When "secondary plasma" glow appears above the driven pixel, micrometer-size particles injected in the plasma start to be gathered into this region. As it has been observed, they can find several isolated equilibrium positions, where three dimensional clusters form. By the fine adjustment of the RF applied to a DC-grounded pixel we were able to control the number of particle in the clusters and also the shape of clusters. The experiments with 3D clusters have been carried out in the PKE-Nefedov chamber with glass walls (chapter 2). The cluster images has been made using 3D diagnostics described in the subsection 2.2.2 of chapter 2. The clusters of relatively small sizes (from 4 up to 73 particles with cluster diameters ranging from 0.35 mm up to 0.9 mm) have been built up due to such particle manipulation. Some examples are given here. Fig. 3.10 shows a 7 particle cluster. In three dimension 7 is a so-called "magic number", because the binding energy of the 7th particle in a 6 particle cluster smaller than the binding energy of the 6th particle in a 5 particle cluster and smaller than the binding energy of the 8th particle in a 7 particle cluster, when the nearest neighbors interaction dominates [103]. This configuration is particularly stable and we could record some vibration on top of the trivial motion of rotation. Fig. 3.11 shows a 12 particle cluster. This number presents a vacancy with respect to the 13 particle cluster, the second magic number in 3D. The icosahedral structure of the 13 particle cluster is formed by layers with 1, 5, 1, 5, 1 particles. In Fig. 3.11 the structure is 1, 6, 5, but in the

Figure 3.10: The cluster of 7 particles. P=76 Pa, $V_{RFpixel-pp}$=120 V, $V_{RFdrivenelectrode-pp}$=176 V. The green-red picture shows 2.3×1.7 mm^2. The same cluster, seen at 90^0 is represented by the blue particles (chapter 2, subsection 2.2.2). PKE-Nefedov chamber.

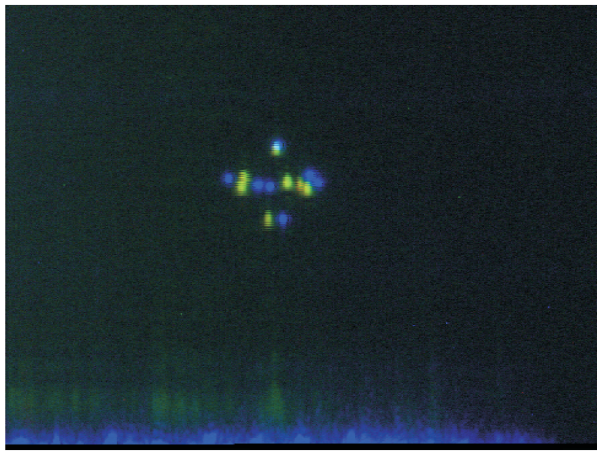

course of the recorded sequence the structure is gradually tending to the configuration 1, 5, 1, 5 leaving the vacancy at one end (and not in the center). Larger clusters could easily be achieved and visualized up to about 200 particles. Fig. 3.12 shows a large cluster of about 60 particles. The vibrations and rearrangement of the particles have been observed in this cluster. The analysis of the particle behavior in the clusters will be presented in the next chapters.

In the equilibrium positions the vertical confinement is provided by the electric field of the double layers/striations combined with the suitable conditions for the charging. The horizontal confinement is another question, which will be discussed below in chapter 5. During the particle collection to the bright region above the driven pixel particles also can get levitation conditions in the upper part of the small "plasma ball", as in Fig. 3.13, or in its lower part very near to the electrode surface (Fig. 3.14).

In the first case the horizontal confinement can be due to plasma pressure, while in the second case this can occur because of internal forces among the cluster component, Lennard-Jones like potential, or by electrostatic confinement of the neighbor pixels.

Fig. 3.15 presents the whole particle structure as we see in the plasma volume: multiple double layers, that form in the sheath loaded with many particles and a spherical cluster in the region of the "plasma ball" above the pixel. More work would be required to explain the double-layer formation in such a particle distribution. This is beyond the scope of this thesis.

Figure 3.11: A cluster of 12 particles. P=56 Pa, $V_{RFpixel-pp}$=120 V, $V_{RFdrivenelectrode-pp}$=300 V. The green-red picture shows 2.3×1.7 mm^2. The same cluster, seen at 90^0 is represented by the blue particles (chapter 2, subsection 2.2.2). PKE-Nefedov chamber.

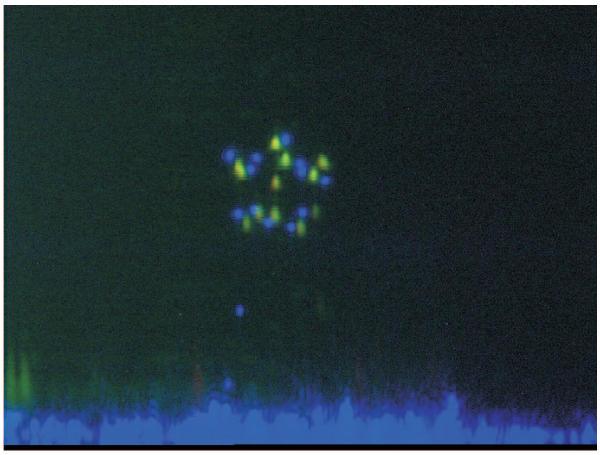

Figure 3.12: A large cluster of about 60 particles. P=56 Pa, $V_{RFpixel-pp}$=120 V, $V_{RFdrivenelectrode-pp}$=300 V. The green-red picture shows 2.3×1.7 mm^2. The same cluster, seen at 90^0 is represented by the blue particles (chapter 2, subsection 2.2.2). PKE-Nefedov chamber.

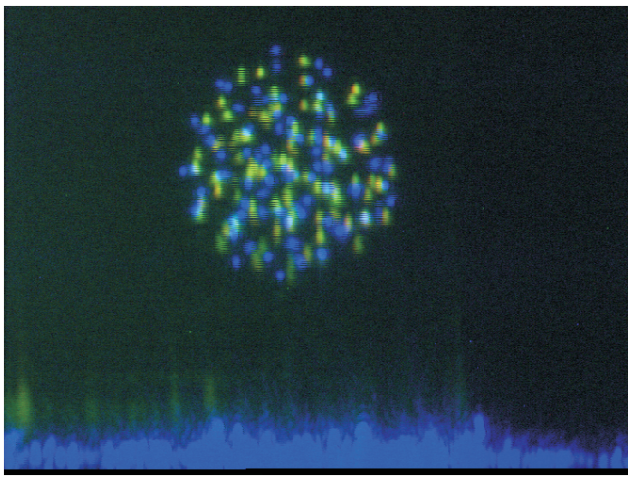

Figure 3.13: Particles in stable equilibrium in the middle of a glow. P=38 Pa, $V_{RFpixel-pp}$=82 V, $V_{RFdrivenelectrode-pp}$=300 V. The picture shows 18×12.5 mm^2. Metallic chamber.

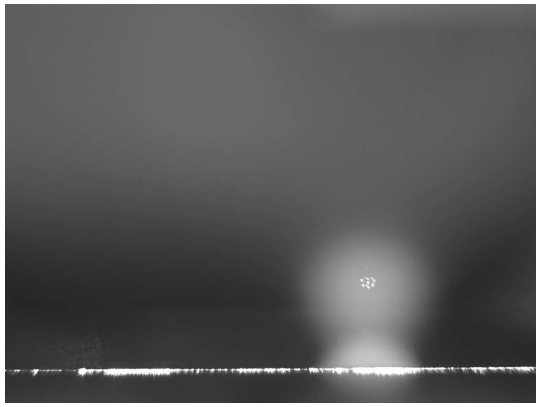

Figure 3.14: Particles in stable equilibrium above a glow. P=38 Pa, $V_{RFpixel-pp}$=62 V, $V_{RFdrivenelectrode-pp}$=300 V. The picture shows 18×12.5 mm^2. Metallic chamber.

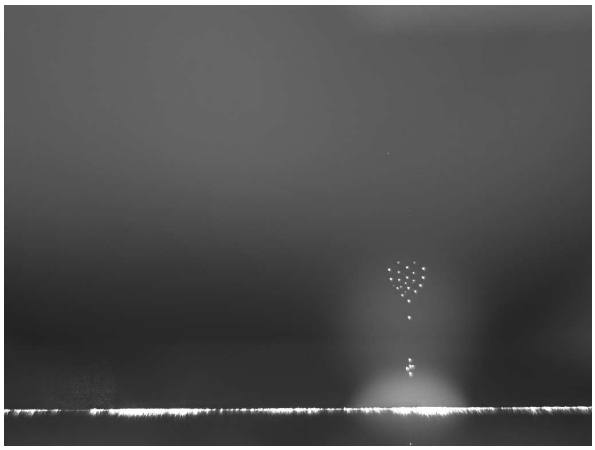

Figure 3.15: A particle heavily loaded sheath. P=76 Pa, $V_{RFpixel-pp}$=110 V, $V_{RFdrivenelectrode-pp}$=200 V. The green-red picture shows 2.3×8.5 mm^2. The same cluster, seen at 90^0 is represented by the blue particles (chapter 2, subsection 2.2.2). PKE-Nefedov chamber.

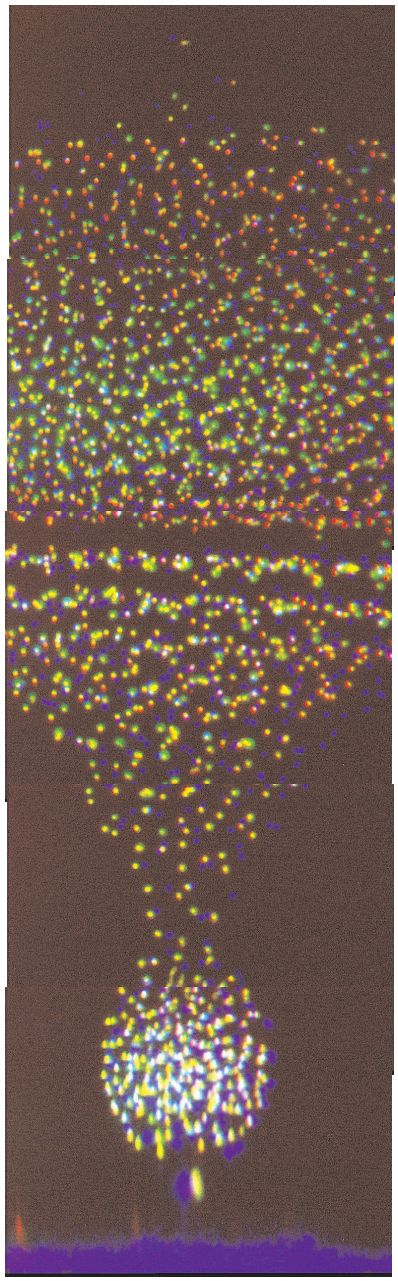

3.7 Conclusions

In this chapter we have described a new plasma configuration, which has been obtained using a segmented "adaptive electrode". The localized RF on the boundary of the main plasma volume produces a glow – "secondary plasma" with the ionization processes inside. The amplitude and phase of RF voltage on the driven pixel determine the parameters of "secondary plasma". Electric field, plasma densities and dependent on them dust particle charge and positions of levitation have been estimated for two cases with DC or RF voltage applied to the pixel. In this situation the RF amplitude has not exceeded the DC amplitude and the volume of main plasma has not been modified. We have experimentally demonstrated that even without a DC applied particles of any diameter can be collected, transported and stored in a flexible and reversible manner. The plasma or chamber properties do not modify qualitatively the effects but might have an influence on the quantitative values of the voltage applied. An obvious application of such manipulation is the cleaning of the plasma, that has been discussed above in the Introduction. In the case of RF$\gg$DC the glow of "secondary plasma" modifies not only the sheath but also the main plasma volume. We have demonstrated also the way to visualize the structure above the RF biased pixel using fine particulates. The grown nano-size particles follow the small glow boundaries and show the potential distribution in the sheath.

The manipulation of dust particles with driven pixel has shown selected positions where the particles can be three-dimensionally confined making possible the study of three dimensional clusters. A three-dimensional simultaneous visualization technique has been used for recording vibrations and structure transitions. The analysis of these effects in the cluster obtained and estimation of the force value among particles in these structure will be done in next chapters.

Chapter 4

Study of 3D plasma clusters' environment by emission spectroscopy

In order to characterize the behavior of the dust particles in the clusters it is necessary to know the parameters of the plasma at the position, where the clusters are situated. As described in chapter 3 the clusters obtained are situated in the "secondary plasma", which is created by a segment of the "adaptive electrode". Because of very small size and the RF nature of the "secondary plasma" Langmuir probes cannot be used. Therefore the spectroscopic analysis has been chosen as the most suitable method of plasma diagnostics. The spectroscopic measurements of the "secondary plasma" and following density calculation and theoretical approaches will be discussed in this chapter.

All clusters have been obtained in Argon discharge at the pressures about 60 Pa, therefore, spectroscopic measurements have been made in Argon at the same pressure and at 30 Pa for comparison. The photomultiplier with several band-path filters for certain range of the radiation wavelengths has been used. With these filters some ionic and atomic lines typical for Argon have been detected. Since the plasma in our experiments is optically thin the steady-state corona model can be used in order to obtain the density of the small "plasma ball".

Theoretically the density of plasma can be estimated in analogy with the analysis of the positive column, which has been done by Schottky and presented by J. Cobine [104]. These calculations were performed for the collisional regime using the ambipolar diffusion coefficient. We followed this procedure here, too, since at 60 Pa pressure we have a strongly collisional case and the collisional approach is very suitable.

Figure 4.1: View of the plasma glow with RF voltage applied to the pixel (opposite phase with respect to upper driven electrode). P=88 Pa and the driven electrode excitation V_{RF}=250 V.

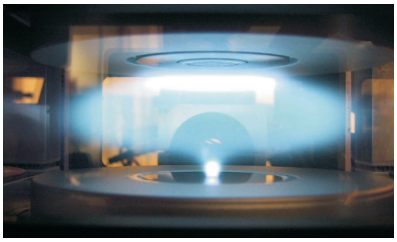

4.1 Experimental evidence

The experiments have been performed in PKE-Nefedov chamber, which has been described in chapter 2. Using the "adaptive electrode" the "secondary plasma" has been obtained just above the lower electrode, as it has already been shown in the previous chapter 3 in Fig. 3.7 for different value of RF amplitude on the pixel and for certain RF voltage in Fig. 4.1. For the spectroscopic measurements we used the same experimental conditions, as there at which the complex plasma clusters had been obtained. The voltage on the driven electrode was 300 V_{pp}; on the small segment - about 150 V_{pp} in opposite phase.

The spectroscopic analysis of the "plasma ball" intensity has been done using a photomultiplier with three filters with the band-path approximately 10 nm (wave length λ=350 nm, which corresponds to a bunch of ionic lines with the upper level of excitation about 23 eV; λ=550 nm with 3 relevant atomic lines of 549.5 nm (15,33 eV), 555,8 nm (15.13 eV), 560.6 nm (15.11 eV); and λ=810 nm with two atomic lines of 811.5 nm (13.07 eV), 810.3 nm (13.1 eV)). We have used a small tube of 0.4 mm internal diameter, length 215 mm to get a space resolution of 0.5 mm in the center of the chamber (see Fig. 4.2). By scanning vertically we obtained the structure of our discharge, with the main plasma glow, two sheath regions and the "plasma ball" glow. The resolution gives us 8 scan points in the "secondary plasma". In Fig. 4.3 the light emission structures at 30 and 60 Pa are shown. In these two figures the large peak from the left presents very bright glow just above the lower electrode, where the "secondary plasma" is. Almost all our clusters are situated in this region. Above the large peak one can see a small peak at 60 Pa but not at 30 Pa. This is the spherical shape part of our small "plasma ball" (see Fig. 4.1). The third large peak, which is present for 60 Pa as well as for 30 Pa, is the main plasma glow. The intensity of "secondary plasma" is higher than intensity of main plasma in all spectrums at 60 Pa and it is lower at 30 Pa. At lower pressures the small "plasma ball" disappears because of the expansion of the main plasma sheath.

Figure 4.2: Sketch of the spectroscopic measurements in plasma chamber. PMP - the photomultiplier, T and r are the length and the radius of the additional tube, L - the distance between walls in chamber, l - the dimensions of plasma emission. (Not in scale).

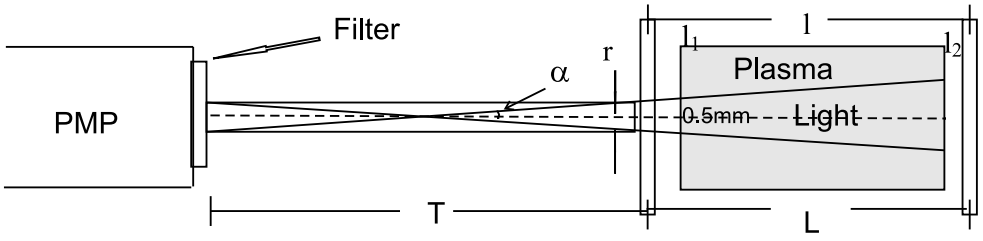

Figure 4.3: The distribution of intensity between electrodes in the discharge measured by photomultiplier at 30 and 60 Pa pressure. The lower electrode is at 1 mm.

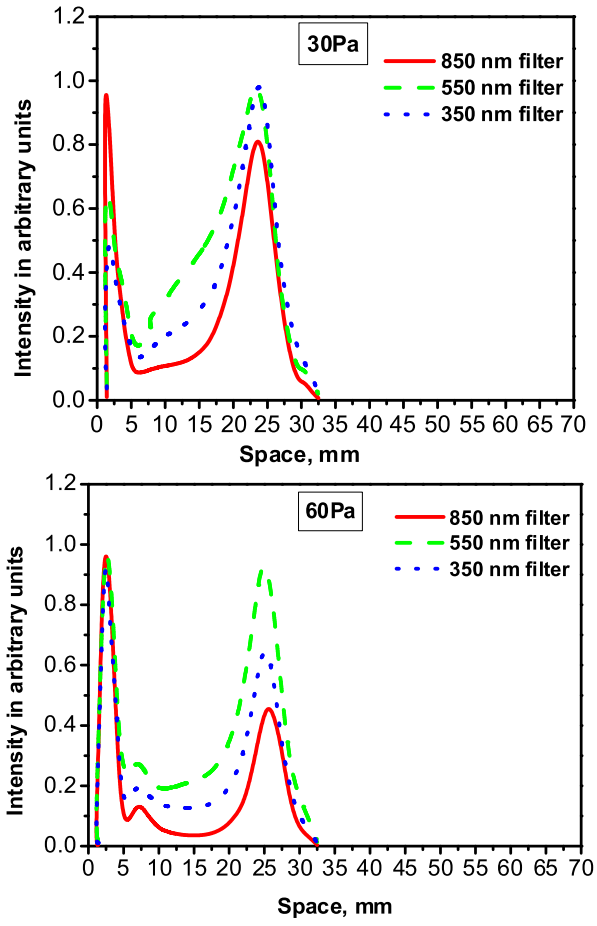

4.2 Corona model

In order to estimate the density of the "secondary plasma" from the spectroscopic data the suitable corona model has been chosen. In the corona model it is assumed that the electron density is low enough that collisional de-excitation can be neglected. Then all upward transitions can be considered collisional from ground state and all downward transitions are radiative. This model is applicable in several cases for analysis of low density laboratory plasma, when the plasma is optically thin, i.e. absorption of radiation can be ignored [105]. We have made the experimental determination of the plasma optical depth by "mirror method". For this purpose a mirror was placed behind the plasma source to compare a single pass intensity I_s and a total reflected intensity I_T. In these terms the optical depth τ can be written as:

$$\tau = \ln \frac{I_s}{I_T - I_s}. \tag{4.1}$$

If $\tau < 1$ the plasma is optically thin and absorption is low. The intensity measurements have been made using a power-meter with a mirror in the pressure range from 30 up to 90 Pa. The optical depth τ was equal to 0.6, this confirms that our plasma is optically thin and the steady-state corona model is a reasonable approximation.

In this model the intensity of a line is an integral function of the electron distribution function and the cross section of the emission:

$$I_{ij} = G n_0 \int_0^\infty \sqrt{\frac{2\varepsilon}{m_e}} f(\varepsilon) \sigma_{ij}(\varepsilon) d\varepsilon, \tag{4.2}$$

where G is the geometric constant factor. $\sigma_{ij} = A_{ij}\sigma(\varepsilon)$ is the cross section for the emission of a photon of frequency $(h\nu)_{ij}$ emerging from the electron impact at an energy ε on a ground-state atom and A_{ij} is the atomic transition probability between quantum levels i and j. n_0 is the population density on the ground level.

The energy range of the spectral lines allows us to use the linearized cross section, when the collisional excitation occurs due to the high-energy electrons in the tail of the Maxwellian distribution [17]. Here $n(\varepsilon) \propto \exp(-\varepsilon/kT_e)$ falls off steeply, so that a linear function can be used for the cross section: $\sigma_{ij} = C(\varepsilon - E_T)$, where E_T is the excitation potential, C is a constant depending on the specific line. After integration eq. 4.2 can be written as:

$$I = GCn_0\bar{c}_e(E_T + 2T_e)e^{\frac{-E_T}{T_e}}, \tag{4.3}$$

where $\bar{c}_e$ is the electron thermal velocity $\bar{c}_e = (8k_BT_e/\pi m_e)^{1/2}$.

4.3 The first method of ion density calculation

In order to calculate ion density in our plasma, we can compare intensities of two lines - ionic I_i and atomic I_a, which have been taken with two filters, 350 nm and 850 nm, respectively:

$$\frac{I_i}{I_a} = \frac{G_i}{G_a}\frac{C_i}{C_a}\frac{n_i}{n_a}\frac{E_{Ti}+2T_e}{E_{Ta}+2T_e}e^{\frac{-(E_{Ti}-E_{Ta})}{T_e}}. \tag{4.4}$$

Here E_{Ti} and E_{Ta} are the upper levels for the most probable lines of Argon in UV (λ=350 nm) and Infrared (λ=810 nm). The geometric factors for ionic and atomic lines G_i and G_a we assume to be the same in our geometry. The constants C_i and C_a are not known. Their ratio can be found by using the ratio of intensities I_i/I_a but only in the volume of main plasma, where the ion density $n_i \sim 10^{15}m^{-3}$ and electron temperature T_e=3 eV are known from Langmuir probe measurements, the density of neutrals n_a at our pressure of 60 Pa is equal to $1.2\times10^{22}\ m^{-3}$. For the ratio in eq. 4.4 the maxima of intensity in main plasma for each spectrum have been used.

With these parameters the ratio of constants C_i/C_a is found to be 2.8×10^6. Now from the same ratio of intensities (eq. 4.4) only in the "secondary plasma" the ion density can be found. It has been calculated equal to $1.6\times10^{16}\ m^{-3}$.

The photomultiplier tube is characterized by the quantum efficiency, which describes its response to different wavelengths of light. In our range of investigations from 350 nm up to 800nm quantum efficiency of our photomultiplier decreases by a factor two. Thus, the intensity obtained in IR spectrum has to be increased accordingly. Hence, the density in the "secondary plasma" can be estimated about $3\times10^{16}m^{-3}$.

4.4 The second method of ion density calculation

The second method to calculate the ion density in "secondary plasma" is to compare the intensities of ionic lines (UV spectrum) in the main plasma volume and in the small "plasma ball". With the hypothesis that the electron distribution is not modified the constants C_i can be cancelled out, but we have to take into account a large difference in geometry between the main plasma and the small "secondary plasma".

Hence, it is necessary to calculate the geometrical volumes of plasma and "plasma ball", from where the light is taken. The volume of the light from the main plasma has been calculated as the emission of a cone section of volume $1/3\pi R^2H$, where R is the radius of the base and H is the cone height. In our case the cone height H is the plasma dimensions

$l_2 - l_1$ plus the length of additional tube, which has been used to get better resolution:

$$G = \frac{1}{3}\int_{l_1}^{l_2} \frac{1}{3}\pi R^2 \frac{\pi r^2}{4\pi(l+T)^2} dl, \tag{4.5}$$

where l_1 and l_2 are the beginning and the end of the emission, T=215 mm and r=0.2 mm are the length and radius of additional tube, R is the radius of the cone base, $R = \tan\alpha(l + T/2)$, $\tan\alpha = r/T/2$ (Fig. 4.2). The factor $\pi r^2/4\pi(l+T)^2$ is a weighting factor, which assumes that the percentage of the light that arrives at the photomultiplier from the emitting spot is the ratio of the "entrance angle" to the full solid angle. The factor 1/3 before the integral takes into account the reduction of the light taken from the center and periphery of the cone base. The volume of the light from the small "secondary plasma" has been calculated as a volume of a cylinder with radius of equal to the height of the small glow h. The height of this cylinder is equal to the diameter of the "secondary plasma" $D = 2r_g$:

$$g = \pi h^2 2r_g \frac{\pi r^2}{4\pi(l+T)^2}, \tag{4.6}$$

r_g is the radius of this glow, which changes depending on the position above the lower electrode. It decreases from 2 mm in the center to 0 at the top of the small glow. The maximum of the ratio G/g is equal to 15. Thus, the ion intensity calculated from eq. 4.4 with the ratio of constants C_i/C_a for the main plasma volume should be multiplied by this factor to give the ion density in the small "plasma ball". The maximum calculated density of "secondary plasma" is of the order of 2×10^{16} m^{-3}, which is in good agreement with the previous calculations.

4.5 Density profile of the "secondary plasma"

Using the measured intensity data we can build the density profile in the "secondary plasma" and compare it with the position of our clusters in order to know more precisely the parameters of the plasma environment surrounding the clusters. Since the scanning of the "plasma ball" gives us 8 points with the scanning step of 0.5 mm, the density has been selected from the each point of the corresponding collection volume of the small glow. The height of small glow is 4.5 mm, larger than the radius in the center (2 mm), therefore it is represented by a half of an ellipse with the major radius 4.5 mm and minor - 2 mm. Then the radius r_g to be used in eq. 4.6, in each point of scanning has been estimated from the equation of ellipse. The density profile is shown in Fig. 4.4. The vertical lines indicate the mean position of the clusters. It is clear that clusters are situated around the maximum of the density. Hence, we can conclude that the density of the "plasma ball", which surrounds

Figure 4.4: The dashed curve presents the profile of the density expressed by *sin* function from the first theoretical model, the solid curve presents the density profile assuming ionization constant in volume from the second model, and the curve with squares presents experimental density profile in the secondary plasma, which have been plotted in dimensional units with $y = n/n_{Max}$ and $x = x/R - 1$. Two vertical lines show the upper and lower borders, where the plasma clusters are situated.

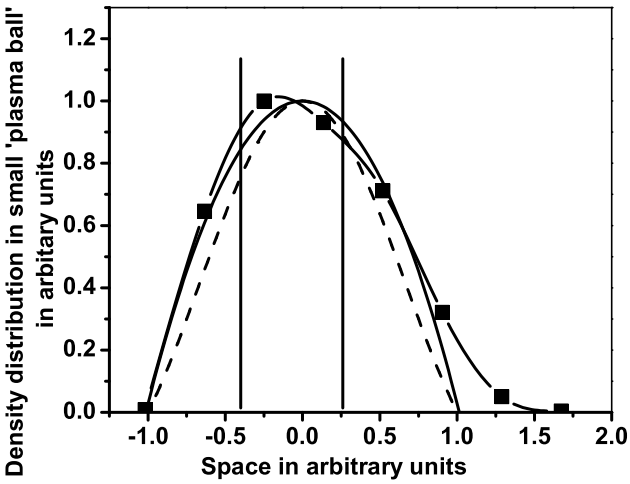

our clusters, is equal to the maximum density estimated from the spectroscopic analysis $\simeq 2 \times 10^{16}\ m^{-3}$.

4.6 Theoretical calculation of "plasma ball" density

The density of plasma can be obtained in analogy with the analysis of the positive column, which has been done by Schottky and presented by J. Cobine [104]. The calculations have been performed for the collisional regime using the ambipolar diffusion coefficient. To estimate collisionality we compare the dimensions of the system with the mean free path of ions in Argon $\lambda = 1/n_a\sigma$, where n_a is a number of atoms, σ is the cross section for collisions in Argon, which has been measured using ion cyclotron resonance by Wobshall *et al.* [106]. For low ratio of electric field to pressure, E/p, with the energies at or near thermal, $\sigma = 2.15 \times 10^{-18}\ m^2$. At 60 Pa the mean free path for ions is estimated about 32 μm. Thus, the ratio of the small glow dimensions and mean free path is 140, this suggests a strongly collisional case.

Hence, we can use the collisional model described in [17]. The plasma is considered to

be quasineutral, i.e. $n_e = n_i = n$. The flux of ions moving toward the wall by diffusion is:

$$n\mathbf{v} = -D_a \nabla n, \tag{4.7}$$

where D_a is a coefficient of ambipolar diffusion, v is the ion rate. In order that the plasma concentration remains in equilibrium, the ion flux should be compared to the number of electrons, which take part in ionization:

$$\nabla \cdot (n\mathbf{v}) = Zn, \tag{4.8}$$

where Z is the number of ionizing collisions per second made by each electron.

Combining these two equations we obtain:

$$\nabla^2 n + \frac{Zn}{D_a} = 0 \tag{4.9}$$

In the case, described by J. Cobine [104] calculations have been made for a portion of a cylindrical discharge tube, whilst we have a "plasma ball" of spherical shape. We consider a portion with radius r of a spherical shell of radius R. Thus, for the spherical case eq. 4.9 should be written as following:

$$\frac{d^2 n}{dr^2} + \frac{2}{r}\frac{dn}{dr} + \frac{Zn}{D_a} = 0. \tag{4.10}$$

Making substitution $r = \sqrt{D_a/Z}x$ we get the following equation:

$$\frac{d^2 n}{dx^2} + \frac{2}{x}\frac{dn}{dx} + n = 0. \tag{4.11}$$

The solution of such an equation is the spherical Bessel function of the first kind $j_m(x) = \sqrt{\pi/2x}J_{m+1/2}(x)$. For the case $m = 0$ the solution is the zero order Bessel function $j_0(x) = \sin x/x$ and $n_r = n_0 j_0(x)$. n_0 is the concentration of ions at $r = 0$. This function approaches zero value, when $x = \pi$, which corresponds to the radius of a sphere R:

$$x_R = R\sqrt{\frac{Z}{D_a}} = 3.1415 \tag{4.12}$$

Thus, the density distribution is found to be:

$$n_r = n_0 \frac{\sin(\pi r/R)}{\pi r/R}. \tag{4.13}$$

Since, the density distribution in our "secondary plasma" is described by the function

$\sin x/x$, we can compare the behavior of this function with the density profile obtained from the experimental measurements of the intensity. In Fig. 4.4 the function $\sin x/x$ is shown together with the density profile in the "plasma ball". One can see that the behavior of these two curves are very similar.

In our small "plasma ball" the distribution of ions and electrons, is radial, therefore, for the analysis of "secondary plasma" we can estimate the outward flux of ions from the center. The ion flux is proportional to the ion density integrated over the volume of our sphere with radius R:

$$J_i = 4\pi R^2 D_a \left(\frac{dn}{dr}\right)_{r=R} \tag{4.14}$$

Another approach to find the density distribution is to assume that the number of ionizations Zn is a constant in the volume and does not depend on the distance from the center, then $\nabla(nv) = C$. In that case our model should be built on the next two equations:

$$n\mathbf{v} = -D_a \nabla n, \nabla \cdot (n\mathbf{v}) = C \tag{4.15}$$

From these equations for the spherical ball we have:

$$\frac{1}{r^2}\frac{d}{dr}\left(r^2\frac{dn}{dr}\right) + \frac{C}{D_a} = 0 \tag{4.16}$$

After integration the density is expressed as following:

$$n_r = n_0\left[1 - \frac{C}{6D_a n_0} r^2\right] \tag{4.17}$$

The flux of ions at $r = R$ is equal to $J_i = 4/3\pi R^3 C$. If $n = 0$ constant $C = 6D_a n_0/R^2$. We have $R^2 = \sqrt{D_a/Z}\pi$, hence, the ion flux is:

$$J_i = \frac{8R^3 Z n_0}{\pi} \tag{4.18}$$

The behavior of the density profile from this model is also shown in Fig. 4.4. It describes the experimental density profile even better than the previous model, although we do not have any evidence to assume the ionization to be constant in the "plasma ball".

4.7 Conclusion

In this chapter we have presented the results of spectroscopic analysis of 3D plasma clusters' environment, which is a plasma of very small size (appr. 32 mm^3). The spectroscopic analysis has been chosen as the only possible non-invasive method. Using the steady-state

corona model and calculation of the geometrical volumes of main and "secondary" plasmas the density of small "plasma ball" has been obtained. This information is fundamental for the plasma cluster investigations, since it gives us the possibility to estimate the screening Debye length in the plasma and, hence, the scaling of the distance between particles in the small clusters, which defines the cluster structures. We assume that electron losses on particles of 3.4 μm diameter are always too small to modify the density distribution in the "secondary plasma" volume. The density profile obtained using the data of discharge intensity helps us to estimate more correctly the plasma density near the clusters. The measured profile of the discharge intensity shows the complicated structure of the RF discharge with additional bright part in the sheath region - "secondary plasma". At the chosen experimental conditions the "plasma ball" intensity was higher than intensity of the main plasma, that resulted in a larger density of "secondary plasma". Besides, the density distribution is compared to the results of two theoretical models built on the principles of the ion collisional motion. Both of the theoretical approaches demonstrate good agreement with the experimental data. The first model assumes the ionization proportional to the density. The second one considers ionization to be constant in volume and coincides even better with density profile. Since we do not have any compelling reason for constant ionization in our system, this result should not be overinterpreted. We only have a small number of experimental points (because of the small volume of "secondary plasma") and experimental uncertainties in the measurement are difficult to determine anyway.

Chapter 5

Pair-interaction force in small 3D plasma clusters

5.1 Introduction

Due to the specific shape of the discharge with the "adaptive electrode", which forms the "secondary plasma" in the sheath of the main plasma, we were able to obtain 3D spherical structures (plasma clusters) under gravity conditions, as described in the previous chapter. In the next two chapters we will analyze the structure and the behavior of particles in some of the clusters obtained.

Considering the particle assemblies a fundamental issue at this point is the nature and form of the forces, which keep particles together. There is a growing theoretical and experimental interest in the possibility of attraction between particles in a plasma [107], [69], [30], [67], [74], with experimental techniques using collisions [67] and laser manipulation [74]. In the present work repulsive/attractive forces among particles suspended in a plasma are estimated for the first time from the observation of their spontaneous motion in three-dimensional plasma clusters. The main features of these measurements are: 1) weak (external) confinement, 2) the particles levitate inside the plasma region and not in the plasma sheath, 3) the particle number in the clusters can be externally controlled, 4) novel 3D diagnostics described in chapter 2 allows us to reconstruct the kinetics of the particles. The possibility to get 3D plasma clusters was already pointed out in the work of Arp *et al*. [94] using strong external confinement and "scanned" visualization. Our work is complementary to [94], since we use a completely different system to "construct" and characterize 3D plasma clusters.

5.2 Methods of measurements

The experiments have been performed in the PKE-Nefedov chamber, which has been described in section 2.2. Typical conditions are: RF voltage on the upper electrode in the range of 200-300 V_{pp}, about 150 V_{pp} in "push-pull" on the lower central pixel, Argon pressure from 35 to 70 Pa and melamine-formaldehyde particles of 3.4 μm diameter. The particle clusters are assembled in the "secondary plasma" just above the lower electrode (see chapter 3). The particle number in the cluster can be controlled by varying the RF applied to the pixel. Since the microparticles all carry negative charges, one would presume that internal electrostatic pressure would disperse the cluster without strong additional external confinement. External confinement can, in principle, be due to electrostatic fields, ion or neutral drag/pressure. In addition, there could be an attractive force between the charged particles. The analysis of the cluster structures and the particle motion inside clusters has been done using 3D optical diagnostics (see section 2.2).

5.3 Particle charge

The charge on the particles can be estimated from different theories, see table 5.1.

Theory	O.M.L.	A.B.R.	A.B.R.(collis.)
$V_f(kT_e)/e$	2.1	0.33	0.533
charge (e)	24814	3899	6298
$\vec{E}_{levitation}(V/m)$	76.5	486.9	301.5
$Energy_{ions,1m.f.p.}(eV)$	$2.3{\cdot}10^{-3}$	$1.5{\cdot}10^{-2}$	$9.1{\cdot}10^{-3}$

Table 5.1: Estimated values for the floating potential on isolated particles according to different theories. The charge on the particles, the electric field needed for levitation and the energy acquired by the ions in a m.f.p. are also shown.

The OML (orbital motion limited) [39] theory is not applicable in our range of pressures because typical values of the mean free path ($m.f.p. = 30$ μm at 60 Pa) are much shorter than the Debye length, which is about 160 μm using a plasma density of 10^{16} m^{-3}, deduced from the bright glow by spectroscopic measurements (see chapter 4), and an electron temperature of 5 eV (somewhat higher than the main discharge). The ABR theory (Allen - Boyd - Reynolds theory for radial motion) [25] and the moderate collisional regime [108] are based on the hypothesis of "cold" ions. They could be applied here. The actual floating potential acquired by a particle in the cluster is reduced with respect to an isolated particle due to the presence of the nearby particles. We therefore believe that a reasonable estimate of the charges lies between 3000 to 5000e.

Figure 5.1: A cluster of 4 particles. a) particles before interaction, b) particle A is attracted by the orbital particle B. Units on the axis are in millimeters. (P=57 Pa, peak to peak voltage are $V_{RFpixel}$=120 V, $V_{RFdrivenelectrode}$=300 V). Depth visualization uses variation in particle (sphere) size, larger spheres are "closer" (have higher z values) than smaller spheres.

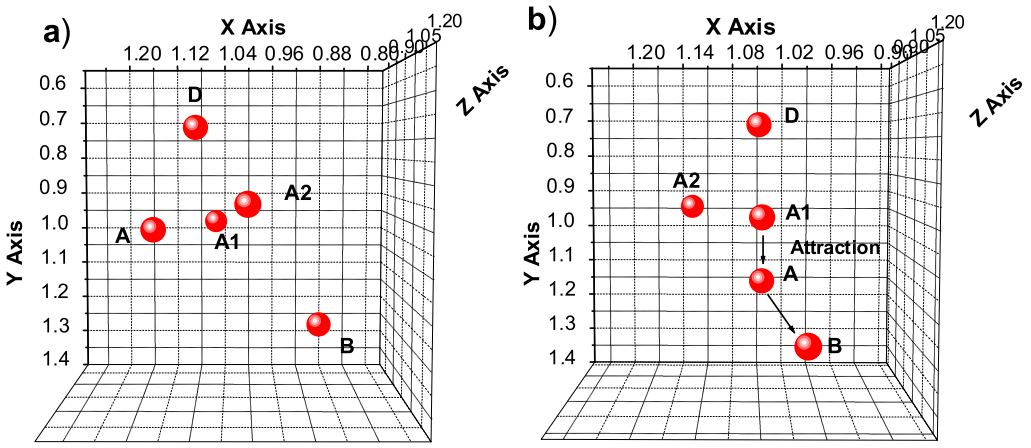

5.4 Description of particle kinematics

We analyze here the dynamical behavior of a cluster consisting of 4 particles A,A1,A2,D (Fig. 5.1a), interacting with a fifth (B) orbiting below the cluster. Particles of different shapes orbiting in a plasma have been observed in DC and RF experiments [109]. The cluster is periodically distorted by the motion of the lower particle. At some point, due to thermal vibrations, the distance between a cluster particle A and the orbiting particle B becomes shorter than the distance to the upper cluster particle D. In this case particle A breaks its bond with the upper particle D and starts to move in the direction of the orbiting particle B (Fig. 5.1b). As soon as particle B proceeds further and the distance AB increases, particle A returns back and takes its place inside the structure, "pushing" on its neighbors to restore equilibrium. The motion of particle B is almost elliptical, this will be used later to estimate the external confinement force. The particle separation distance as a function of time for particles A,B and A,D is shown in Fig. 5.2, which allows us to determine the interparticle interaction force in this distance range. We note here that for separation >0.3 mm the particles do not interact, while the maximum force occurs at about 0.2 mm.

Figure 5.2: Distance between particles A and B, and A and D. The two peaks at frame 155 correspond to attraction.

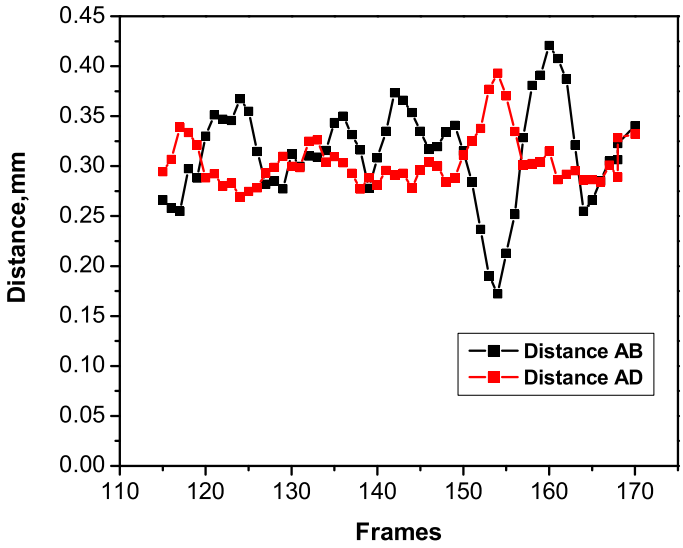

5.5 Analysis of forces in small clusters

The force has been derived from the kinematics of the motion $\sum_i \vec{F}_i = M\,\ddot{\vec{x}} + \gamma\,\dot{\vec{x}}$, where M is the mass of the particle and γ is the neutral drag constant given for spheres by Epstein [65] $\gamma = \delta\frac{4\pi}{3}Nm\bar{c}r^2$, where $N, m, \bar{c}$ are the number per unit volume, the mass, and the mean speed of the neutrals, and r is the radius of the particle. In our calculations we used the coefficient for diffuse reflection with accommodation (δ=1.442). At the Argon pressure for our experiment the inertia is always much smaller than the neutral drag. From the 3D trace left by a moving particle we derived the vector velocity, from which we determined the instantaneous vector force acting on a particle. This force is due to systemic forces as well as the influence of all the other particles' fields.

In order to separate these components we proceed in the following way: 1) by assuming that the orbital motion of particle B is due to external confinement field only, we may estimate the maximum strength of this force, and 2) by assuming that the main contribution to the force on particle A is due only to the nearest two neighbors we can estimate the pair-interaction force from the kinematics of the motion. In the first approximation we derive the upper limit for an external confinement force by equating it with the measured centripetal force, which acts on the rotating particle. Using a mean orbit radius of 0.219 mm the maximum estimated centripetal force $F = MV^2/r$ is $1.4{\cdot}10^{-15}$ N at the maximum velocity of 3.2 mm/sec and the minimum force is $0.55{\cdot}10^{-15}$ N at the minimum

velocity of 1.97 mm/sec. A more detailed orbit investigation did not show any particular radius dependence. Also, this particle is only 387 μm above the electrode, which implies that its vertical deflection due to other forces is correspondingly small. May be the orbiting particle in our experiment has non-spherical shape or it is an agglomeration of two particles. Since this fact does not influence the calculations, it has been assumed that this particle is similar to others in the cluster.

From the second component of the force due to nearby particles we can derive the pair-interaction force solving the following equations:

$$F(d1)\cos\alpha + F(d2)\cos\beta = \gamma V, \tag{5.1}$$

$$F(d1)\sin\alpha + F(d2)\sin\beta = 0, \tag{5.2}$$

where $F(d1)$ and $F(d2)$ are the forces as function of distances with respect to the two nearest particles in each frame, α and β are the angles between the line connecting the particles and the trajectory and V is the relative velocity.

The sign of the forces $F(d)$ is estimated using both the previous and the successive frame. The result is shown in Fig. 5.3. One can see, that the maximum attractive force (negative part of the plot) occurs at the interparticle distance 0.194 mm and it is fairly high, $2.4{\cdot}10^{-14}$ N. For separation larger than 0.25 mm the attractive force rapidly goes to zero and the particles essentially do not interact any more. If the distance between particles is less than 0.177 mm, they repel each other. The error bars are due to the pixel discretisation of particle position and trace. (Note that changing the value for δ will lead to a re-scaling of the vertical axis, but will not alter the generic shape of the curve). From these measurements it is clearly seen that the centripetal force (and by implication an external confinement force) is much smaller than the measured interactive force among particles in this cluster. Hence, the particle motion cannot be explained using external confinement alone.

5.6 Attractive forces in medium size clusters

Here we analyze a cluster of 73 particles, where both systemic and collective attractive force may exist. In the recorded time sequence one of the particles is very mobile (Fig. 5.4). This particle has an orbital trajectory with radius r=0.275 mm, which most of the time is external to the cluster. The full orbit takes about 0.4 sec, the maximum velocity is 1.26 mm/sec. During this external motion the average distance from the nearest particle in the cluster is 0.181 mm, the minimum distance is 0.162 mm and the maximum distance 0.198 mm. Since the particle may escape from the cluster but cannot leave it completely,

Figure 5.3: Measured interparticle's force with respect to distance.

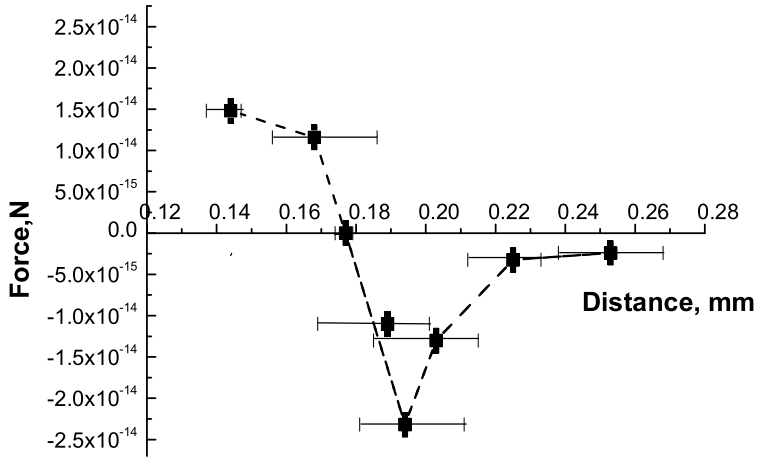

there must be an attraction force which balances the centripetal force. From the particle dynamics, observed radius of curvature (r=2.84 mm). This force is calculated to be $1.7{\cdot}10^{-16}$ N. It may not be the highest value, because the radius is determined by a balance of the attractive force and by the repulsion from the outer shell of the cluster. We do not have a direct measurement of the confinement in this case.

5.7 Discussion

Our experiments have provided new information regarding binary and collective interaction processes in complex plasmas. In a weakly confined system, particle clusters of various size were assembled and the individual particle dynamics was studied.

For small clusters we may assume that collective effects are not important and that the particle dynamics is dominated by binary interactions and the external confining field. The force due to the latter was calculated from the particle orbit ($\sim 10^{-15}$ N). The binary interaction was calculated by assuming (in a small 4 particle cluster) that nearest neighbor effects dominate. This yielded a repulsive force at small particle separation (<0.17 mm) - as expected from electrostatic interaction - and an attractive force at larger distances, with a maximum attractive force of $2.4 \cdot 10^{-14}$ N (see Fig. 5.3). Since this force is more than an order of magnitude larger than the calculated (systemic) confining force, we believe that we were able to identify (for the first time) an attractive component of the binary interaction between particles in plasma, not in the sheath. There are different theories about such interaction: 1) the vertical "pairing" observed in the plasma sheath [74] caused

Figure 5.4: Cluster of 73 particles. The black spheres show the positions of the moving particle in 15 consecutive frames. Units on the axis are in millimeters.

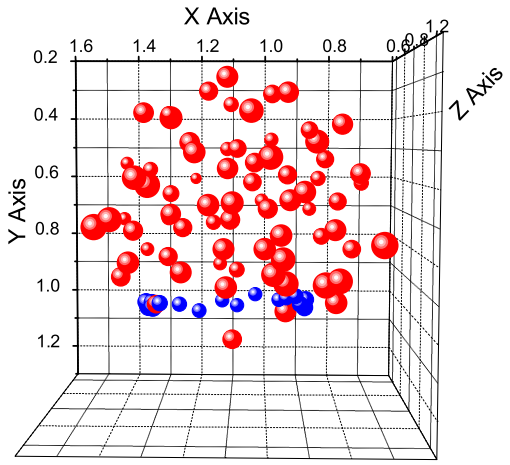

by wake-effects in the pre-sheath streaming ions. This situation does not apply to our experiment, which was conducted in the bulk plasma, we accordingly did not observe any particle alignment. However, in the presence of strong ionization we cannot rule out particle interaction related to the ion drifting in the pre-sheath; 2) there could be an attractive force due to induced dipoles caused by charge redistribution in the field of the nearest neighbor particle. This process is believed to be important in "supercoagulation" or gelation phase transition [110]. The force due to such an induced dipole would vary as r^{-4}, which is compatible with our measurements (Fig. 5.3); 3) attraction can also be produced by the so-called "shadow force" - the mutual shielding of plasma (or neutrals) providing an attractive pressure-like force that varies as r^{-2}. Within the experimental uncertainties this may also just be feasible (Fig. 5.3).

In a large cluster (investigated in a separate experiment) collective effects should dominate (eg. double-layer formation at the surface of the cluster [2], [111]) and binary interaction processes may be expected to be masked by these. The attractive force in the large (73 particle) cluster was measured at a mean distance from the central axis of 0.275 mm. That is much larger than the distance of 0.16 mm in the small (4 particle) cluster, which was used to measure the confinement. Therefore, the confinement force measured for small clusters cannot be taken to apply to large cluster as well.

Since in the small cluster we may safely assume that the external (systemic) confinement is not modified by the microparticles, we believe that the measured $\sim 10^{-15}$ N force is due to the field produced by the shaped plasma from the pixel-electrode. The large cluster (because of the larger dimensions, r=0.45 mm), modifies the ion and electron population by

recombination and by the changes in effective plasma potential, reducing the confinement. We suggest here that the effects of collective forces may have been seen for the first time. In a future series of experiments we will investigate this possibility systematically.

5.8 Summary

The interaction forces between particles in a 3D plasma cluster under weak external confinement have been estimated. A suitable combination of DC and RF applied to a small electrode provided gravity compensation, uniform over dimensions much larger than the cluster itself. The forces acting on the particles could be reconstructed due to unique three-dimensional diagnostics, which allows us to obtain coordinates and velocities of all the particles simultaneously. The measurements yield a maximum (external) confinement force of $1.4{\cdot}10^{-15}$ N and interparticle force that is repulsive at short distances and attractive at larger distances, with a maximum attractive force of $2.4{\cdot}10^{-14}$ N at particle separation 195 μm.

Chapter 6

Limit of the co-operative regime in 3D plasma clusters

In the crystalline assemblies the particles are strongly coupled and the characteristics of individual interactions as well as the properties of the whole structure (as a macro-system) can be investigated. In the previous chapter we have considered the smallest cluster and the pair-interaction of particles in it. In this chapter the effects observed in the clusters of larger sizes will be studied. In the clusters of 17 and 63 particles rearrangements inside the structures have been observed. We assume that particles change their positions inside clusters in order to find an energetically more stable state and, hence, for the whole system to attain the minimum energy. Energy estimates in both clusters will be made.

Moreover, in the cluster of 63 particles characteristic oscillations have been observed. In the cluster of 17 particles, vibrations are not strong, possibly, because of the small number of particles. We will compare the oscillations in the 63 particle cluster with two kinds of oscillations of relevance: 1) dust-acoustic waves (using a kinetic approach) and 2) vibrations of a liquid drop with surface tension (applying a hydrodynamic approach).

As shown in chapter 5, in our experiments the external confinement has negligible influence on the processes inside the clusters. This makes it possible for the first time to conduct high accuracy kinetic studies of generic importance.

6.1 Experimental procedure

The clusters have been obtained in the PKE-Nefedov chamber (chapter 2) by the method described above (see chapter 5). Melamine-formaldehyde particles of 3.4 μm diameter have been injected inside the chamber and form spherical 3D structures in the so-called "secondary plasma" above the segmented "adaptive electrode". A 3D optical system together with programming analysis, has been used to obtain simultaneous information about the

Figure 6.1: A cluster of 17 particles. The black spheres show the positions of the moving particle during its way to the inner shell. The light spheres show the outward motion. Units on the axes are in millimeters.

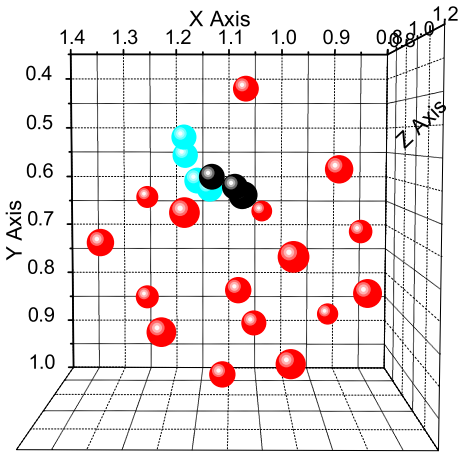

three coordinates of the particles (chapter 2, [112]) .The particles' velocity vectors could be measured in 3D from the analysis of traces, recorded during the shutter opening time of the CCD. By this technique fast processes in the clusters can be detected.

6.2 Changing of the system energy after the arrival of new particles

A change in structure has been observed in the cluster of 17 particles obtained at 76 Pa pressure (200 V_{p-p} on the upper RF driven electrode and 110 V_{p-p} on one pixel of the "adaptive electrode"), when it is impacted by an external particle with velocity more than 12 mm/sec. This particle penetrates the cluster, pushing and re-arranging neighboring particles. It has an unstable position and moves around in order to find its equilibrium. We were able to follow the dynamical evolution of the excited cluster to its new equilibrium. Finally, after 1.12 sec, this particle comes to rest at the external surface of the cluster having lost the kinetic energy acquired in the collision (see Fig. 6.1).

The rearrangement inside the structure can be explained by the motion of one particle to find an energetically preferable position. This provides a minimum energy for the whole system. Linearizing the interaction force from [112] for small displacement, the energy of the n^{th} binary bond can be expressed by:

$$E(n) = \frac{1}{2}K(d - d_{0_n})^2, \tag{6.1}$$

where the force gradient K is taken from the slope of the interaction force at the equilibrium position, for example, in [112] $K = 1.5 \cdot 10^{-9} N/m$. d is the distance between two particles in the chosen frame, and d_{0_n} is the mean distance between particles in one frame. If particles are far away from each other, it can be assumed that they do not interact any more. This cut-off of interaction can normally be estimated as an intermediate point half way between the first and the second shell. However, since the cluster of 17 particles only has one shell (see Fig. 6.2,a), we have used the behavior of the interaction force [112] and have chosen the value of 0.25 mm as a cut-off distance for interaction for this purpose. After the displaced particle has come to rest, no further motion inside the structure was observed besides the thermal vibration. This state of the cluster can be considered stable, and the distances between particles are near equilibrium. The whole energy of the system can be calculated with respect to the number of bonds n:

$$\sum_n (E(n) + \frac{1}{2} K (d_{0_n} - d_0)^2), \tag{6.2}$$

where $E(n)$ is the energy, calculated from eq. 6.1, d_0 is the mean distance between particles, which is taken as the equilibrium distance in the stable state structure. There are two methods to estimate this distance: 1) the frame with the minimum energy has been identified where the structure is stable enough (no dramatic reorganizations are observed). The mean distance between particles is then measured, $d_0 = 200\ \mu m$; 2) the second way is to analyze the shell structure of the cluster. There is only one shell for the cluster of 17 particles, therefore, this method can be applied only for larger clusters (for example, 63 particles (Fig. 6.2, b)).

Fig. 6.3 shows the changes in averaged bond energy during 60 frames (2.16 sec), which contains the rearrangement and transition to the equilibrium. The energy after the rearrangement (30th frame) is lower. The peaks correspond to the frames, in which larger changes of the displaced particle's position were observed. We can conclude, that after the arrival of one new particle, the system goes through a transition state to a final state with minimum energy.

6.3 Changing of the system energy after escape of one of the particles

Particles leaving from the top of a cluster of 63 particles at 57 Pa pressure have been observed (300 V_{p-p} on the upper RF driven electrode and 120 V_{p-p} – on the pixel) . Without any external manipulation 3 particles left one by one from the top of the cluster

Figure 6.2: The structure of shells in the clusters of 17 (a) and 63 (b) particles.

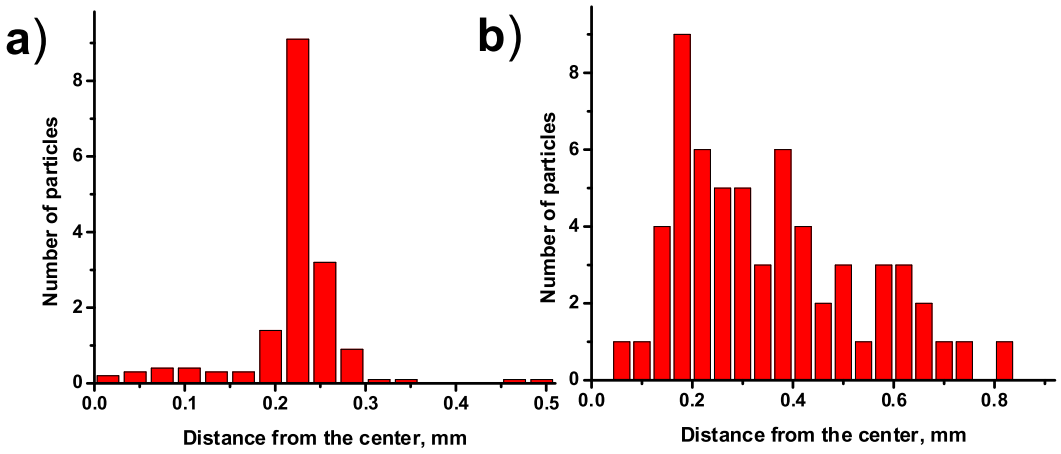

Figure 6.3: The derived energy of the 17 particles' cluster in time.

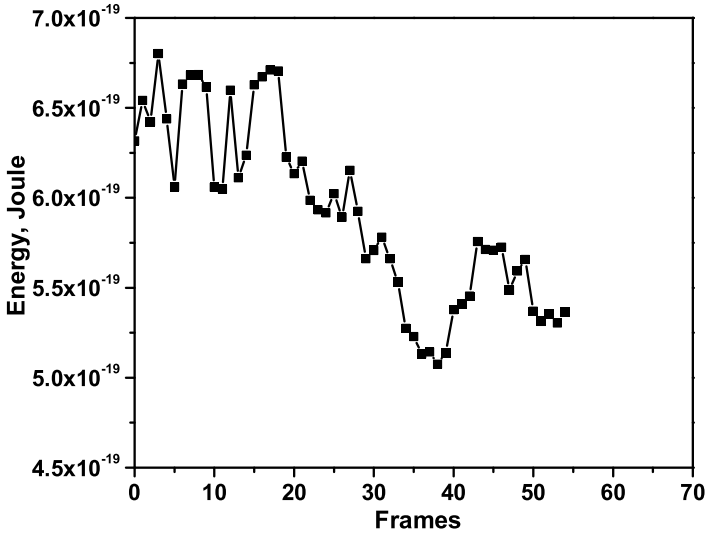

Figure 6.4: The 3D structure of the cluster with 63 particles and one particle leaving from the top.

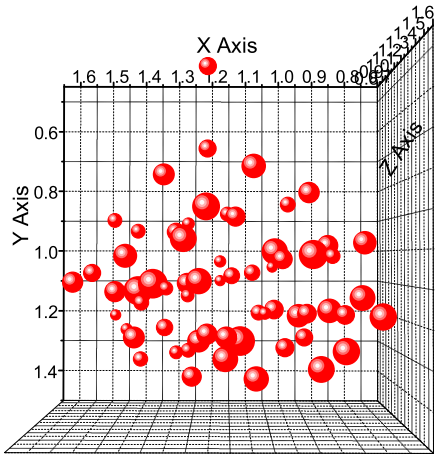

during 100 frames (4 seconds) (see Fig. 6.4).

The whole energy of the cluster has been calculated with respect to the number of bonds using eq. 6.2. Fig. 6.5 shows the average energy during 150 frames (6 sec.) after the particles have left. After the last particle escaped (frame 87), the energy starts to decrease. It is lower than at the beginning of the sequence. After the first two particles escape (frames 28, 63) the energy rapidly increases (peaks at frames 47 and 76) demonstrating an energetically unfavorable state. The stable trend after frame 87 corresponds to the vibrations of the upper particle in the cluster, which however does not evaporate.

The results of numerical simulations of Coulomb clusters [113] show that 57 and 60 are so-called "magic" numbers in 3D configurations. This means, that the system in these states is sufficiently stable and has less energy per bond than it would have with a smaller or a larger number of particles. Even if the interaction between particles in the cluster is not purely Coulomb, we may conclude that our cluster loses particles in order to achieve a "magic" number, i.e. a more stable state with minimum energy. Furthermore, the escape of the particle at the top of the cluster suggests the configuration of an electric field, which is overall weak in the region of the cluster and stronger at the position where particles can jump out. This supports the conception of weak external confinement for our clusters, which has been discussed in chapter 5.

Figure 6.5: The derived energy of the 63 particles' cluster in time.

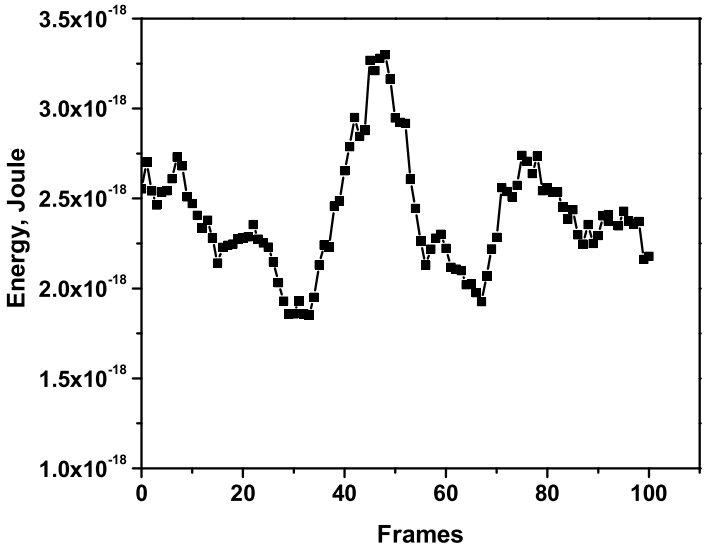

6.4 Analysis of vibrations and dust acoustic waves

After the last particle has left the cluster of 63 particles the remaining upper particle exhibits large amplitude vibrations. An analysis of these vibrations has demonstrated that particles leave during such self-oscillations of the cluster, which are mostly vertical. We have obtained the natural frequency of the system by Fourier transforming the vertical position of the particles. Fig. 6.6 presents several modes of the cluster frequency, f, with important peaks at 1.2, 2,6 and 3.57 Hz.

In [103] Smirnov generally describes the vibrations of such cluster particles as an acoustic wave (with sound speed), which propagates inside the cluster. In order to theoretically model our experimental results with complex plasmas, these oscillations have to be compared to dust acoustic waves. For this kind of wave, the inertia of the particles is very important and electrons and ions obey the Boltzmann distribution. The Poisson equation has been considered together with the dust continuity equation and the dust momentum equation [3]. In the long-wavelength limit, ($k^2\lambda_D^2 \ll 1$, where k=1/D, D being the dimension of the cluster, λ_D the combined Debye length), the wave frequency can be found as:

$$\omega = kZ_{d0}\left(\frac{n_{d0}}{n_{i0}}\right)^{1/2}\left(\frac{k_BT_i}{m_d}\right)^{1/2}\left[1+\frac{T_i}{T_e}\left(1-\frac{Z_{d0}n_{d0}}{n_{i0}}\right)\right]^{-1/2} \tag{6.3}$$

where Z_{d0} is the charge of the particles. For these calculations the problem arises because our cluster is located inside a plasma that has been modified by the presence of the cluster

Figure 6.6: The Fourier transform of the vertical vibrations of the 63 particles' cluster.

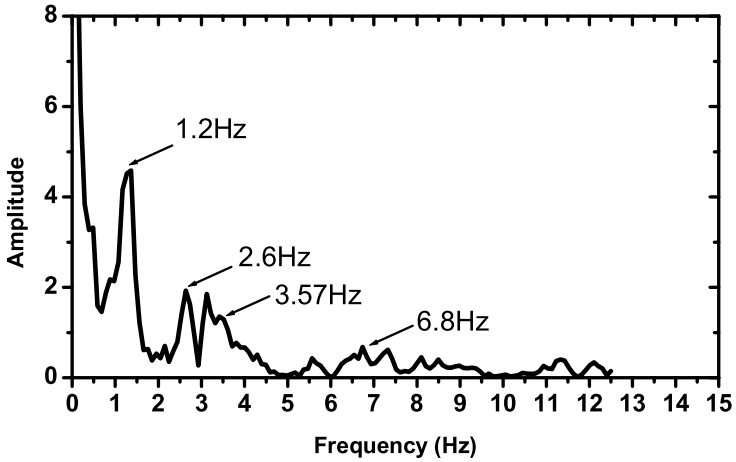

itself, i.e. the plasma near the cluster border differs from the plasma far away. Since electrons and ions are absorbed by the solid spheres a space charge forms near the cluster. Matching the flux of particles in and out the cluster, with zero net current, will create double layers, as in [111]; in that paper for similar conditions the double layer voltage was $1k_BT_e/e$. In our case the effect is reduced by the focusing of the ions near the cluster border due to the spherical shape, as for spherical Langmuir probes. In our slightly collisional regime the radial motion theory for the ion motion gives an upper estimate for the floating potential. For $R/\lambda_D \simeq 1$, the effect of the geometry implies a reduction of 0.33 with respect to the planar geometry in Argon [114]. Thus, we have a difference in the potential between the plasma surrounding the clusters and the plasma "far away" of the order of a fraction of k_BT_e/e. In the follow we take this fraction to be 0.66.

Inside the quasineutral cluster the particles have a charge strongly reduced with respect to the charge calculated using the vacuum approximation and the particle floating potential from the radial theory for electric probes [108]. In our collisionality regime (200 μm the distance between particles and the mean free path is 30 μm) we assume the charge z_d=2500e, somewhat lower than estimated in ref. [112], because of the larger number of particles in the present case. $n_{d0} = 2.35 \times 10^{11} m^{-3}$ is the dust density in our cluster of 63 particles. The plasma density n_{i0}, n_{e0} in "small plasma" volume has been estimated from the spectroscopic analysis to be in the order of $10^{16} m^{-3}$, higher than main plasma density. Ions are considered to have room temperature (T_i=0.025 eV), the temperature of electrons are supposed to be about 3 eV. At these parameters the estimated angular frequency of dust acoustic waves ω is 2.5 Hz. It is in agreement with the first peak of experimental frequency, for which ω =7.5 Hz. The other peaks in the power spectrum

cannot be identified. The Einstein frequency for this system using the above values is about 700 Hz.

6.5 Analysis of vibrations and surface tension

Since our cluster is strongly coupled (liquid phase), a hydrodynamic approach may be also suitable for our situation (although the number of particles is still relatively small). The cluster has the shape of a sphere, therefore the frequency of the system has been compared with the resonance mode frequencies of a liquid drop with surface tension. According to [115] the self-frequency of capillary oscillations of a spherical drop is given by the following equation:

$$\omega^2 = \frac{Tl(l-1)(l+2)}{\rho R^3}, \tag{6.4}$$

where l takes all integral values from zero upwards. Eq. 6.4 vanishes for $l = 0$ and $l = 1$. The value $l = 0$ corresponds to radial oscillations, i.e. to spherically symmetric pulsations of the drop, which we do not observe. For $l = 1$ the motion is simply a translatory motion of the drop. The smallest possible frequency of oscillations of the drop corresponds to $l = 2$ and is given by:

$$\omega_{min} = \sqrt{\frac{8T}{\rho R^3}}. \tag{6.5}$$

where T is surface tension, R=0.4 mm the cluster radius, ρ is the density of the particles in the cluster, $\rho = 63 mass_{part}/Volume_{cluster}$. If we identify this minimum frequency with the first peak in Fig. 6.6 (the frequency f = 1.2 Hz) we obtain for the next frequency modes with l =3, 4 and 6 corresponding higher orders at f=2.6, 3.57 and 6.8 Hz. These are in surprisingly good agreement with the peaks seen in Fig. 6.6.

We can now estimate the surface tension of the cluster from eq. 6.5 by using the first peak of f = 1.2 Hz. The ratio T/R is found to be about $3.3 \cdot 10^{-8} Joule/m^3$. This is the total surface tension of the cluster. This value can be compared with the energy of all bonds in the cluster. From the analysis of shell structure (Fig. 6.2) we see that there are two shells in the cluster of 63 particles: 8 or 10 particles populate the first shell and the other 53 particles the second shell. The number density of bonds between the first and second shell, N, is the ratio of the number of particles in the external shell to the surface area of the cluster, $53/4\pi R^2$. The "equivalent" surface tension is obtained by multiplying N by the energy per single bond, $1/2k\overline{\triangle d}^2$, with $\overline{\triangle d}$ the average value of particle displacement. Equating the derived surface tension with $N \cdot 1/2k\overline{\triangle d}^2$ yields a value of $\overline{\triangle d}$ 18 μm, which matches with the direct measurements of the particle displacement. This is in the range of 10-20 μm with respect to the equilibrium position.

It is of considerable interest to estimate a surface tension for the cluster using classical fluid theory and to compare this with the results obtained above. The spherical clusters can be regarded as liquid drops. The walls experience the pressure from inside and outside, which are compensated by the surface tension $P_1 - P_2 = 2T_{hyd}/R$, T_{hyd} is the surface tension calculated from the hydrodynamics of a drop, P_1 is the pressure inside and P_2 is the pressure outside. The pressure P_2 can then be written simply as the pressure of ions and electrons near the cluster surface, the "Maxwell stress" is null for double layers:

$$P_1 = \frac{2T_{hyd}}{R} + \frac{J_i}{e} M_i v_i + n_e k_B T_e. \tag{6.6}$$

The ion flux, with density J_i, enters the cluster from the quasineutral plasma. This flux is equal to the electron flux and can be calculated as:

$$J_e = n_e \sqrt{\frac{k_B T_e}{2\pi m_e}} e^{-eV_{fl}/k_B T_e}. \tag{6.7}$$

m_e is the electron mass, V_{fl} the floating potential of the cluster, the electron temperature, T_e, is considered to be 3 eV, ions are at room temperature T_i=0.025 eV. The plasma density n_e is approximately $10^{16} m^{-3}$. Using these values and considering collisions the second term in eq. 6.6, $J_i M_i v_i$, has a value of $\simeq 10^{-2} Joule/m^3$. The electron pressure $n_e k T_e$ is much smaller than the ion ram pressure. The pressure P_1 inside the cluster is the sum of ion and electron thermal pressures and the particle pressure due to their electrostatic interactions. The quasineutrality of the cluster implies $n_i = n_e + z_d n_d$; with $n_d = 2.2 \cdot 10^{11} m^{-3}$ and z_d=2500e, as calculated before. The densities of the both free and surface-bond negative charges are $\simeq 5 \cdot 10^{14} m^{-3}$. The particle pressure is $P n_d k T_d$, where P is the coupling parameter. Its value is calculated from the balance of the internal and external pressures to be $P \simeq 400$. The equivalent pressure due to surface tension of our cluster of 63 particles, estimated from the vibration of the cluster as $3.3 \cdot 10^{-8} Joule/m^3$, is much smaller than the other terms. This could be a consequence of the fact that the cluster is small with only a few shells. It is possible that the surface tension increases initially as the drop becomes "more hydrodynamic". More experiments with larger clusters are needed to see whether T varies with cluster size, R.

6.6 Conclusion

The possibility to get 3D plasma clusters under gravity conditions and to obtain the 3 coordinates of the particles simultaneously allowed us to perform the analysis of the cluster structure, as well as the study of wave propagation inside the cluster. In this chapter we

have demonstrated, that the observed reorganization of a 3D plasma cluster is governed by the principle of minimum energy. A cluster formed by 60 particles appears to be stable in accordance with the "magic number" found in the simulation of [113] for Coulomb interaction. The analysis of 63 particles' cluster vibrations using Fast-Fourier transform gave cluster frequencies, which agree well with the theory of dust-acoustic waves. Since this cluster has two shells, we investigated cooperative phenomena, where the cluster was compared to a liquid drop with surface tension. The observed resonances in the Fourier spectrum agree surprisingly well with the resonance mode frequencies of a liquid (up to $l = 6$), suggesting that even small clusters exhibit fluid-like cooperative behavior.

Chapter 7

Microparticles as a diagnostic tool of the electronegative plasma sheath at low pressures

In this chapter a diagnostics of the electronegative plasma sheath at low pressures using microparticles (dust particles) is presented.

Electronegative discharges are often used in plasma processing of materials because they are highly chemically reactive and they show peculiar plasma characteristics, as transport and plasma boundaries, useful for etching and deposition. Amemiya in his work [116] gives several references, where negative ions play an important role: in discharge physics the negative species change the structure of cathode region and the positive column [117], also they influence the light emission and stability of the discharge [118]; in plasma processing negative ions vary the plasma potential and the behavior of electrons. They also cause dislocations on the surface during film formation [119]. Working with electronegative discharge it is necessary to care for the chemical properties of such gases. In electronegative plasmas the processes occurring in the volume are in general not only ionization, but also attachment, detachment and recombination [120].

At present several physical effects of the electronegative sheath are still unexplored. Physically a discontinuity in the electrostatic potential may arise because the colder, usually heavier, negative species is confined in the plasma while the electrons extend further in the sheath. This problem was originally pointed out by [121] and discussed further in a number of theoretical contributions, which included ionization, collisions and different techniques of analytical or numerical analysis, [46], [122]. So far there has been no experimental validation of the theories. The reason lies in the difficulty of mid-sheath diagnostics under the conditions of significant negative ion density and high temperature ratio.

In the work presented dust particles were injected into plasma. They levitate in the

sheath region, gravity being compensated mainly by the upward electrostatic force. The grain size usually is very small, therefore, the plasma is perturbed only in the immediate vicinity of the microparticles. Thus, the injected dust particles provide a new experimental approach for sheath diagnostics. The equilibrium position depends on the presence of negative ions in two ways: the electric field of the sheath can be a nonmonotonic function of the electronegativity, and the particle charge is strongly affected by the modified Bohm flux of positive ions.

A collisionless model of the levitation force as a function of α, the ratio of the negative ions to the electron density is presented. This ratio is measured in the collisionless range by Langmuir probe and extrapolated to the collisional regime using the trend obtained by photo detachment techniques [123]. The correspondence between the temperature of the negative ions and the observed double equilibrium position (due to the stratified plasma), which has been predicted by [122], is investigated.

7.1 Features of electronegative plasmas

Electronegative plasma is usually defined as a plasma, where the density of negative ions is significant and must be taken into account. But to determine the proportion of negative ions is not a simple problem. Franklin in [124] presents the following estimate of the plasma electronegativity: the electronegativity parameter $\alpha \equiv n_-/n_e$, where n_- is the negative ion density and n_e is the electron density, must be >3 at low pressures, and >300 at higher pressures.

The presence of negative ions can significantly alter the discharge structure. In [125] the authors give the conditions, under which it is permissible to use the Boltzmann relation in electronegative plasmas. At very low collisionalities, *i.e.* negative ion mean free path greater than plasma dimension, $\lambda_- > L$, the negative ions have a Boltzmann distribution with temperature T_-, *i.e.* $n_- = n_{-0}\exp(eV/k_BT_-)$.

At higher collisionality, when the ion motion is collisional within the plasma, the electronegativity parameter $\alpha \approx 300$ and it is approximately constant across the plasma. But in this situation the Boltzmann relation is not applicable, because the Bolzmann relations for electrons and negative ions ($n_e = n_{e0}\exp(eV/k_BT_e)$, $n_- = n_{-0}\exp(eV/k_BT_-)$) at the condition $n_- = \alpha n_e$ cannot be satisfied simultaneously, unless the temperatures of electrons and negative ions are equal, $T_- = T_e$. However, in general, $T_- \sim 0.01T_e$. Thus, the Boltzmann relation can hold for the electronegative ions only in the case of very low collisionality.

In the work of Braithwaite and Allen [121] the authors have pointed out that in the presence of negative ions the equation for potential at the sheath edge can have a multi-

Figure 7.1: Plot from the paper of Braithwaite and Allen [121] of normalized sheath edge potential against the plasma electronegativity $\alpha \equiv n_-/n_e$.

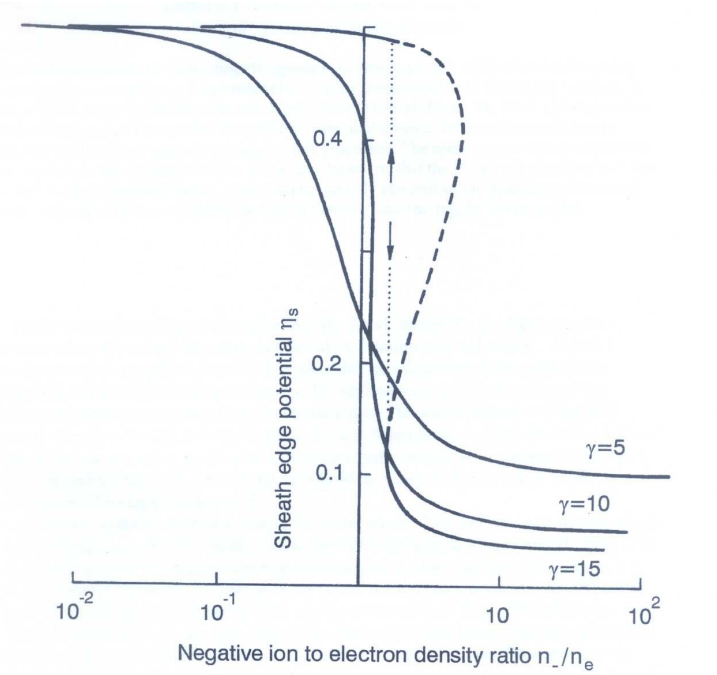

valued solution. In electropositive plasma this potential is described by the Bohm criterion (chapter 1):

$$eV_s \geq \frac{1}{2} k_B T_e. \tag{7.1}$$

However, in electronegative discharges Braithwaite and Allen found out that for certain values of the plasma parameters this criterion can be modified. In particular, they have estimated the values of electron and negative ion temperature ratio $\gamma = T_e/T_-$, at which the Bohm criterion is multi-valued. When $\gamma \geq 5 + \sqrt{24}$ ($\gamma \geq 9.9$) and at certain values of plasma electronegativity, a double layer can develop. In Fig. 7.1 the normalized sheath boundary potential $\eta_s = V_s/k_B T_e/e$ is presented with respect to the plasma electronegativity α. It is clear that at large γ a certain range of electronegativity yields solutions at several values of the potential. It has been proposed to take the smallest value as the correct one, because it is the first plasma edge encountered by the ions, when they exit the plasma. As soon as the gradient of the potential is reached, the quasi-neutrality fails and the space charge sheath forms.

This multi-valued solution for the sheath potential may imply the presence of a multi-layer at the plasma boundary, *i.e.* two plasmas are separated by a potential structure. The multi-layer (double or triple layer) has been discussed in several theoretical works ([126],

[127], [128]). Such a structure in the vicinity of the plasma sheath depends on the value of the plasma electronegativity and also on the collisionality. In the paper of Sheridan [122] the effect of moderate collisionality in an electronegative discharge is modelled. First of all, the discharge structure is described with increasing the negative ion concentration in the collisionless case. When the electronegativity, α, is small, negative ions are confined in the center of the discharge and most of the plasma region is electropositive. Consequently, the Bohm velocity at the plasma edge is determined mostly by the electron temperature. This is the so-called "stratified" discharge. When α is large, the Bohm velocity at the sheath edge is determined by the negative ion temperature, the electron density is almost constant in the plasma and positive and negative ion densities go together closely up to the plasma edge. It is the "uniform" structure. In a third situation, when $\gamma \geq 9.9$, *i.e.* there exist two solutions for the plasma edge potential [121], a double-layer structure is found between the stratified and the uniform cases.

In the case of collisional discharge the amount of collisionality defines the structure. When collisionality is small, the discharge is uniform. For a high degree of collisionality the discharge stratifies, and again, between the uniform and stratified discharge there is a double-layer structure. Thus, increasing collisionality in a collisional model is similar to decreasing α in the collisionless case: one moves from a uniform structure to a double-layer discharge and then to a stratified discharge.

Hence, theory predicts that the electronegative discharge has a complex structure, which depends on all the plasma parameters. From another point of view, it is important to study this kind of discharges, because of its wide practical use.

In this chapter we discuss the use of levitated dust particles as a new powerful diagnostic of the mid-plasma sheath. These particles can reveal features undetectable either to plasma or to surface measurements. The equilibrium positions of microparticles suspended in an Oxygen plasma-sheath together with a model of the levitation force and Langmuir probe measurements in the bulk give evidence of secondary electropositive plasmas down in the already established plasma sheath, in the range of parameters, where the modified Bohm criterion breaks down in multiple solutions.

7.2 Experimental evidence

The experiments have been performed in the metallic chamber (see chapter 2). Melamine-formaldehyde particles of diameters 6.81, 3.42 and 1.29 μm were injected into the plasma through a fine mesh from a dispenser at the side edge of the plasma. A confining external ring has been situated on the lower electrode in order to confine particles just above the electrode and do not let them escape to the chamber sides. As mentioned before, the main

Figure 7.2: Particles of 3.42 μm diameter about a minute after the injection in the plasma. P=46 Pa and electrode excitation V_{RFpp}=300 V. The picture shows 17×13 mm.

aim of this work is to study the electronegative sheath, unperturbed by the presence of many particles. To do this equilibrium positions of single (or few) particles have to be determined for different conditions (power, pressure). The results can be summarized as follows: the particles with diameter 6,81 μm had one stable position for pressure in the range $4.7 < P < 17$ Pa and for $P > 70$ Pa. In the intermediate range the particles had two metastable equilibrium positions, the lower being more stable (a few minutes residence time) than the upper (residence time of the order of tens of seconds). From 1.4 to 4.7 Pa the particles acquired a large kinetic energy and no particles could levitate below 1.7 Pa. The particles with diameter 3.42 μm show the same behavior as the larger ones, and, within the experimental error, the same positions. A typical picture of non-interacting particles is shown in Fig. 7.2. The particles with diameter 1.29 μm always had two equilibrium positions with the same trend with respect to pressure, as the upper layer of the heavier ones. For the analysis it is important to only consider those particles in the lower layer, which are not interacting with particles in the upper layer (i.e. a particle not directly below another one, or in the middle point between particles in the upper layer, or showing any other correlation). The position of the particles is shown in Fig. 7.3.

When a particle has reached its equilibrium position, the sum of all the forces acting on it is zero. It is assumed that only two dominant forces are acting on the particle in the plasma sheath: an upward electric force $F = QE$ and gravity downwards. This means that a model for the plane electrode sheath in electronegative discharges and a model for the charging of the particle in that sheath are needed. Since the injected particles are small spheres, the model for the charging should be in spherical geometry.

Figure 7.3: The particle positions above the lower electrode versus pressure.

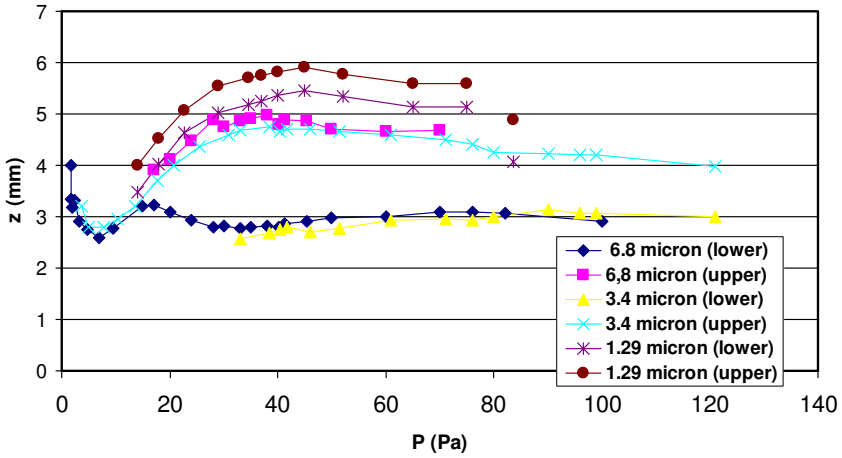

7.3 Modification of Bohm criterion in electronegative plasma

In the planar sheath of an electronegative plasma the positive ions enter with an energy given by the modified Bohm criterion, as derived by Braithwaite and Allen [121]. The potential at the sheath edge is:

$$\eta_s = \frac{1}{2}\frac{1+\alpha_s}{1+\gamma\alpha_s}, \tag{7.2}$$

where $\alpha_s = n_{-s}/n_{es}$ and $\eta_s = eV_0/k_BT_e$ are the plasma electronegativity and the dimensionless potential at the sheath edge, respectively. From this equation the dependence of the electronegativity parameter, α, from the potential at the sheath edge can be extracted. Since in the work presented the dependence of the electronegativity parameter from other plasma parameters will be studied, the derivation of the η_s is the important part of the work and it will be discussed in detail.

There are three ways to derive the potential at the plasma edge. The first way is based on the assumption that at the sheath edge the derivative of the charge density with respect to the potential is zero [121]:

$$\frac{d\rho}{dV} = 0, \tag{7.3}$$

where ρ is the net space charge, $\rho = e(n_{is} - n_{es} - n_{-s})$, where the subscript s refers to the sheath edge, the subscripts i, e and $-$ to ions, electrons and negative ions, respectively. V is the potential measured from the sheath edge. It is assumed that the electron velocity distribution is Maxwellian, thus, the electron density n_e can be described by the Boltzmann

relation. The same is assumed for negative ion density n_-:

$$n_e = n_{es} \exp(ev/k_B T_e), \tag{7.4}$$

$$n_- = n_{-s} \exp(ev/k_B T_-). \tag{7.5}$$

For the positive ion density the assumption of the flux conservation at the plasma-sheath edge is used:

$$n_i v_i = n_{is} v_{is}. \tag{7.6}$$

Thus, the ion density is [33]:

$$n_i = n_{is} \left(1 - \frac{V}{V_0}\right)^{-1/2}, \tag{7.7}$$

where V_0 is the potential at the sheath edge.

The quasineutrality condition is assumed to be still applicable at the plasma-sheath edge:

$$n_{is} = n_{es} + n_{-s}, \tag{7.8}$$

Now, the Poisson equation is considered:

$$\varepsilon_0 \bigtriangledown^2 v = -\rho. \tag{7.9}$$

After the above determinations of the densities this equation can be written as follows:

$$\varepsilon_0 \frac{dV^2}{dx^2} = -n_{is} e \left(1 - \frac{V}{V_0}\right)^{-1/2} + n_{es} e \exp(ev/k_B T_e) + n_{-s} e \exp(ev/k_B T_-), \tag{7.10}$$

where the first term presents the positive ion density, the second and third terms are the electron and negative ion densities, respectively.

In order to find the potential at the plasma-sheath edge V_0 the potential in the sheath is assumed to be equal to zero, $V = 0$. From the Poisson equation the following inequality can be obtained, since the squared second derivative of the potential can be only positive:

$$\frac{eV_0}{k_B T_e} \geq \frac{1}{2} \frac{1 + \frac{n_{-s}}{n_{es}}}{1 + \frac{T_e}{T_-} \frac{n_{-s}}{n_{es}}}. \tag{7.11}$$

If the dimensionless variables α_s, γ and η_s, which have already been introduced above, are used, the same expression for the potential at the sheath edge as has been derived in [121] is obtained:

$$\eta_s \geq \frac{1}{2} \frac{1 + \alpha_s}{1 + \gamma \alpha_s}. \tag{7.12}$$

The second way to get the Bohm criterion has been described in [33]. The quasineutrality condition (eq. 7.8) together with the same determination of densities for electrons, negative and positive ions as before (eqs. 7.4, 7.5, 7.7) is applied. Then the Poisson equation reads:

$$\varepsilon_0 \frac{dV^2}{dx^2} = -n_{is} e \left(1 - \frac{V}{V_0}\right)^{-1/2} + n_{es} e \exp(ev/k_B T_e) + n_{-s} e \exp(ev/k_B T_-). \tag{7.13}$$

Multiplication by dV/dx and integration with respect to x gives:

$$\frac{1}{2}\varepsilon_0 \frac{dV}{dx}^2 = n_{is} 2eV_0 \left(1 - \frac{V}{V_0}\right)^{1/2} + n_{es} k_B T_e \exp(ev/k_B T_e) + n_{-s} k_B T_- \exp(ev/k_B T_-) + C \tag{7.14}$$

The constant C can be found by assuming the electric field at the sheath edge to be negligibly small:

$$2n_{is} eV_0 \left(1 - \frac{V}{V_0}\right)^{1/2} + n_{es} k_B T_e \exp(ev/k_B T_e) + n_{-s} k_B T_- \exp(ev/k_B T_-) - \frac{1}{2}\varepsilon_0 E^2 = \\ = 2n_{is} eV_0 + n_{es} k_B T_e + n_{-s} k_B T_- \tag{7.15}$$

The first term of the left hand side represents the rate of momentum flow nmv^2, and the next two terms represent the electron and negative ion pressure. This equation, as shown in [33], is the so-called *stress-balance equation*.

Then the case of small potentials, V, is considered, and all terms with V are expanded into series. The zeroth and first order terms cancel out. As in the previous case the following inequality is then obtained:

$$\frac{n_{es}}{k_B T_e} + \frac{n_-}{k_B T_-} \geq \frac{n_{is}}{2eV_0} \tag{7.16}$$

Finally, applying the quasineutrality condition (7.8) the modified Bohm criterion for an electronegative plasma is:

$$\eta_s \geq \frac{1}{2}\frac{1+\alpha_s}{1+\gamma\alpha_s} \tag{7.17}$$

The third way to get the potential at the sheath edge is described in [129] and it is based on the assumption that the sound speed of ion-acoustic waves is equal to the speed of ions at the sheath boundary. These calculations will be not considered in detail.

In eq. 7.17 the value of the plasma electronegativity at the sheath edge α_s is used,

Figure 7.4: The multivaluated solution for the sheath edge potential. γ=10 and α_0=0.55.

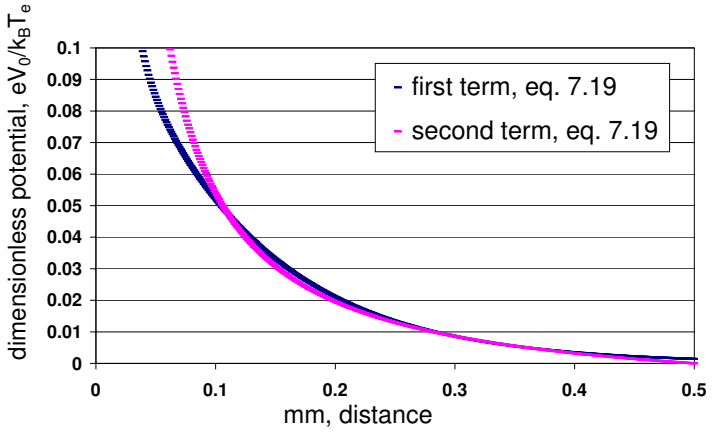

which depends on the electronegativity in the main plasma α_0 in the following way:

$$\alpha_s = \alpha_0 e^{-\eta_s(\gamma-1)} \tag{7.18}$$

Thus, the Bohm criterion in the terms of α_0 becomes

$$\alpha_0 exp[-\eta_s(\gamma-1)] = (1-2\eta_s)/(2\gamma\eta_s - 1). \tag{7.19}$$

This equation has been solved graphically and results are presented in the Fig. 7.4. This figure shows the dependence of the first and second term of this equation with respect to α_0. One can see that two solutions exist in the regions of $\eta_s \approx 0.1$ and 0.35.

In the table 7.1 we have summarized the values of α_s and η_s for a given value of α_0 (for γ=10).

α_0	η_s	α_s
0.01	0.5	$1.11 \cdot 10^{-4}$
0.1	0.5	$1.11 \cdot 10^{-4}$
1	0.41	0.025
10	0.058	5.933
20	0.052	12.525
50	0.051	62.625

Table 7.1: The values of α_s and η_s at certain value of α_0 at γ=10.

The smaller solution for the sheath edge potential, which corresponds to the first plasma

edge encountered by the ions arriving from the plasma, has been chosen in the present work.

7.4 Calculation of electric field

By using the conservation of ion flux (eq. 7.7) the Boltzmann distribution for electrons and negative ions (eqs. 7.4, 7.5) and quasi-neutrality condition in electronegative plasma (eq. 7.8) the Poisson equation can be written as follows:

$$\epsilon_0 \frac{d^2\eta}{d\xi^2} = -n_{es}[(1+\alpha_s)(1-\frac{\eta}{\eta_s})^{-\frac{1}{2}} - e^{\eta} - \alpha_s e^{\gamma\eta})] \tag{7.20}$$

with $\xi = r/\lambda_D$ - the normalized space coordinate with respect to the plasma edge. This equation is integrated analytically to obtain the electric field with the boundary conditions of zero field at the sheath edge:

$$\left(\frac{d\eta}{d\xi}\right)^2 = \frac{(1+\alpha)^2}{1+\alpha\gamma}\left\{\left[1-2\eta\frac{(1+\alpha)^{1/2}}{1+\alpha}\right]-1\right\} + \{e^{\eta}-1\} + \frac{\alpha}{\gamma}\{e^{\eta\gamma}-1\}. \tag{7.21}$$

The second integration is numerical and gives us the space distribution of potential $\eta(r)$. During calculations the boundary condition of η_s=0.01 at the sheath edge has been used to avoid divergences.

In Fig. 7.5 and Fig. 7.6 the distribution of dimensionless potential and dimensionless field at different value of α_0 are shown as a function of ξ for different values of plasma electronegativity α. From these two plots one can see the irregularity in the distribution with increasing α.

7.5 Charge calculation

When the particle is much smaller than the electron Debye length, the space charge just near its surface is ignorable with respect to the charge at the surface. In this case the vacuum approximation for the potential is valid and the charge acquired by a particle of fixed radius is directly proportional to the floating potential, η_{DC}, measured with respect to the local space potential, η_0:

$$Q = 4\pi a \varepsilon_0 \eta_{DC}, \tag{7.22}$$

where a is the particle radius. For the charge calculation it is assumed that the charge reaches an equilibrium value, when the current of electrons, positive and negative ions balances, satisfying the equality $I_i = I_e + I_-$. For the charge calculation the Orbital Motion Limited Theory for spherical probe is usually used, because the dust particles have a very small radius compared with the Debye length ($a = 1.7 \cdot 10^{-6}$ m and $\lambda_D \sim 10^{-3}$ m).

Figure 7.5: Distribution of dimensionless potential η at different value of α_0 with respect to position ξ.

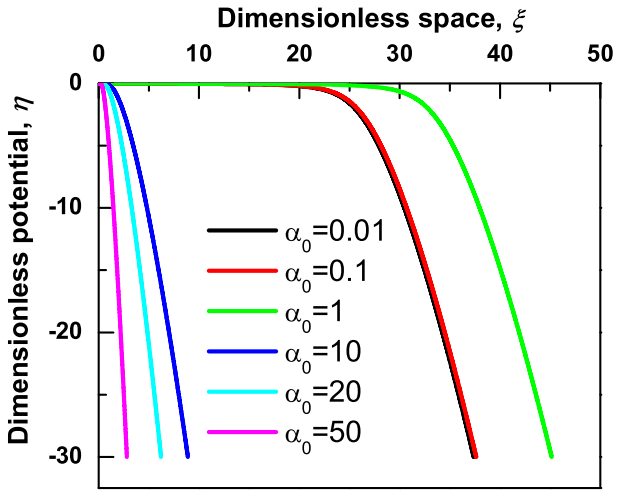

Figure 7.6: Distribution of dimensionless field $d\eta/d\xi$ at different value of α_0 with respect to position ξ.

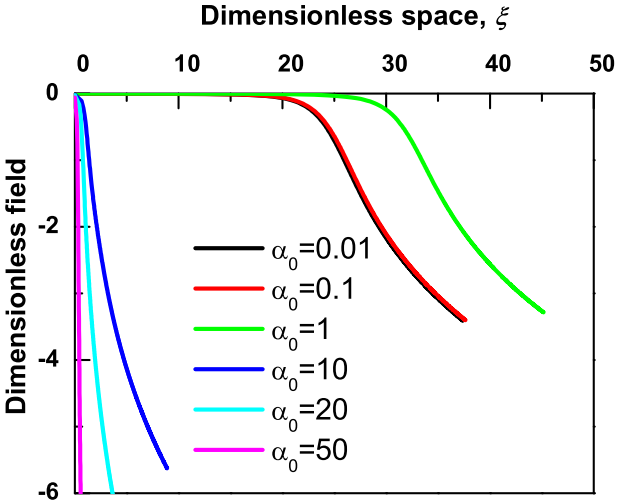

Figure 7.7: The floating potential of particles η_{DC} with respect to the space potential η_0 at different values of α_0 at $\gamma = 10$.

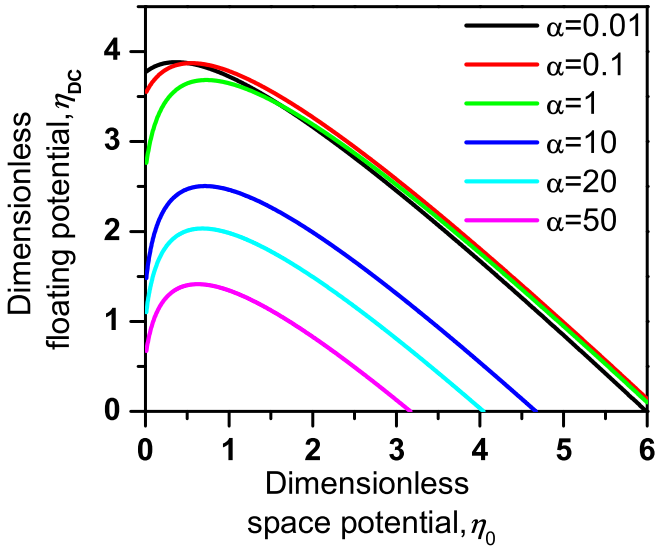

η_{DC} has been calculated from the equation of the current balance:

$$(1+\alpha_s)|\eta_s|^{1/2}\left(1+\frac{\eta_{DC}}{\eta_s+\eta_0}\right) = 2\left(\frac{m_i}{\pi m_e}\right)^{1/2} e^{\eta_0} e^{\eta_{DC}} + 2\alpha\left(\frac{m_i}{\pi\gamma m_-}\right)^{1/2} e^{\eta_0\gamma} e^{\eta_{DC}\gamma}, \quad (7.23)$$

where the left hand side term comes from orbital theory and has been modified to take into account the directed motion of the flux of ions out of the electronegative plasma. From this equation the floating potential of particles η_{DC} as a function of the space potential η_0 can be obtained for given values of α_0. These dependencies at $\gamma = 10$ and $\gamma = 20$ are shown on Fig. 7.7 and Fig. 7.8. From these plots one can see that with increasing α_0 the floating potential decreases. The dependence on γ is negligible at small values of α_0, but it is significant if $\alpha_0 > 1$.

The value of γ is defined by the negative ion temperature and can be changed from 5 up to 100. At this point it has been assumed that the negative ions can be confined by electric field and get some value of energy. Thus, they are not so cold as positive ions. But they also cannot move so much as electrons, because of the large mass.

Figure 7.8: The floating potential of particles η_{DC} with respect to the space potential η_0 at different values of α_0 at $\gamma = 20$.

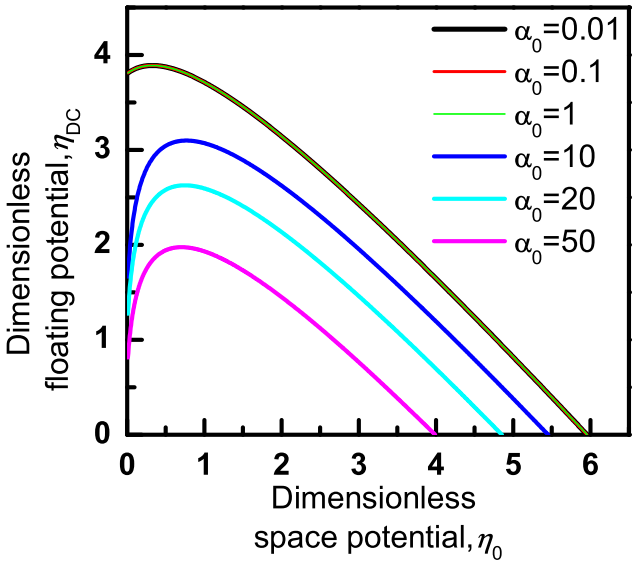

7.6 Levitation force

From these two previous models of the charge and electric field calculations the levitation force $F = QE$ for the particles can be obtained for given gas, particle radius, and electron temperature. This force is estimated from the dimensionless equation:

$$F(\xi) = \frac{d\eta}{d\xi} 4\pi\varepsilon_0 \xi_{part} + \eta_{DC}, \tag{7.24}$$

where $\xi_{part} = a/\lambda_D$. By choosing the plasma parameters the spatial units can be specified in mm (Fig. 7.9). λ_D is obtained as a function of α. Therefore, for a constant ion density the dependence $\lambda_{De}(\alpha) = \lambda_{De}\sqrt{1+\alpha}$ should be made. The curves of levitation force are plotted as a function of position x, with the abscissa going from the floating electrode (V_{fl}=0) upwards, (Fig. 7.10). The intercept with the gravitational force mg gives the equilibrium positions plotted in Fig. 7.11. In this way it is possible to make a direct link to the experiments, if α_0 is known.

7.7 The measurements of α with electric probes

Electric probe measurements have been performed to characterize electronegative discharges. In Fig. 7.12 probe characteristics in Oxygen at three pressures 14, 27 and 72 Pa

Figure 7.9: Theoretically calculated levitation force of the 3.4 μm radius and $\gamma = 10$ versus the height above the electrode.

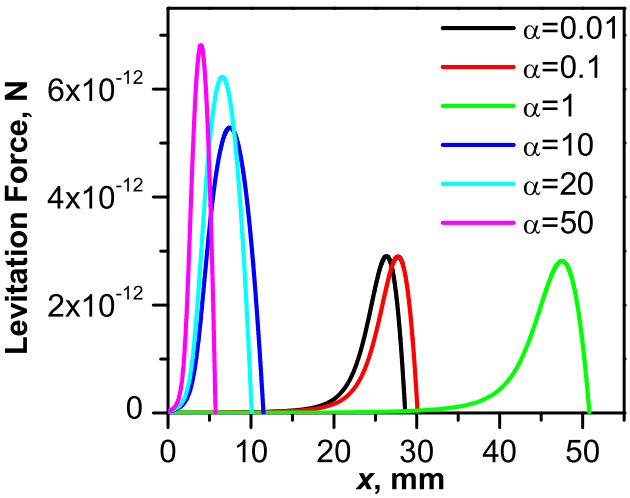

Figure 7.10: Theoretically calculated levitation force of the 3.4 μm radius and $\gamma = 10$ versus the height above the electrode. The zero of the abscissa corresponds to the floating condition. The weight of particle is also shown.

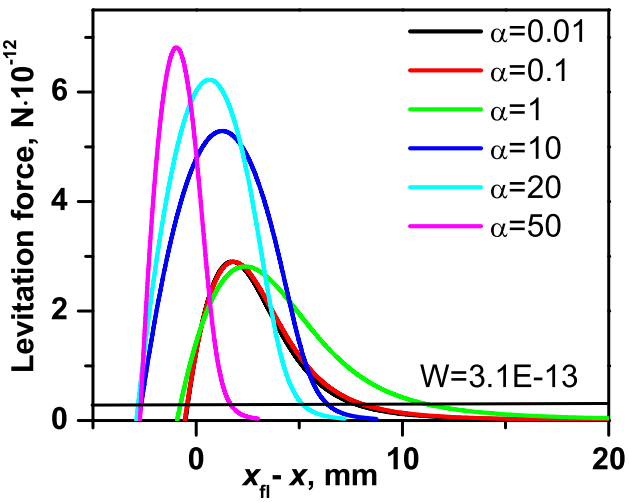

Figure 7.11: The theoretically calculated height of the equilibrium position for the 3.4 μm particles and $\gamma = 10$ in an Oxygen plasma.

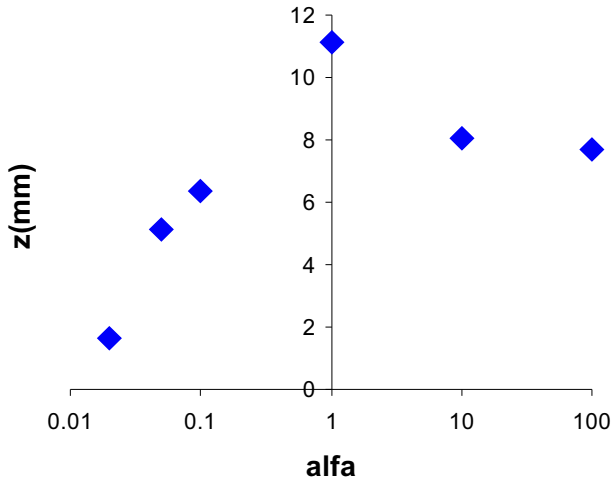

are shown. From this figure one can see that at decreasing pressures ion current increases and electron current decreases. In the case of Oxygen, when ion current increases with respect to the electron current, there are more negative ions. Thus, one can say that the plasma electronegativity increases with decreasing pressure. For comparison the probe characteristic in Argon at 30 Pa is given in Fig. 7.13. In this case there are no negative ions.

The probe has been placed in different positions above the lower electrode to measure the space distribution of negative ions. In Fig. 7.14 one can see that at the same pressure in the middle position the ion current is larger, than in a lower position, while the electron current does not change much.

There are several ways to get the density of negative ions in the electronegative discharge. Amemiya, Annaratone and Allen in [130] have calculated the curves for the ion current in radial motion and orbital motion in cylindrical and spherical geometry. For this purpose the Poisson equation with three components has been solved. The plasma solution has been used as a boundary condition for the sheath solution. The authors have suggested a diagnostic method to determine plasma parameters by applying their theory. If electronegativity α is unknown, under the condition that T_e and T_- are known, the best fitted pair of (α, ξ_p), where ξ_p is the ratio of probe radius to the Debye length, may be obtained from the comparison of the current-voltage characteristics in the paper and from individual experiment. For Maxwellian distributions, the negative charge current at V_p

Figure 7.12: The current-voltage characteristics at the pressures of 14, 27 and 72 Pa (Oxygen).

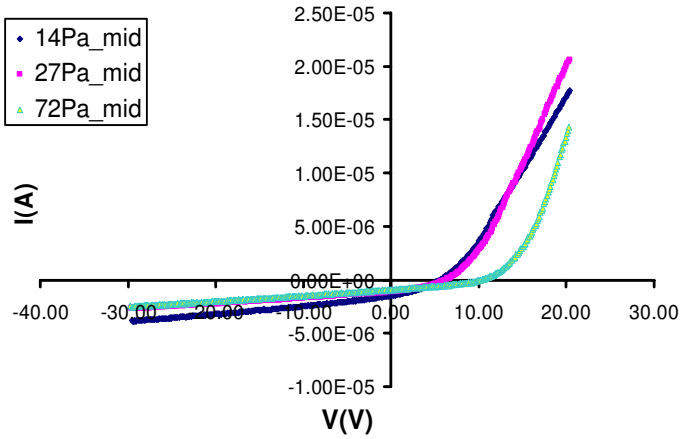

(space potential) is given by the sum of electron and negative ion currents as:

$$I_e = en_0 S \left\{ (1-\alpha)\sqrt{\frac{k_B T_e}{2\pi m}} + \alpha\sqrt{\frac{k_B T_-}{2\pi M_-}} \right\}, \tag{7.25}$$

where all parameters have their usual meaning, and n_0 is a plasma density. If the combination of α and n_0 is substituted into this equation and the procedure is repeated until a good agreement for I_i and I_e is reached, α and n_0 are obtained.

In our case the relative value of the negative ion density to the electron density, α,

Figure 7.13: The current-voltage characteristics at the pressures of 30 Pa in Argon.

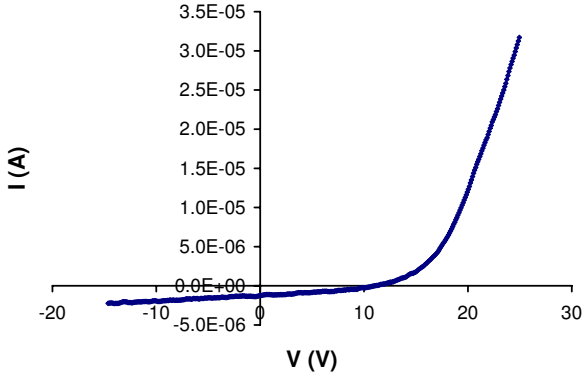

Figure 7.14: The current-voltage characteristics at the different positions of the probe above the lower electrode, 72 Pa (Oxygen).

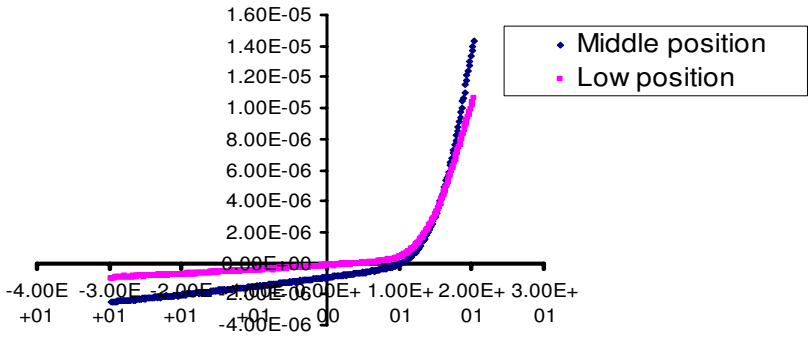

has been deduced from Langmuir probe characteristics using the ratio of two peaks on the second derivative (Fig. 7.15).

One peak is due to electrons and another one shows the presence of negative ions. These two peaks are clearly identifiable only for pressures below 20 Pa. To obtain the plasma electronegativity the following equation has been used:

$$\alpha = \sqrt{\frac{M_-}{m_e}} \frac{\int_{-\infty}^{V_p} \sqrt{|V - V_p|} I''_-(V - V_p) dV}{\int_{-\infty}^{V_p} \sqrt{|V - V_p|} I''_e(V - V_p) dV}, \tag{7.26}$$

where I'' is the second derivative of the current-voltage characteristics. This method is sensitive to a possible instrumental effect, which produces a broadening of the second derivative of the curves if this broadening does not conserve the area. However, it has been chosen for the positive ion analysis [130] because it is independent of the estimated values of γ and the hypothesis of Maxwellian distribution for the electrons. In fact, the eedf (electron energy distribution function) has been found strongly depleted in the low energy range. The above equation can only be used for pressures up to 20 Pa. At higher pressures the second derivative of the current was dominated by electrons/positive ions at low energies so that the negative ion distribution could not be clearly identified. Fig. 7.16 shows the measured values of α. The curve has been extended above 20 Pa using the theoretical trend of n_- from [123] and our experimental values for n_e. In Fig. 7.3 one can see that the position of the upper layer of particles has a maximum at $P \approx$45 Pa for all the diameters. At this pressure Fig. 7.16 shows $\alpha \approx 2$ in the center of the discharge, which agrees well with the maximum position shown in Fig. 7.11. In this maximum position the suspended particles experience an ion flow that comes directly from the main plasma, and is not much affected by collisions or by the multiple solution "instability", which develops

Figure 7.15: The second derivative of probe current at P=5.6 Pa. The two peaks shape is caused by the presence of negative ions.

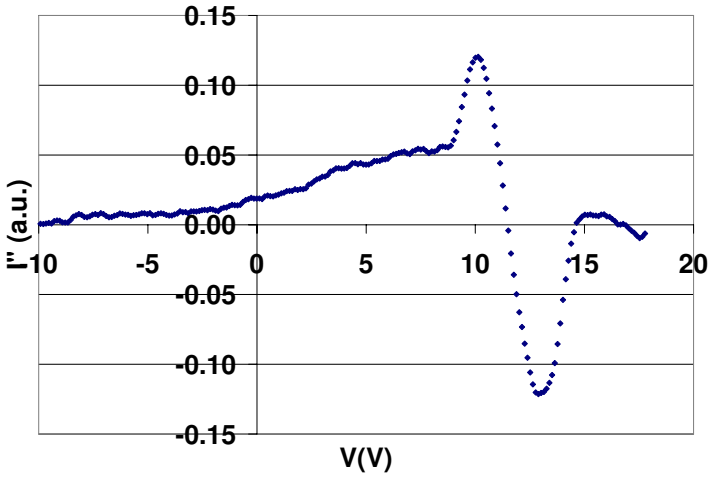

for values around $\alpha = 1.17$ at $\gamma = 10$.

7.8 The temperature of negative ions

For the comparison of the results of our model with experiments both the density of negative ions and their temperature should be known. Here it is necessary to refer to the chemistry of the plasma processes. In the plasma bulk the dominant negative ions are O^-, but O_2^- and O_3^- also make a significant friction (about 10%) [123]. The O^- ions can be created by the dissociative attachment of an electron to molecules O_2 and $O_2(a)$. The latter is a metastable state. The energy of the negative ion produced by dissociative attachment of an electron to a molecule can be written following [131] as:

$$\varepsilon_0 = \frac{1}{2}(\varepsilon - D + \varepsilon_A), \tag{7.27}$$

where the factor $\frac{1}{2}$ arises because the products of the dissociative attachment have the same mass. ε is the electron energy (about 3 eV in our case), ε_A is the electron affinity energy of atomic O^-, which is 1.46 eV [131]. D is the dissociation energy of the molecule. For O_2 it is 4.6 eV and for $O_2(a)$ D is 3.6 eV [132] ($O_2(a)$ is 0.99 eV above the ground state). This means that in dissociative attachment to O_2 negative ions do not get much energy, but in the attachment to $O_2(a)$ the energy acquired is 0.4 eV. The negative ions do not acquire or lose much energy by collisions and remain distinct until they are destroyed by a detaching mechanism. The density of the negative ions is estimated multiplying the

Figure 7.16: The experimentally measured value of α versus pressure. Up to 20 Pa the data are obtained by eq. 7.26 (Ratio Areas) or by conventional probe techniques (Positive Ions Analysis)in the middle of the discharge (Mid) or just above the lower plasma sheath (Low). The lines shows the ratio between the theoretically calculated trend of n_- and the experimentally measured value of n_e.

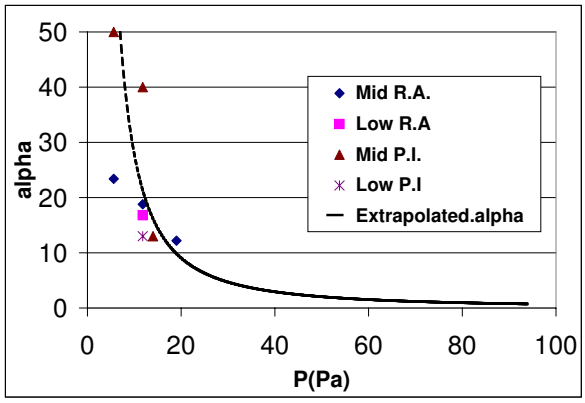

P(Pa)	n_{O_2}	n_e	$n_{O_2(a)}$	n_{O^-}
10	$2.6 \cdot 10^{21}$	$1 \cdot 10^{14}*$	$2 \cdot 10^{20}\triangle$	$1 \cdot 10^{15}*$
100	$1.7 \cdot 10^{22}$	$2 \cdot 10^{14}*$	$9.8 \cdot 10^{21}+$	$2 \cdot 10^{14}+$

Table 7.2: The values of the densities at different pressures in (m^{-3}); * experimentally measured in our apparatus; $\triangle$ from [123]; the + value has been extrapolated as in [123].

production rate of negative ions by the life time. The ratio between the quantity of negative ions created by two reactions:

$$O_2 + e \rightarrow O^- + O \tag{7.28}$$

and

$$O_2(a) + e \rightarrow O^- + O \tag{7.29}$$

has been calculated for two pressures with the coefficient given in [123] and the results are listed in Table 7.2.

This ratio is ≈ 4 at both the pressures. The life time is related to the detachment mechanism and is dependent on the energy of the ions. The cold negative ions are destroyed mainly by reactions $O^- + O_2(a) = O_3 + e$ and $O^- + O_2(a) = O + O_2^-$ [123], while the ions with the energy 0.4 eV are destroyed only by the latter reaction because the rate constant of reaction $O^- + O_2(a) = O_3 + e$ decreases rapidly with the energy [133]. The ratio of the life times is ≈ 0.25 and is independent on the pressure in our range of interest.

Then, the plasma can be characterized as composed by three negative species: the electrons, the cold negative ions, and the fast negative ions, with α_c, α_f and γ_c, γ_f the normalized densities and temperatures. From the above considerations it is known that $\alpha_c/\alpha_f = 1$ for both pressures. The ratios $n_e : n_-^c : n_-^f$ is $1 :\approx 5 :\approx 5$ at 10 Pa. This result is in agreement with the Langmuir probe measurement for α_{total}. The ratios $1 :\approx 0.5 :\approx 0.5$ would match α_{total} at 100 Pa if the density of $O_2(a)$ is fitted as in Table 7.2. This density is compatible with the estimated quadratic dependence on the pressure as in [123]. In this condition the modified Bohm criterion can be re-written as:

$$\eta_s = \frac{1}{2}\left(\frac{1+\alpha_s^c+\alpha_s^f}{1+\gamma^c\alpha_s^c+\gamma^f\alpha_s^f}\right). \tag{7.30}$$

This represents the energy of the positive ions at the sheath edge as well as a distribution of potential in the plasma bulk. The negative ions created at the periphery of the plasma are accelerated towards the center by a potential $\leq \eta_s k_B T_e/e$ and this may lead to a spread in the energy in the core of the discharge as seen by the simulation of Chabert [134]. This effect is small, if $\alpha_c/\alpha_f = 1$ and $\gamma_c = 100$ and $\gamma_f = 10$. Multiple solutions appear only for α_{total} between 0.3 and 0.4. For higher electronegativity η_s is lower than 0.03 so that the presence of two distributions of negative ions effectively mono-energetic can be assume. The results reported in Fig. 7.3 can be interpreted in the light of the three negative species being retarded in different layers. At an intermediate pressure, e.g., 40 Pa, the small particles settle at the edge of the inner plasma, where the cold ions are retarded as well as at the edge of a secondary electronegative plasma, where the fast negative ions are retarded. It can be proposed that a charge double layer develops between the two plasmas with a potential difference of the order of 0.4 V. Finer calculation would go along the lines outlined by [135], who obtained double layers in an electronegative plasma sheath, when an electron beam was injected from the cathode (here from the secondary plasma). The thickness of the secondary plasma is independent of pressure and the temperature and density ratios of the two negative ions species. The medium and large particle settle on the two sides of an electropositive secondary plasma, whose thickness develops with decreasing α_{total} and goes through a maximum in the region of instability. In fact for $\alpha_c/\alpha_f = 1$, an equivalent $\gamma_{total} = 55$ has been calculated for which multiple solutions for eq. 7.20 exist in the range $2 \leq \alpha_{total} \leq 4$. From probe measurement at 20 Pa α_{total}=8 in the center of the discharge but has a lower value in the plasma in front of the lower electrode [120].

Figure 7.17: Time-averaged profiles of electron, positive and negative ions densities at P=6.6 and 39.5 Pa.

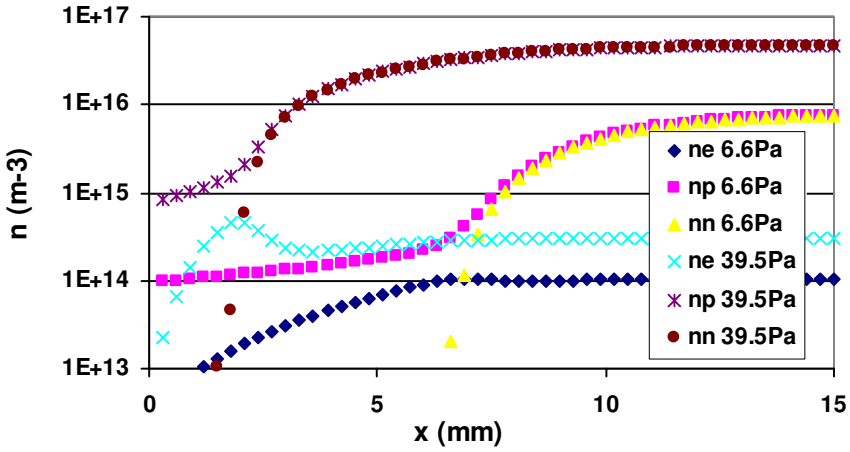

7.9 Simulations

From the particle levitation position (Fig. 7.2) and the Langmuir probe results it can be deduced that for pressures above 20 Pa collisional effects are important. These effects are not taken into account by the collisionless model presented in [136], thus, one can try to explain the experimental results by numerical simulation. The fluid Siglo-RF code (Kinema) [137] for a symmetric RF discharge in O_2 has been used, the gap between electrodes being 30 mm, the gas pressure p=6.6 Pa and 49.5 Pa, and the amplitude of RF voltage U_{rfP-P}=300 V. The time-averaged profiles of n_e, n_i, n_- (negative ions) are obtained, see Fig. 7.17 and the electric field and potential, see Fig. 7.18.

Particularly interesting is the peak in the electron density at 39.5 Pa, at about 2 mm from the electrode, due to the radiofrequency. In an asymmetric discharge as in the experiments discussed here one would expect this peak to be even larger. The values deduced from Fig. 7.17 are somewhat higher than the experimentally derived. In a plasma environment with an isotropic distribution of ions, the charge of the particles is calculated using the vacuum approximation, $Q = 4\pi\varepsilon_0 a V_f$, with V_f the floating potentials, derived from the balance of currents on the surface of the particle:

$$n_i e\sqrt{\frac{k_B T_i}{2\pi M_i}}\left(1+\frac{e|V_f|}{k_B T_i}\right) = n_e e\sqrt{\frac{k_B T_e}{2\pi m}}e^{-\frac{e|V_f|}{k_B T_e}} + n_- e\sqrt{\frac{k_B T_-}{2\pi M_-}}e^{-\frac{e|V_f|}{k_B T_-}} \tag{7.31}$$

Instead, for directed ions in the sheath, equation 7.23 has been used, where the directed

Figure 7.18: Time-averaged profiles of voltage V and electric field E at P=6.6 and 39.5 Pa.

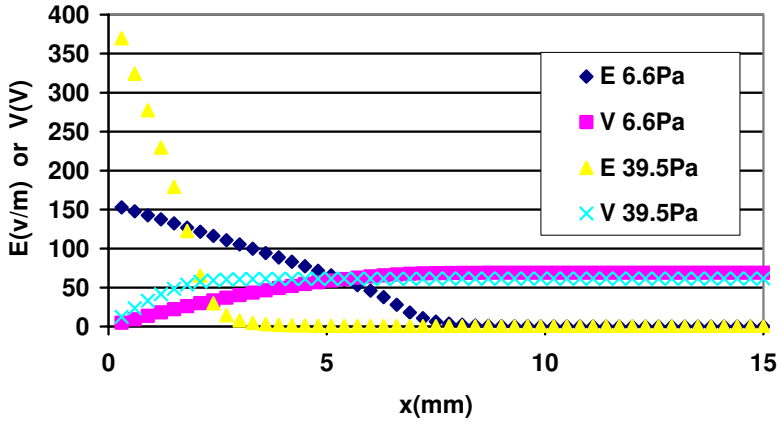

Figure 7.19: Levitation forces for particles of three sizes from plasma and sheath solution at P=6.5 Pa. Strength lines define the weight for each particles size.

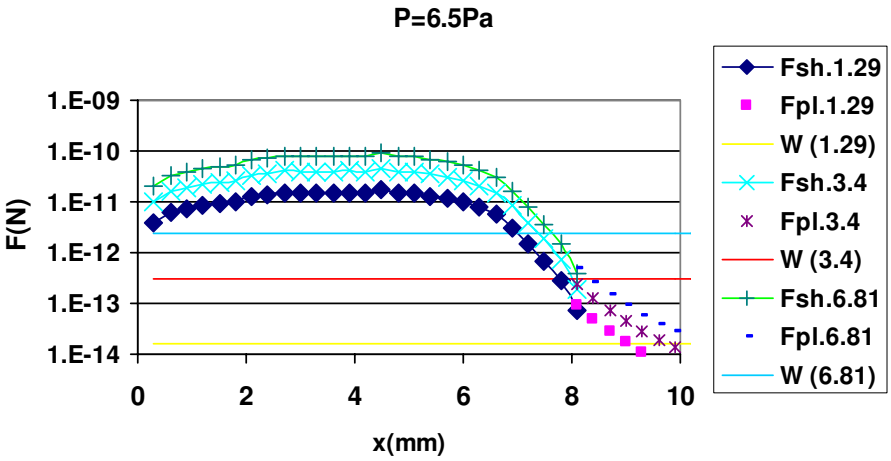

Figure 7.20: Levitation forces for particles of three sizes from plasma and sheath solution at P=39.4 Pa. Strength lines define the weight for each particles size

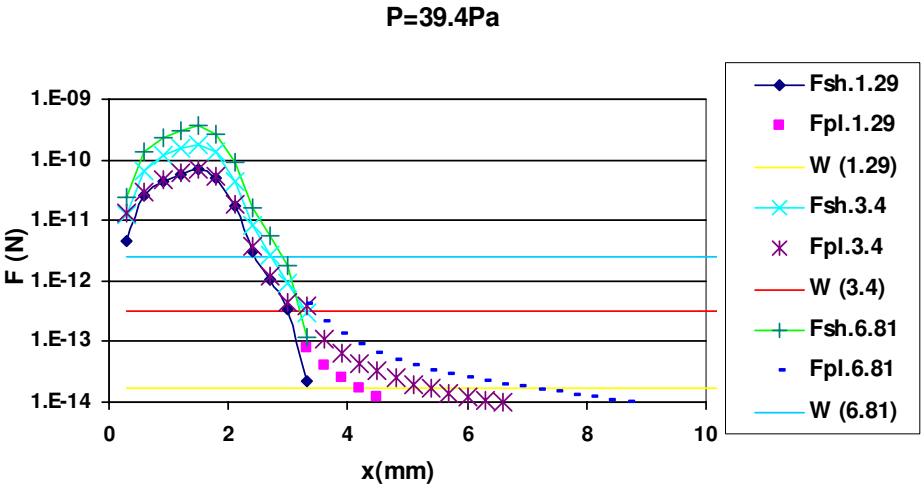

motion of ions is taken into account:

$$n_i e\sqrt{\frac{2e|V_0|}{M_i}}\left(1+\frac{|V_f|}{|V_0|}\right)=4n_e e\sqrt{\frac{k_B T_e}{2\pi m}}e^{-\frac{|V_f|}{k_B T_e}}+4n_{-}e\sqrt{\frac{k_B T_{-}}{2\pi M_{-}}}e^{-\frac{|V_f|}{k_B T_{-}}} \tag{7.32}$$

Here all V are negative numbers, V_0 is measured from the plasma and V_f is measured from the local V_0. If collisions are important V_0 should be replaced by the drop of voltage in the last mean free path. The values M_{-}=16 and M_i=32 has been used.

The levitation force and the weight of the particles are shown in Fig. 7.19 and Fig. 7.20, the lined curves correspond to the sheath solution (eq. 7.32). The theoretical equilibrium position of the particles is indicated by the crossing of the weight line with the respective levitation force. The larger and medium particles have almost coinciding equilibrium position while the smaller particles are clearly in the range, where the plasma solution applies (eq. 7.31). One cannot see the double equilibrium position as in Fig. 7.3. This may be attributed to the nonsymmetric set-up of our experiment or to some approximation of the code.

7.10 Summary

In this section the diagnostic of electronegative discharge by using dust particle has been discussed. The results presented are, to our knowledge, the first experimental proof of

a structured electronegative plasma sheath, a possibility so far only mathematically and numerically investigated. There is, however, some caveat that is necessary to include in this discussion: the range of instability is narrow and the equilibrium positions for the micro particles, used in the diagnostic, are subject to fluctuations. The fact that the conditions reported could be (in part) dependent on the apparatus also cannot be excluded completely. In fact the purity of the gas is essential, as already pointed out by [123]. Another important effect is the RF voltage drop at the electrode sheath. Although this effect has not been taken in account in the calculation of the levitation force it is known that both the charge of the particle and the sheath electric field are affected. The dependence on the energy of all the collision coefficients is not accurately known, on the other hand, using the most probable reactions the existence of three negative species in an RF Oxygen plasma has been identified. The experimental data seem to confirm our deductions.

Conclusions

Dusty (complex) plasma physics is relatively new field and at the same time it is of great interest in physics. One of the reasons is its interdisciplinary. Astrophysicists are interested in dusty plasmas, because many astrophysical objects contain dust. Besides, space dust can influence the working regime of space probes and satellites.

In modern technology plasmas are very much in use as well. In plasma reactors it is impossible to avoid the processes of sputtering from the reactor surfaces (electrodes and walls) and in situ particles growth. These particles are charged negatively and usually levitate close to one of the electrodes. After switching off the discharge they are deposited on the processed surface, can contaminate it and change its properties. Besides, dust can also influence the discharge parameters. But in some industrial applications dust has a positive aspect, for example, in so-called "polymorphous" solar cell production.

The simplicity of particle visualization provides a unique opportunity to observe complex processes occurring in many particle systems at the individual particle level. The detailed analysis of the thermodynamics of crystalline and liquid phases, self-organization, critical and cooperative phenomena, etc. becomes possible allowing new insights into the kinetic origin of physical processes that previously could not be investigated experimentally. The interaction between dust particles and the surrounding plasma can also be used as a diagnostic tool for the characterization of the potential and electric field profiles in the plasma sheath.

In this thesis some problems concerning technological dusty plasma applications, in particular the possibility of particle manipulation, as well as fundamental studies – analysis of the particle behavior in electronegative discharges, formation of dust clusters and analysis of particle dynamics inside these clusters have been considered.

The experiments presented in the thesis have been performed in a low-pressure capacitively - coupled RF plasma in Argon. The lower electrode in the discharge was the so-called "adaptive electrode" which consists of small segments - pixels, each segment independently driven with RF or/and DC voltage. By applying this additional voltage to the chosen segment one can create bright regions of ionization, "secondary plasmas", in the sheath region of the main plasma and above. The ionization degree in this "secondary

plasma" depends on the amplitude of the voltage applied. Such local modifications of the plasma change the whole discharge structure and introduce new possibilities for studying the plasma discharge. In this thesis the influence of RF voltage on the plasma parameters, which can be widely used in RF discharge experiments, has been theoretically studied. In particular, the electric field and plasma densities and dependent on them dust particle charge and positions of levitation, have been investigated both for the "pure" DC case and the case with RF voltage on the segment. It would be shown, both theoretically and experimentally, that the presence of a RF component influences the electric field and charge of particles, thereby changing the levitation positions.

By varying the amplitude of the RF voltage, the discharge configuration and the positions of the particles could be changed as well. The dust particles have been "collected" from their original levitation positions in the sheath to move more closely to the electrode inside the "secondary plasma". Thus, it is possible to manipulate their transport behavior. Dust manipulation is an important topic in plasma processing of materials, where the removal of dust from plasma reactors is crucial. It is important to note that in our case dust particles levitate not in the plasma sheath, as it usually happens in dusty plasma experiments under gravity conditions, but in the bulk plasma region, similar to the experiments conducted under microgravity conditions.

Furthermore, the collected particles create well ordered structures - three-dimensional spherical crystals without forming vertical chains, as in the plasma sheath. By fine adjustment of the amplitude of voltage on the segment the number of particles inside these structures can be varied. This possibility can be used in microchip technology as well as for fundamental studies of many particle systems and condensed matter. The fundamental investigations of plasma cluster properties has been the subject in a series of experimental and theoretical investigations.

In order to characterize the behavior in the clusters it is necessary to know the parameters of the plasma at the position, where the clusters are situated. In this thesis a study of the cluster environment has been presented. Because of the very small size and the RF nature of the "secondary plasma", Langmuir probes could not be used. Therefore, spectroscopic analysis has been chosen as the most suitable method of plasma diagnostics. Using the steady-state corona model and calculation of the geometrical volumes of main and "secondary plasmas", the density in this "small plasma" has been obtained. Besides, the density distribution has been compared to the results of two theoretical models built on the principles of the ion collisional motion. Both of the theories demonstrate good agreement with experimental data behavior.

Small plasma clusters with the number of particles ranging from 4 to 73 were formed inside the "secondary plasma". At the chosen experimental conditions clusters stayed in

liquid phase and some re-arranging inside the structures as well as particle vibrations have been observed. The cluster investigations have been performed in a set-up supported by a specific 3D optical diagnostics, which monitors simultaneously the images of x,y and the z,y positions of particles in the chamber. After that, by correlation of the images in the y direction three particle coordinates have been extracted simultaneously using the programming analysis. Due to this possibility one could reconstruct the kinematics of particles in clusters without losing information about fast processes. All clusters have been analyzed in such a way.

In the smallest cluster of 4 particles spontaneous attraction between dust particles has been observed. Assuming that nearest neighbor effects dominate, the interaction force has been estimated. It has a repulsive nature at small particle separation (<0.17 mm) - as expected from electrostatic interaction - and it is attractive at larger distances, with a maximum attractive force of $2.4 \cdot 10^{-14}$ N. The external confinement in this case has been estimated to be weaker ($\sim 10^{-15}$ N) than the attractive force. Therefore it can be concluded that an attractive component of the binary interaction between particles in the plasma has been identified. In the largest cluster of 73 particles the interaction force has also been estimated, but in this case collective effects should dominate and binary interaction processes may be expected to be masked by these.

Two other clusters with 17 and 63 particles have also been studied in detail. In both of these clusters particle rearrangement inside was observed. It seems reasonable to assume that this rearrangement may be explained by the motion of particles to find an energetically preferable position. That provides a minimum energy for the whole system. Therefore, the energy of both clusters during reorganization has been calculated. The calculation has demonstrated that after external perturbations clusters change their structure in order to achieve a more stable state in accordance with the principle of minimum energy. Moreover, it has been shown that the original 63 particle cluster ejects the particles to get the number 60, which is the so-called "magic" number for 3D configuration, as has been found in the simulation of [113] for Coulomb interaction. Further, the characteristic vibrations of this cluster have been analyzed using Fast-Fourier transform. The result gave a "fundamental" cluster frequency, which agrees well with the theory of dust-acoustic waves. Since this cluster is in the liquid state, it has also been compared to a liquid drop with surface tension. The observed resonances in the Fourier spectrum gave good agreement with the resonance mode frequencies of a spherical liquid drop, showing that even such small clusters –with only 63 particles – can exhibit fluid-like cooperative behavior.

In the last part of this thesis the behavior of dust particles in electronegative discharges (Oxygen) has been studied. Since electronegative discharges are widely used in different industrial processes, the experimental investigations of plasmas with negative ions has a

big practical value. In electronegative discharges the dust particles have been used as a diagnostic tool. Firs of all, injecting microparticles into the plasma it has been possible to visualize the potential distribution in the plasma sheath, something that no other diagnostic can do. The same has been done with sputtered dust particles of nanometer size, so called "fog", in experiments with Argon. Furthermore, a mathematical model for the dust particle levitation in electronegative plasmas has been developed, which gives the dependence of particle positions on the plasma parameters. Due to this model the distribution of potential and electric field as well as dust particle charge for our experimental conditions have been obtained. Besides, from the probe measurements the density of negative ions has been estimated. The observed double layer in particle positions shows to our knowledge, the first experimental proof of a structured electronegative plasma sheath, which has been already theoretically predicted [121]. Two families of negative ions with different temperatures have been identified out after consideration of the most probable chemical reactions in Oxygen. It is that the particles of smallest size (1.29 μm diameter), which are observed to split into two layers, can do this, because they can follow this small difference in the ion energy.

The measurement of the plasma parameters using electric probes constitutes a significant part of the work in Oxygen gas. The electric probe measurements in a plasma with negative ions have some specifics. First of all, it is difficult to get the correct temperature of electrons, because there is an additional fraction with negative charge (but big mass – the negative ions). Negative ions influence also the behavior of current-voltage characteristics, making a contribution to the overall ion current. A number of probe measurements under different experimental conditions (pressure, RF voltage, Oxygen flow and different probe positions) has been carried out. The obtained IV-characteristics have shown different amounts of negative ions depending on these conditions. These dependencies can be used in fundamental studies of Oxygen discharges as well as for applications in industry.

Bibliography

[1] A. Bouchoule, (Wiley, New York, 1999).

[2] V. E. Fortov, A. G. Khrapak, S. A. Khrapak, V. I. Molotkov, and O. F. Petrov, Physics-Uspekhi **47(5)**, 447 (2004).

[3] P. K. Shukla and A. A. Mamun, (Institute of Physics Publishing Ltd., Bristol, 2002).

[4] T. Nitter and O. Hanvnes, Earth, Moon and Planets **56**, 7 (1992).

[5] T. G. Northrop, Phys. Scripta **45**, 475 (1992).

[6] C. K. Goertz, Review of Geophysics **27**, 271 (1989).

[7] G. E. Morfill, E. Grün, and T. B. Jonhson, Planetary and Space Science **28**, 1087 (1980).

[8] K. G. Spears, T. J. Robinson, and R. M. Roth, IEEE trans. Plasma Sci. **PS14(2)**, 179 (1986).

[9] J. Winter, Plasma Phys. Control. Fusion **40**, 1201 (1998).

[10] V. N. Tsytovich and J. Winter, Phys. Usp **41**, 815 (1998).

[11] P. Roca i Cabarrocas, P. Gay, and A. Hadjadj, J. Vac. Sci. Technol. **A(14)**, 655 (1996).

[12] E. Bertran, S. N. Sharma, G. Viera, J. Costa, P. St'ahel, and P. Roca i Cabarrocas, Journal of Materials Research **13(9)**, 2476 (1998).

[13] H. Thomas, G. E. Morfill, V. Demmel, J. Goree, B. Feuerbacher, and D. Mohlmann, Phys. Rev. Lett. **73**, 652 (1994).

[14] J. H. Chu and L. I., Phys. Rev. Lett. **72**, 4009 (1994).

[15] Y. Hayashi and K. Tachibana, Jpn. J. Appl. Phys. **33**, L 804 (1994).

[16] A. Melzer, T. Trottenberg, and A. Piel, Rev. Lett. A **191**, 301 (1994).

[17] Y. P. Raizer, (Pringer-Verlag, Berlin, Heidelberg, 1991).

[18] D. A. Mendis, Plasma Scources Sci. Technol **11**, A219 (2002).

[19] A. P. Nefedov, G. E. Morfill, V. E. Fortov, H. M. Thomas, H. Rothermel, T. Hagl, A. Ivlev, M. Zuzic, B. A. Klumov, A. M. Lipaev, V. I. Molotkov, O. F. Petrov, Y. P. Gidzenko, S. K. Krikalev, W. Shepherd, A. I. Ivanova, M. Roth, H. Binnenbruck, J. A. Goree, and Y. P. Semenov, New J. Phys. **5**, 33.1 (2003).

[20] S. A. Khrapak, A. V. Ivlev, G. E. Morfill, and H. M. Thomas, Phys. Rev. E **66**, 046414 (2002).

[21] I. Langmuir, Phys. Rev. **21**, 419 (1923).

[22] D. Bohm, *chapter 3* (Mcgraw-Hill, New York, 1949).

[23] J. E. Allen, B. M. Annaratone, and U. de Angelis, J. Plasma Physics **63**, 299 (2000).

[24] R. V. Kennedy and J. E. Allen, J. Plasma Physics **69**, 485 (2003).

[25] C. M. C. Nairn, B. M. Annaratone, and J. E. Allen, Plasma Sours Sci. Technol. **7**, 478 (1998).

[26] J. Goree, Plasma Sours Sci. Technol. **3**, 400 (1994).

[27] A. P. Nefedov, O. F. Petrov, and S. A. Khrapak, Plasma Physiscs **24**, 1109 (1998).

[28] A. V. Zobnin, A. P. Nefedov, V. A. Sinelshchikov, and V. E. Fortov, JETP **91**, 483 (2000).

[29] M. Lampe, G. Joyce, G. Ganguli, and V. Gavrishchaka, Phys. Plasmas **7**, 3851 (2000).

[30] S. A. Khrapak, A. V. Ivlev, and G. E. Morfill, Phys. Rev. E **64**, 046403/1 (2001).

[31] I. Langmuir and H. Mott-Smith, Phys. Rev. **28**, 727 (1996).

[32] J. D. Swift and M. J. R. Schwar, (Iliffe books ltd, London, 1970).

[33] J. E. Allen, Plasma Physics **84**, 670 (2001).

[34] J. E. Allen, R. L. F. Boyd, and P. Reynolds, Pros. Phys. Soc. **B**, 297 (1957).

[35] H. M. Mott-Smith and I. Langmuir, Phys. Rev. **28**, 727 (1926).

[36] D. Bohm, E. H. S. Burhop, and H. S. W. Massey, in *chapter 2*, edited by A. Guthrie and R. K. Wakerling (Mcgraw-Hill, New York, 1949).

[37] I. B. Bernstein and I. Rabinowitz, Phys. Fluids **2**, 112 (1959).

[38] J. G. Laframboise, *chapter 2* (Report 100, University of Toronto, Institut of Aerospace Studies, 1966).

[39] J. E. Allen, Physica Scripta **45**, 497 (1992).

[40] V. E. Fortov, A. V. Ivlev, S. A. Khrapak, A. G. Khrapak, and G. E. Morfill, Physics Reports **421**, 30 (2005).

[41] G. J. Schulz and S. C. Rrown, Phys. Rev. **98**, 1642 (1955).

[42] Z. Zakrzewski and T. Kopiczynski, Plasma Phys. **16**, 1195 (1974).

[43] S. A. Khrapak, S. V. Ratynskaia, A. V. Zobnin, A. D. Usachev, V. V. Yaroshenko, M. H. Thoma, M. Kretschmer, H. Höfner, G. E. Morfill, O. F. Petrov, and V. E. Fortov, Phys. Rev. E **72**, 016406 (2005).

[44] B. M. Annaratone, M. W. Allen, and J. E. Allen, J. Phys. D: Appl. Phys. **25**, 417 (1992).

[45] K. U. Riemann, Phys. Plasmas **4**, 4158 (1997).

[46] R. N. Franklin and J. Snell, J. Plasma Physics **64**, 131 (2000).

[47] F. F. Chen, J. Nucl. Energy **C7**, 47 (1965).

[48] J. E. Daugherty, R. K. Porteous, and D. B. Graves, J. Appl. Phys. **73**, 1617 (1993).

[49] L. Talbot, R. K. Cheng, R. W. Schefer, and D. R. Willis, J. Fluid. Mech. **101**, 737 (1980).

[50] H. Rothermel, T. Hagl, G. E. Morfill, and H. M. Thomas, Phys. Rev. Lett. **89**, 175001 (2002).

[51] G. E. Morfill and E. Grun, Planet. Space Sci. **27**, 1269 (1979).

[52] D. Samsonov and J. Goree, Phys. Rev. E **59**, 1047 (1999).

[53] M. S. Barnes, J. H. Keller, J. C. Forster, J. A. O'Neill, and D. K. Coutlas, Phys. Rev. Lett. **68**, 313 (1992).

[54] U. Konopka, D. Samsosnov, A. V. Ivlev, J. Goree, V. Steinberg, and G. E. Morfill, Phys. Rev. E **61**, 1890 (2000).

[55] P. K. Kaw, K. Nishikawa, and N. Sato, Phys. Plasmas **9**, 387 (2002).

[56] O. Ishihara, T. Kamimura, K. I. Hirose, and N. Sato, Phys. Rev. E **66**, 046406/1 (2002).

[57] A. V. Ivlev, D. Samsonov, J. Goree, G. E. Morfill, and V. E. Fortov, Phys. Plasmas **6**, 741 (1999).

[58] S. A. Khrapak and V. V. Yaroshenko, Phys. Plasmas **10**, 4616 (2003).

[59] G. E. Morfill, H. M. Thomas, U. Konopka, H. Rothermel, M. Zuzic, A. Ivlev, and J. Goree, Phys. Rev. Lett. **83**, 1598 (1999).

[60] S. A. Trigger, Phys. Rev. E **67**, 046403/1 (2003).

[61] S. A. Khrapak, A. V. Ivlev, G. E. Morfill, and S. K. Zhdanov, Phys. Rev. Letters **90**, 225002 (2003).

[62] W. B. Thompson and J. Hubbard, Rev. Mod. Phys. **43**, 046403/1 (2003).

[63] A. V. Ivlev, S. A. Khrapak, S. K. Zhdanov, G. E. Morfill, and G. Joyce, Phys. Rev. Lett. **92**, 205007/1 (2004).

[64] S. A. Khrapak and G. E. Morfill, Phys. Rev. E **69**, 066411 (2004).

[65] P. S. Epstein, Phys. Rev. **23**, 710 (1924).

[66] L. D. Landau and E. M. Lifshitz, (Pergamon Press, Oxford, 1987).

[67] U. Konopka, G. E. Morfill, and L. Ratke, Phys. Rev. Lett. **84**, 891 (2000).

[68] G. E. Morfill, V. N. Tsytovich, and H. Thomas, Plasma Physics Reports **29**, 1 (2003).

[69] A. M. Ignatov, Plasma Phys. Rep. **22**, 585 (1996).

[70] V. N. Tsytovich, Y. K. Khodataev, G. E. Morfill, R. Bingham, and D. J. Winter, Comments Plasma Phys. Control. Fusion **17**, 249 (1996).

[71] S. A. Khrapak, G. E. Morfill, A. V. Ivlev, H. M. Thomas, D. A. Beysens, B. Zappoli, V. E. Fortov, A. M. Lepaev, and V. I. Molotkov, Phys. Rev. Lett. **96**, 015001 (2006).

[72] V. N. Tsytovich, Y. K. Khodataev, G. E. Morfill, R. Bingham, and D. J. Winter, Comments Plasma Phys. Control. Fusion **18**, 281 (1998).

[73] S. A. Khrapak and G. E. Morfill, Phys. of Plasmas **13**, 104506 (2006).

[74] A. Melzer, V. A. Schweigert, and A. Piel, Phys. Rev. Lett. **83**, 3194 (1999).

[75] V. Steinberg, R. Sutterlin, A. V. Ivlev, and G. Morfill, Phys. Rev. Lett. **86**, 4540 (2001).

[76] A. A. Samarian, S. V. Vladimirov, and B. M. James, Phys. Plasmas. **12**, 022103 (2005).

[77] V. V. Yaroshenko, A. Ivlev, and G. E. Morfill, Phys. Rev. E **71**, 046405 (2005).

[78] W. R. Smythe, *Static and dynamical electricity* (McHill Book Company, Inc., 1950), pp. 6–7.

[79] V. V. Yaroshenko, B. M. Annaratone, T. Antonova, H. M. Thomas, and G. E. Morfill, New J. Phys. **8(9)**, 1 (2006).

[80] Y.-J. Lai and L. I, Phys. Rev. E **60**, 4743 (1999).

[81] T. Totsuji, Phys. Plasmas **8**, 1856 (2001).

[82] W.-T. Juan, Phys. Rev. E **58**, R6947 (1998).

[83] J. Goree, G. E. Morfill, V. N. Tsytovich, and S. V. Vladimirov, Phys. Rev. E **59**, 7055 (1999).

[84] V. N. Tsytovich, S. V. Vladimirov, G. E. Morfill, and J. Goree, Phys. Rev. E **63**, 056609 (2001).

[85] G. E. Morfill, H. M. Thomas, U. Konopka, and M. Zuzic, Phys. Plasmas **6**, 1769 (1999).

[86] H. M. Thomas and G. E. Morfill, Nature **379**, 806 (1996).

[87] H. M. Thomas and G. E. Morfill, J. Vac. Sci. Thechnol. **A 14**, 501 (1996).

[88] A. Melzer, A. Homann, and A. Piel, Phys. Rev. E **53**, 2757 (1996).

[89] F. A. Z. Lindemann, Phys. **11**, 609 (1910).

[90] J.-P. Hansen and L. Verlet, Phys. Rev. **184**, 151 (1910).

[91] H. Löwen, T. Palberg, and R. Simon, Phys. Rev. Lett **70**, 1557 (1993).

[92] R. A. Quinn, C. Cui, J. Goree, J. B. Pieper, H. Thomas, and G. E. Morfill, Phys. Rev. E **53**, 2049 (1996).

[93] M. Zuzic, A. V. Ivlev, J. Goree, G. E. Morfill, H. M. Thomas, H. Rothermel, U. Konopka, R. Sütterlin, and D. D. Goldbeck, Phys. Bev. Lett. **85 (19)**, 4064 (2000).

[94] O. Arp, D. Block, A. Piel, and A. Melzer, Phys. Rev. Lett. **93**, 165004 (2004).

[95] D. D. Goldbeck, PhD Thesis Ludwig Maximillian University, Munich, Germany (2003).

[96] B. M. Annaratone, M. Glier, T. Stuffler, H. Thomas, M. Raif, and G. E. Morfill, New Journal of Physics **5**, 92.1 (2003).

[97] A. Dyson, P. Bryant, and J. E. Allen, Meas. Sci. Technol. **11**, 541 (2000).

[98] B. M. Annaratone, G. F. Counsell, H. Kawano, and J. E. Allen, Plasma Sours Sci. Technol. **1**, 232 (1992).

[99] B. M. Annaratone and N. S. J. Braithwaite, Meas. Sci. Technol. **2**, 795 (1991).

[100] F. Melandsø, T. Nitter, T. Aslaksen, and O. Havnes, J. Vac. Sci. Technol. **A 14**, 619 (1996).

[101] P. D. Prewett and J. E. Allen, Proceedings of the Royal Society of London series A—mathematical, physical and engineering sciences **348**, 435 (1976).

[102] M. Mikikian, L. Boufendi, A. Bouchoule, H. M. Thomas, G. E. Morfill, A. P. Nefedov, and V. E. Fortov, New J. of Phys. **5**, 19 (2003).

[103] B. M. Smirnov, (Springer, Berlin, Heidelberg, 1999).

[104] J. Cobine, (Gaseous Conductors, Dover Publications, New York, 1958).

[105] I. H. Hutchinson, Principles of plasma diagnostics, Press Syndicate of the University of Cambridge, Cambridge 199 (1987).

[106] D. Wobschall, J. R. Graham, and D. P. Malone, Phys. Rev. **131**, 1565 (1963).

[107] B. M. Annaratone, Journal de Physique **IV 7 (C4)**, 155 (1997).

[108] P. Bryant, J. Phys. D: Appl. Phys. **36**, 2859 (2003).

[109] B. M. Annaratone and G. E. Morfill, J. Phys. D: Appl. Phys. **36**, 2853 (2003).

[110] A. V. Ivlev, G. E. Morfill, and U. Konopka, Phys. Rev. Lett. **89 19**, 195502 (2002).

[111] B. M. Annaratone, S. A. Khrapak, P. Bryant, G. E. Morfill, H. Rothermel, H. M. Thomas, M. Zuzic, V. E. Fortov, V. I. Molotkov, A. P. Nefedov, S. Krikalev, and Y. P. Semenov, Phys. Rev. E **66**, 056411 (2002).

[112] T. Antonova, B. M. Annaratone, D. D. Goldbeck, V. Yaroshenko, H. M. Thomas, and G. E. Morfill, Phys. Rev. Lett. **96**, 115001 (2006).

[113] P. Ludwig, S. Kosse, and M. Bonitz, Phys. Rev. E **71**, 046403 (2005).

[114] R. V. Kennedy and J. E. Allen, J. Plasma Physics **67**, 243 (2002).

[115] L. D. Landau and E. M. Lifshitz, (Fluid Mechanics, London Pergamon Press, 1959).

[116] H. Amemiya, J. Phys. D: Appl. Phys. **23**, 999 (1990).

[117] K. G. Emeleus and J. R. M. Coulter, Int. J. electron. **54**, 777 (1983).

[118] J. R. M. Coulter and K. G. Emeleus, Int. J. electron. **64**, 961 (1988).

[119] M. Matsuoka, Y. Hoshi, and M. Naoe, J. Appl. Phys. **63**, 2098 (1988).

[120] D. Vender, W. W. Stoffels, E. Stoffelsand, G. M. W. Kroesen, and F. J. de Hoog, Phys. Rev. E **51**, 2436 (1995).

[121] N. S. J. Braithwaite and J. E. Allen, J. Phys. D **21**, 1733 (1988).

[122] T. E. Sheridan, J. Phys. D: Appl. Phys. **32**, 1761 (1999).

[123] E. Stoffels, W. W. Stoffels, D. Vender, M. Kandoand, G. M. W. Kroesen, and F. J. de Hoog, Phys. Rev. E **51**, 2425 (1995).

[124] R. N. Franklin, Plasma Sours Sci. Technol. **11**, A31 (2002).

[125] R. N. Franklin and J. Snell, J. Plasma Physics **64**, 131 (2000).

[126] K. Sato and F. Miyawaki, J. Phys. Fluids B **4**, 1247 (1992).

[127] H. Amemiya, B. M. Annaratone, and J. E. Allen, J. Plasma Physics **60**, 81 (1998).

[128] T. E. Sheridan, P. Chabert, and R. W. Boswell, Plasma Sours Sci. Technol. **8**, 457 (1999).

[129] J. E. Allen, J. Phys. D: Appl. Phys. **9**, 2331 (1976).

[130] H. Amemiya, B. M. Annaratone, and J. E. Allen, Plasma Sours Sci. Technol. **8**, 179 (1999).

[131] B. M. Smirnov, (McGraw-Hil, New York, 1982).

[132] G. Herzberg, (Inst Sci Inform Inc, Philadelphia, 1983).

[133] L. E. Khvorostovskaya and V. A. Yankovsky, Contrib. Plasma Phys. **31**, 71 (1991).

[134] P. Chabert and T. E. Sheridan, J. Phys. D **33**, 1854 (2000).

[135] H. Amemiya, B. M. Annaratone, and J. E. Allen, J. Plasma Physics **60**, 81 (1997).

[136] B. M. Annaratone, T. Antonova, D. D. Goldbeck, H. Thomas, and G. E. Morfill, Plasma Phys. Control. Fusion **46**, B495 (2004).

[137] L. C. Pitchford, S. V. O'Neil, and J. R. Rumble, Phys Rev A **23**, 294 (1981).

Acknowledgements

Here I would like to thank all of the people who made it possible to perform this work and contributed to its success.

First of all, I would like to thank my supervisor Prof. Dr. Dr. h.c. Gregor Morfill who gave me the opportunity to carry out my work in Max-Planck-Institut für Extraterrestrische Physik in the Theory and Complex plasma group. Thank you very much for your support, scientific help and discussions and personal understanding.

Especially I would like to thank Dr. Beatrice Annaratone. None of my work would have been possible without you. My sincere gratitude for your teaching, for very helpful and interesting discussions, which always gave me a huge impulse and motivation for new work. Thank you very much for the hours in the laboratory, where I have learnt from you a lot of useful and interesting things. I am grateful to you for taking care of me and our work.

I am grateful to Herrn Bernd Steffes for his inestimable constant technical support in two laboratories. Thank you very much for your help with our experiments, teaching me and taking care of me in the laboratory. Main herzlicher Dank Ihnen, Herr Steffes!

I would like to thank to Dr. Dirk David Goldbeck, who has built the set-up with 3D laser diagnostics, where I could perform the largest part of the work presented here. Thank you also very much that you have taught me how to calibrate your set-up and to work with it and how to perform the programming analysis in order to get the dust particle positions.

I am grateful to Dr. Hubertus Thomas, Prof. Victoriya Yaroshenko, Dr. Sergej Khrapak and Dr. Michael Kretschmer for the help with this thesis, for useful scientific discussions and suggestions and always great moral support.

Also, I would like to thank Herrn Herwig Höfner for help with the project organization.

I would like to thank Prof. John Allen from University College, Oxford for his great teaching and taking care of me during my visit in Oxford and also for his help with our paper.

I am very grateful to all my colleagues in Complex plasma group: Prof. Vadim Tsytovich, Dr. Michael Poustylnik, Dr. Milenko Rubin-Zuzic, Manis Chaudhuri, Dr. Uwe Konopka, Dr. Vladimir Nosenko, Prof. Markus Thoma, Dr. Boris Klumov, Dr. Sergey Zh-

danov, Dr. Hermann Rothermel, Ralf Heidemann, Peter Huber, Martin Fink, Herbert Scheingraber, Dr. Tetsuji Shimizu, Slobodan Mitic, Dr. Alexey Khrapak, Tanja Hagl, Dr. Alexey Ivlev, Christina Knapek, Robert Sütterlin, Mierk Schwabe, Dr. YangFang Li, Dr. Roman Kompaneets, Dr. Irina Sidorenko and Dr. Satoshi Shimizu for their help always, when I asked, for the great moral support and for the nice and friendly atmosphere in the group.

I would like to thank to Frau Angelika Langer and Frau Elsbeth Collmar, our secretaries, for their help and support not only in administrative issues.

Also I am grateful to all of the professors from Kharkiv National V.N. Karazin University, Physical and Technical Faculty for their great teaching and to the colleagues from the Department of Physical Technologies for giving me the possibility to get my first scientific experience.

Especially I am very grateful to two people, my parents. I am grateful to my mother for supporting me all the time. To my father, who always did for me everything in his whole life, I am grateful with all my heart, I wish you were still with us, I miss you very much.

Also I would like to thank Dr. Alexei Matveev for supporting and helping me always and, in particular, with this thesis.

Publications

Refereed publications:

1. T. Antonova, B. M. Annaratone, H. M. Thomas and G. E. Morfill, Energy relaxation and vibrations in small 3D plasma clusters, New J. Phys. 10 (2008) 043028
2. G.E. Morfill, A.V. Ivlev, M. Rubin-Zuzic, C.A. Knapek, R. Pompl, T. Antonova, H.M. Thomas, Complex plasmas new discoveries in strong coupling physics, Appl. Phys. B 89, 527534 (2007)
3. V.V. Yaroshenko, B.M. Annaratone, T. Antonova, H.M. Thomas and G.E. Morfill, Dynamics of cluster particles in a dense plasma, New J. Phys. 8, No 9, 203 (1-12), 2006
4. T. Antonova, B.M. Annaratone, D.D. Goldbeck, V. Yaroshenko, H.M. Thomas and G.E. Morfill, Measurements of the interaction force among particles in three-dimensional plasma clusters, Phys. Rev. Letters 96 (11), 115001, 2006
5. B.M. Annaratone, T. Antonova, D.D. Goldbeck, H.M. Thomas and G.E. Morfill, Complex-plasma manipulation by radiofrequency biasing, Plasma Physics and Controlled Fusion 46: B495-B509 Sp. Iss. SI Suppl. 12B, 2004
6. B.M. Annaratone, T. Antonova, H.M. Thomas and G.E. Morfill, Diagnostics of the electronegative plasma sheath at low pressures using microparticles, Phys. Rev. Letters 93 (18): Art. No. 185001, 2004

Not refereed publications:

7. T. Antonova, B. M. Annaratone, H. M. Thomas and G.E. Morfill, The structure and dynamical processes in small 3D crystals, Proceedings to 2nd International Conference on the Physics of Dusty and Burning Plasmas, August 26-30, 2007, Odessa, Ukraine
8. T. Antonova, B. M. Annaratone, H. M. Thomas and G.E. Morfill, Analysis of the particle vibrations in 3D plasma clusters, Proceedings to 28th ICPIG, July 15-20, 2007, Prague, Czech Republic
9. V. Yaroshenko, B.M. Annaratone, T. Antonova, H.M. Thomas and G. Morfill, Inter-

action forces between cluster particles in a dense plasma, 33rd European Physical Society Conference on Plasma Physics, Rome, Italy, June 19-23, 2006

10. T. Antonova, B.M. Annaratone, H.M. Thomas and G.E. Morfill, Natural oscillations in 3D plasma clusters, electronic proceedings, Thirty-Third EPS Conference on Plasma Physics, Rome, Italy, June 19-23, 2006

11. T. Antonova, B.M. Annaratone, T. Sato, H.M. Thomas and G.E. Morfill, Spectroscopic investigation of the 3D plasma clusters' environment, electronic proceedings, 13th International Congress on Plasma Physics, Kiev, May 22-26, 2006

12. T. Antonova, B.M. Annaratone, D.D. Goldbeck, V.Yaroshenko, H.M. Thomas, G.E. Morfill, Interaction among Particles in 3D Plasma Clusters, AIP Conference Proceedings, 799, p.299, 2005

13. T. Antonova, B.M. Annaratone, H.M. Thomas and G.E. Morfill, The structure of a plasma cluster as seen by an injected particle, Proceedings to Thirty-Second EPS Conference on Plasma Physics, Tarragona, Spain 27 June – 1July, 2005

14. B.M. Annaratone, T.Antonova, V.A. Lisovskiy, H.M. Thomas, G.E. Morfill, Levitation of particles in O_2 plasma, Proceedings to Thirty-First EPS Conference on Plasma Physics, London, July 2004

15. T. Antonova, S.V. Dudin, V.I. Farenik, The Langmuir probe modelling in ion-beam plasma, Proceedings to International Conference and School on Plasma Physics and Controlled Fusion, Ukraine, 2003

16. T. Antonova, S.V. Dudin, V.I. Farenik, Currents of fast and slow ions to the Langmuir probe in ion-beam plasma, Problems of Atomic Science and Technics, Series Plasma Physics, V.9, N 1, pp. 147-149, 2003

CURRICULUM VITAE

Tetyana Antonova

Date and place of birth	February 27, 1979, Kupyansk, Ukraine
1986–1992	Study in Kupyansk Secondary School Nr.4, Ukraine
1992–1996	Study in Kupyansk Gymnasium Nr.1, Ukraine
1996–2002	Study in Kharkiv National V.N. Karazin University, Department of Scientific Physical Technologies, specialization – Plasma Physics
February 2002	The graduation from the University, the subject of Diploma thesis: "The Langmuir probe model in ion beam plasma".
June 2001-January 2004	Half-time position of Junior Scientific Researcher at Scientific Center of Physical Technologies of Ukrainian Academy of Science and Ministry of Education and Science of Ukraine
2002-2004	Scientific research in the field of low-temperature plasma diagnostics in Kharkiv National V.N. Karazin University, Ukraine
From 2004	Ph.D student at Max-Planck-Institut für Exstraterrestrische Physik, Theory and Complex plasma group, Germany